Studies of Origami and Kirigami and Their Applications

by

Zeming Song

A Dissertation Presented in Partial Fulfillment
of the Requirements for the Degree
Doctor of Philosophy

Approved April 2016 by the
Graduate Supervisory Committee:

Hanqing Jiang, Chair
Lenore Dai
Hongbin Yu
Ximin He

ARIZONA STATE UNIVERSITY

May 2016

ABSTRACT

Origami and Kirigami are two traditional art forms in the world. Origami, from ‘ori’ meaning folding, and ‘kami’ meaning paper is the art of paper folding. Kirigami, from ‘kiri’ meaning cutting, is the art of the combination of paper cutting and paper folding. In this dissertation, Origami and kirigami concepts were successively utilized in making stretchable lithium ion batteries and three-dimensional (3D) silicon structure which both provide excellent mechanical characteristics.

First chapter of this dissertation demonstrates an origami Lituium-ion battery (LIB) that can be deformed at an unprecedented high level, including folding, bending and twisting. Deformability at the system-level is enabled using rigid origami, which prescribes a crease pattern such that the materials making the origami pattern do not experience large strain. The origami battery is fabricated through slurry coating of electrodes onto paper current collectors, packaging in standard materials, followed by folding using the Miura pattern. The resulting origami battery achieves significant linear and areal deformability, large twistability, and bendability.

Second chapter of this dissertation demonstrates stretchable LIBs using the concept of kirigami. The designated kirigami patterns have been discovered and implemented to achieve great stretchability (over 150%) to LIBs that are produced by standardized battery manufacturing. It is shown that fracture due to cutting and folding is suppressed by plastic rolling, which provides kirigami LIBs excellent electrochemical and mechanical characteristics. The kirigami LIBs have demonstrated the capability to be integrated and power a smart watch, which may disruptively impact the field of wearable electronics by offering extra physical and functionality design spaces.

Third chapter of this dissertation demonstrates a new strategy to fabricate microscale origami using Silicon (Si) nano-membrane (NMs) as the materials that are supported by elevated polydimethylsiloxane (PDMS) walls on top of a PDMS substrate.

This dissertation aims to deepen study origami and kirigami patterns, understand mathematics and mechanical properties behind them and discover their applications.

DEDICATION

I dedicate my dissertation work to my family. I present a special feeling of gratitude to my loving parents, Shizhong Song and Yaping Jiang whose words of encouragement and push for tenacity ring in my ears. I also dedicate this dissertation to my wife, Wenwen Xu, for the unconditional love and support she has for me.

ACKNOWLEDGMENTS

I would like to first express my deepest gratitude to my supervisor, Prof. Hanqing Jiang, who has always been supportive, helpful and caring ever since I entered the Master program at Arizona State University. His vision, leadership and perseverance for research have been the constant driving force for my progress. I also especially thank him for supporting and assisting my wife to pursue her PhD studies in his group. I feel very fortunate to have been his student, and therefore to have had such an enjoyable and fulfilling graduate school experience.

I would also like to deeply thank Prof. Hongyu Yu and Prof. Candace K. Chan, who were abundantly helpful and offered invaluable assistance and guidance to my experimental projects.

I also love to thank Prof. Hongbin Yu and Dr. Min Tao who have been advising me on Intel SRS project during the two and a half years.

In addition, I am very grateful for all the help and advice from my committee members, Prof. Lenore L. Dai and Prof. Ximin He.

Last but not the least, the help and support from my colleagues at Arizona State University, Dr. Teng Ma, Dr. Rui Tang, Dr. Hai Huang, Dr. Hanshuang Liang, Dr. Prithwish Chatterjee, Dr. Yonghao An, Qian Cheng, Cheng Lv, Xu Wang, Mengbing Liang, Ruirui Han, Haokai Yang, Jinshan Lin, Wei Zeng, Todd Houghton, Yiling Fan, Tianwei Sun, Dr. Qiang Liu and Deepakshyam Krishnaraju are truly appreciated.

TABLE OF CONTENTS

Page

LIST OF FIGURES

Figure Page

Figure Page

Figure Page

Figure Page

CHAPTER 1

GENERAL INTRODUCTION OF ORIGAMI AND KIRIGAMI-FUSION OF ARTS AND ENGINEERING

1.1 Introduction of Origami

Origami, the art of paper folding (*1*), is often associated with Japanese culture. Paper was first invented in China in the year 102 A.D. and then brought to Japan in the sixth century A.D. Since then, Japan has developed origami to a very high art form. In modern usage, the word 'origami' is used as an inclusive term for all folding practices, regardless of their culture of origin. The goal is to provide the ability to create versatile 3D stable configurations from 2D sheets.

Origami structures can be simply classified as static origami and dynamic origami; or rigid origami and non-rigid origami. Static origami is a common art form of origami that has been handed down from parent to child through many generations. Animals, birds, fish, puppets, toys and masks are among the models that even very young children can learn to make in just one sitting. Figure 1.1(a) shows the most well know paper crane.

(a) (b)

Figure 1.1. (a) Origami paper crane. (b) Origami Chinese dragon.

Much more delicated static origami such as Chinese dragon shown in figure 1.1(b) was created by artists. Dynamic origami is a developed form of origami, namely, dynamic origami can deform. One example of dynamic origami structure shown in figure 1.2 is called ‘waterbomb’ structure, or the nick name ‘magic ball’.

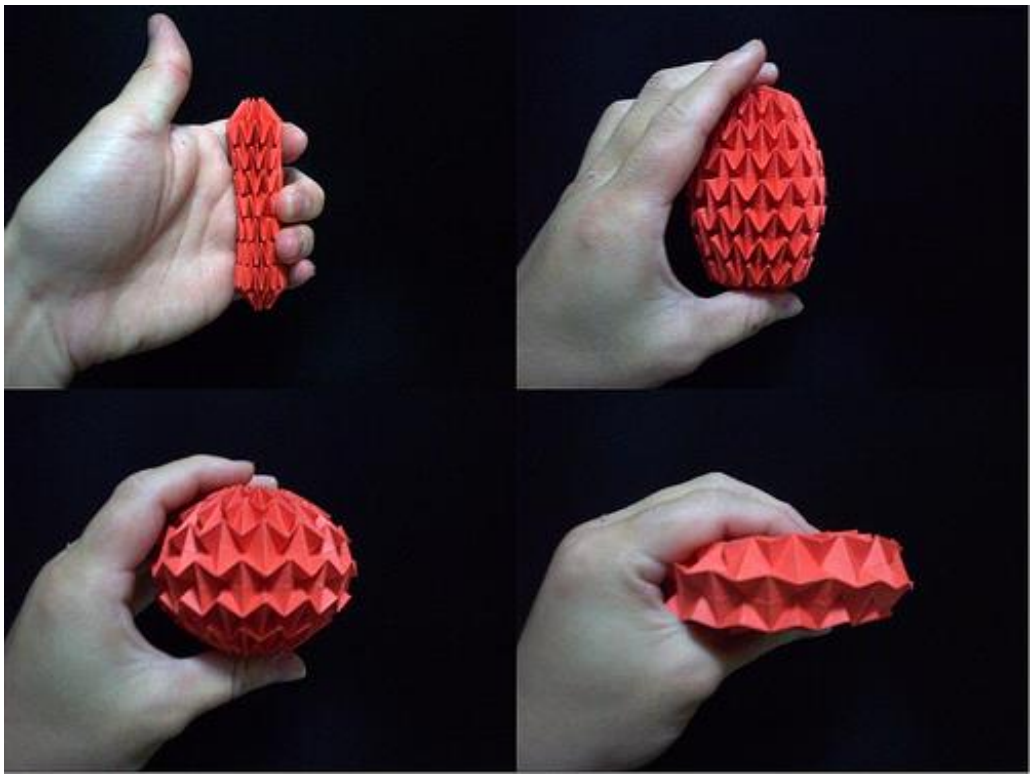

Figure 1.2. Different morphologies of origami magic ball structure.

Magic ball structure can deform into sphere or cylinder when force applied axial or radial, respectively. Kinetic behavior of dynamic origami can be applied to temporary shelters, retractable roofs and space structures, etc. Rigid origami is a branch of origami that deformability is enabled by the high degree of folding/unfolding at the creases, while the facets between creases do not experience deformation. Figure 1.3 shows an example of rigid origami named Miura-Ori fold.

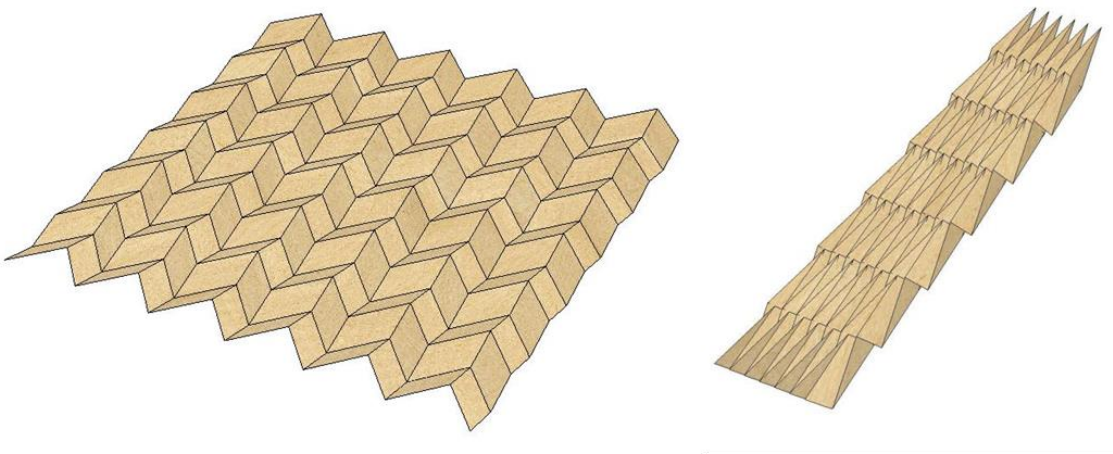

Figure 1.3. Two morphologies of Miura-Ori pattern. Left picture shows stretched state and right picture shows compressed state.

The crease patterns of the Miura fold form a tessellation of the parallelograms. The creases lie along straight lines in one direction. Each parallelogram forms the mirror reflection of its neighbor across each crease. In the other direction, creases are zigzag shape like and each of zigzag creases consist only mountain folds or valley folds. Miura-ori structure can be completely deformed in one direction without causing any deformation on facets. Conversely, facets in non-rigid origami will bend or twist to accommodate global deformation like the Chinese dragon in Figure 1.1(b).

Recently, origami, providing the ability to create versatile 3D stable configurations from 2D sheets, has been transformed by mathematicians, scientists, and engineers to utilize the folded objects' deformability and compactness (*2-21*).

Notable progress has been made in the area of origami theory, particularly on methods and tools to design origami models and to understand folding and unfolding from a theoretical perspective. The most notable example in origami theory is the tree method developed by R. Lang and T. Meguro in the 1990s, which provides a powerful

design tool to create crease patterns (*1*). It was followed in subsequent years by more powerful design tools (*20, 22-25*). The success in origami design has inspired great interest in applying origami to engineering applications, where engineering materials (e.g., polymers), instead of paper, are used. In addition, the use of active materials has led to field of 'action origami' (*26*), or active origami (*17, 27*), with pioneering applications generated by this MURI team: M. Dickey demonstrated the use of light absorbing inks to create shape memory polymer-based hinges (*13*) (Figure 1.4(a)), later applied to self-folding antenna (*21*) and machines (*14, 15*); H. Qi integrated 3D printing with shape memory polymer to create four dimensional (4D) printed origami (Figure 1.4(b)) (*16, 17*). G. Paulino has designed a new origami structure that combines two origami design folding patterns (*18*) (Figure 1.4(c)). Functional devices, such as batteries made by origami is also demonstrated in this dissertation (*19*) .

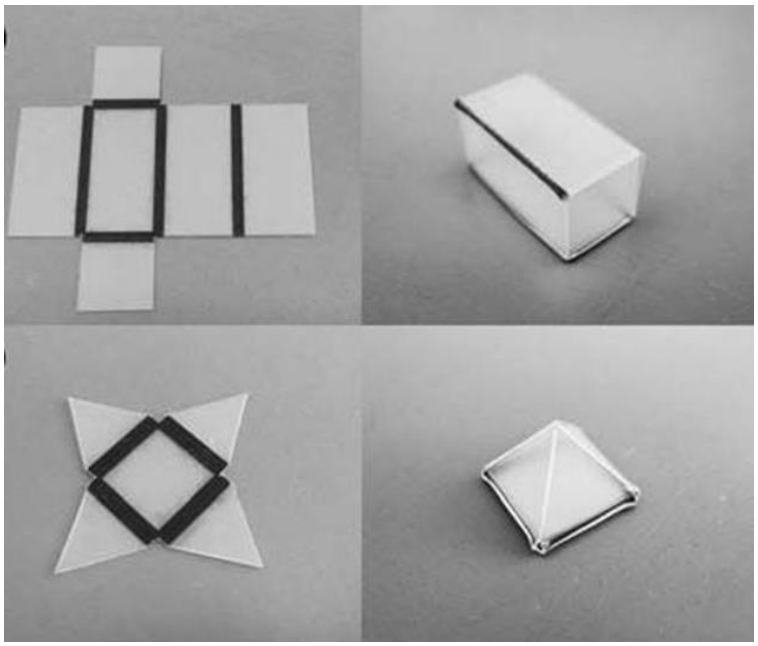

(a)

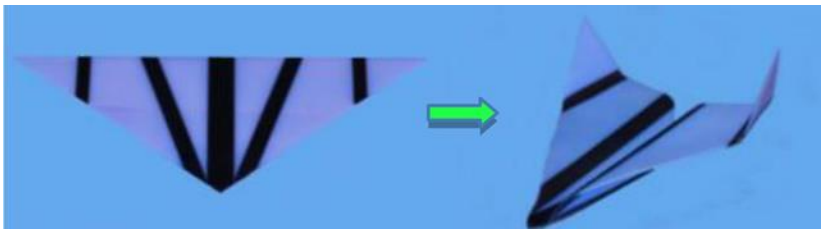

(b)

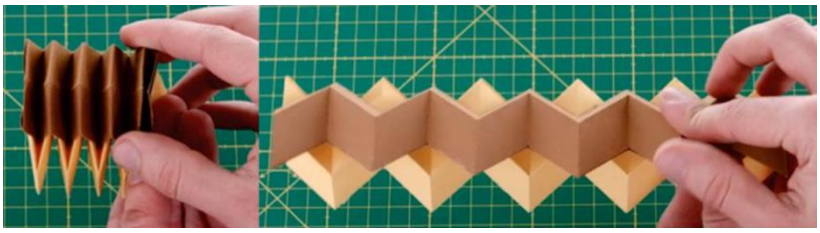

(c)

Figure 1.4. Examples of recent advances in active origami. (a) Folding of response to IR irradiation; (b) origami airplane by 4D printing; (c) origami tubes for reconfigurable structures and metamaterials.

However, origami-based foldable structures have two disadvantages. First, their foldability is limited from the folded state to the planar state. Although it can be tuned by different folding patterns, the same constraint is still prescribed by the planar state. Second, the folded state involves uneven surfaces, which introduces inconvenience when integrating with planar systems, though this issue can be somewhat circumvented.

1.2 Introduction of Kirigami - A Combination of Paper Cutting and Paper Folding

To overcome those disadvantages, another approach is introduced which combines folding and cutting, by the name of kirigami, to define patterns that form an even surface after stretching and the stretchability is not limited by the planar state. kirigami is symmetrical and an art of folding paper which is cut by scissors to make flower, paper doll, paper snowflake and other designs. Figure 1.5 shows the simple

process of making kirigami trees. This simple yet amazing form of art yields marvelous pieces that would showcase symmetry, consistency and balance.

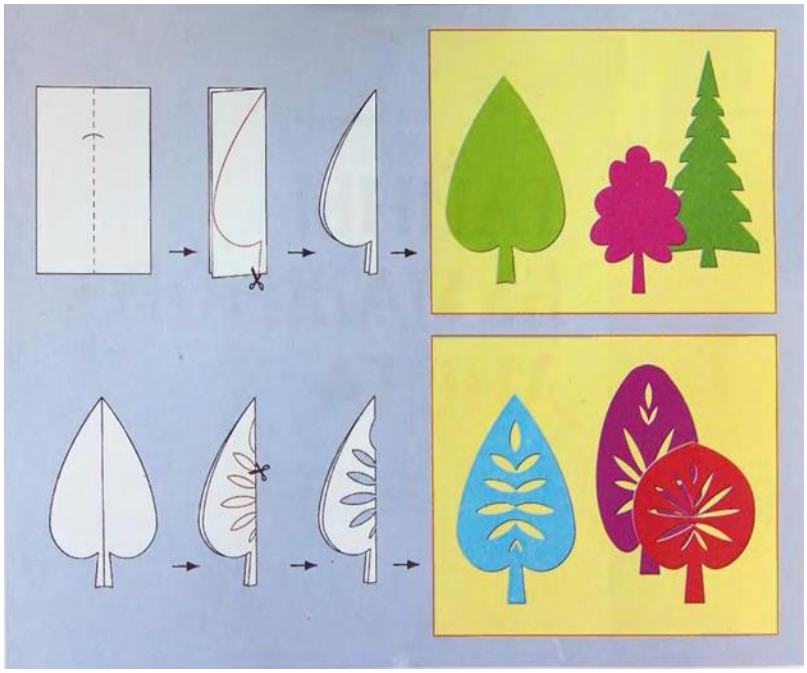

Figure 1.5. Steps of making kirigami trees.

In next two chapters, Origami and Kirigami patterns were successively utilized in making stretchable Lithium ion batteries, which both provide kirigami LIBs excellent electrochemical and mechanical characteristics.

CHAPTER 2

ORIGAMI LITHIUM ION BATTERIES

2.1 Background

Deformable energy storage devices are emerging as indispensable components for unconventional electronics devices that are able to survive significant degrees of deformation, mainly bending and stretching, with strain levels much greater than 1%. Examples include flexible displays (*28-31*), stretchable circuits (*32*), hemispherical electronic eyes (*33*), and the recently developed epidermal electronics (*34*). The energy storage devices present a significant challenge for developing a robust deformable system, since they must be seamlessly integrated with deformable functional devices and energy supplies with similar mechanical characteristics, including linear deformability (i.e., stretchability and compressibility), bendability, and twistability. For bending deformation, many thin film based energy solutions, such as supercapacitors (*35-38*) and batteries (*37, 39-43*) have been developed that take advantage of the inherently small strains (usually less than 1%) near the mechanical neutral planes (*44*). Recently a handful of efforts have been undertaken to develop stretchable energy sources. Stretchable supercapacitors using buckled carbon nanotube (CNT) macrofilms as electrodes (*45, 46*) and CNT-coated porous conductive textiles (*47*) have been developed with over 30% stretchability. Stretchable LIBs with over 100% stretchability and 50% areal coverage have been demonstrated that used serpentine interconnects and that were packaged by elastomeric materials (*48*). To date approaches that simultaneously achieve a high level of deformability (including linear stretching and compression, bending, twisting and their combinations in any order) with large areal coverage that are compatible with

commercially available manufacturing technologies have not been demonstrated. These attributes represent desired requirements to fully integrate energy storage devices with deformable electronics to reach system-level deformability in realistic applications.

Origami-based approaches represents a potentially game-changing alternative to enable deformability over existing methods that use elastomeric materials and mechanically designed structures such as buckling and serpentine shapes. Using origami, the ancient art of paper folding, compact deformable three-dimensional structures can be created from two-dimensional sheets through high degrees of folding along pre-defined creases,. Origami-based approaches have recently been pursued in several practical applications, including a foldable telescope lens (*5*) for space exploration and in heart stents (*2*).

In this dissertation, an approach to enable origami LIBs with the attributes of extreme mechanical deformability was reported, including significant system-level linear and areal deformability large twistability and bendability, and up to 74% areal coverage. Furthermore, commercially standard packaging technologies were used in the origami LIBs, which when combined with other deformable electronic devices, may lead to direct practical applications.

2.2 Experiment and Results

2.2.1 Battery Design Using Miura Folding

Figure 2.1 illustrates the origami LIB concept. Starting from conventional planar LIBs (Figure 2.1(a)) consisting of many layers, including current collectors, anode and cathode, separator and packaging, the origami LIBs were realized by folding these layers based on specific origami patterns of Miura-ori (*49*). In the Miura-ori pattern, shown in

Figure 2.1(b), many identical parallelogram faces are connected by ‘mountain’ and ‘valley’ creases. Depending on the difference of angles between adjacent ‘mountain’ and ‘valley’ creases, the Miura-ori can be either almost completely compressible in one direction (lower-left of Figure 2.1(b), and referred to as ‘45^{o} Miura folding’ hereafter) or collapsible in two directions (lower-right of Figure 2.1(b), and referred to as ‘90^{o} Miura folding’ hereafter). Despite the overall high-level of deformability that can be realized, the parallelogram faces themselves remain undeformed because the folding and unfolding of the creases maintains the faces in a rigid configuration. This class of origami pattern is appropriately called rigid origami, where deformability at the system-level is prescribed by the creases while the base or substrate materials making the origami pattern do not experience large strain except at the creases.

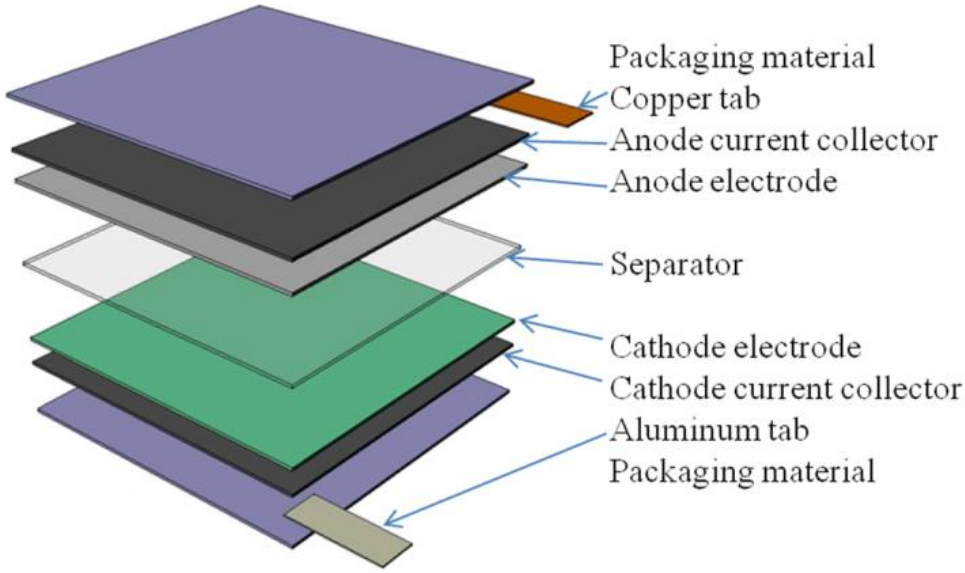

(a)

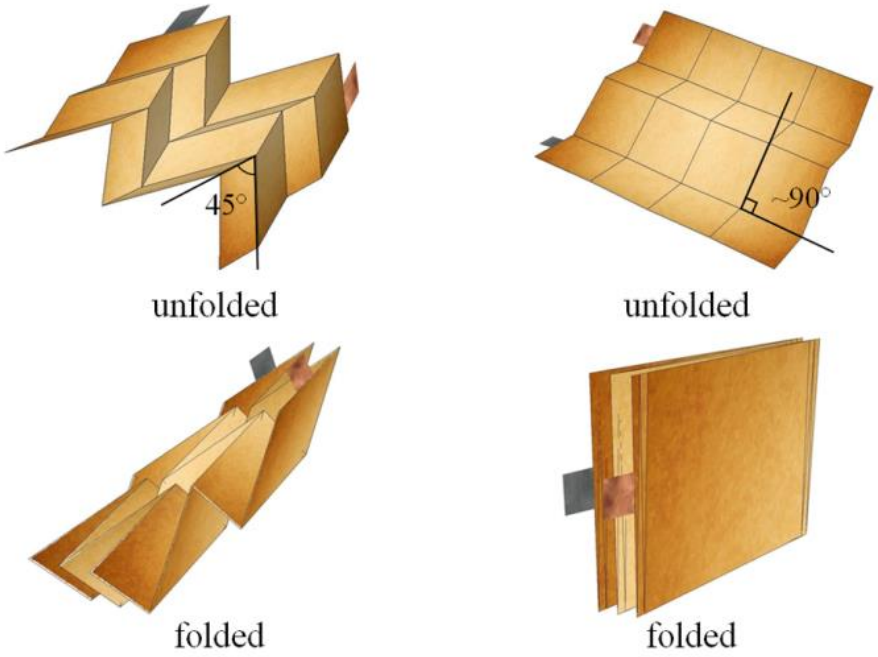

(b)

Figure 2.1. Concept of origami LIBs (a) exploded view of the multilayer structure of conventional LIBs in the planar state. (b) two examples of origami LIBs using Miura folding. The lower left pictures refer to 45^{o} Miura folding in the unfolded and folded states, showing it can be completely compressed in one direction. The lower right pictures refer to 90^{o} Miura folding in the unfolded and folded states, showing it can be completed collapsed in biaxial directions.

In order to achieve good foldability and electrical conductivity at the creases after cyclic folding and unfolding, we adopted CNT coated paper as the current collectors upon which we deposited active material layers (*37, 50*). Figures 2.2(a) and 2.2(b) show the optical and scanning electron micrographs (SEM) of this paper current collector, which was produced by coating thin and porous laboratory Kimwipes (Kimtech Science, Kimberly-Clark) with CNT layers of ~40μm thickness after drying. The electrical resistance of this paper current collector on each side was about 5Ω per square. CNT-coated paper was prepared as the current collector on laboratory Kimwipes using P3

CNTs from carbon solutions as described in our previous work (*50*). The final mass loading of CNTs on the CNT-coated paper was ~0.8 mg cm^{-2}. Cathodes and anodes were prepared by depositing $LiCoO_2$ (LCO, Sigma-Aldrich) and $Li_4Ti_5O_{12}$ (LTO, MTI Corp.) slurries onto the CNT-coated paper. Multilayer stacking structures as shown in Figure 2.1 were prepared, with the aluminized polyethylene (PE) (Sigma-Aldrich) as the packaging material, CNT-coated papers as anode and cathode current collectors, LTO and LCO as anode and cathode electrodes, respectively, polypropylene (Celgard 2500) as separator, and 1 M $LiPF_6$ in EC:DMC:DEC (4:2:4) as electrolyte. The mass ratio for LTO:LCO was fixed at ~1.6. Three layers of anode electrode connected with a copper (Cu) tab, separator soaked in electrolyte, and cathode electrode connected with an aluminum (Al) tab were placed in an aluminized/PE bag and assembled in an Argon filled glovebox.

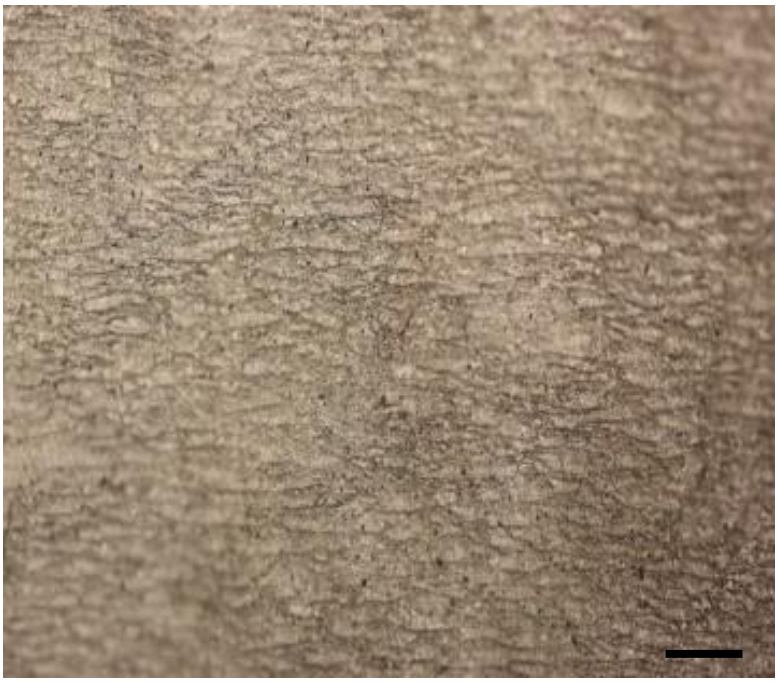

(a)

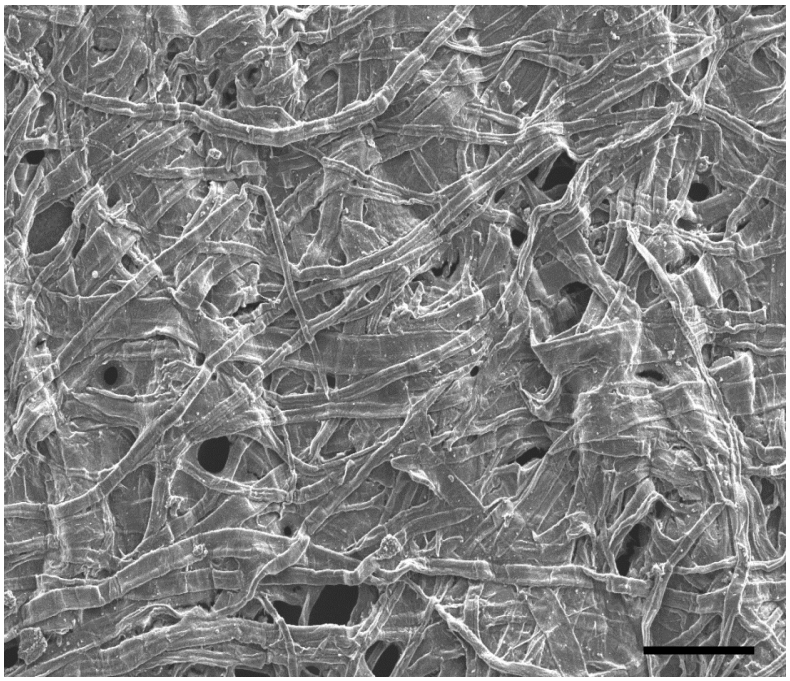

(b)

Figure 2.2. Origami LIBs using CNT-coated paper current collectors (a) Optical and (b) SEM of CNT-coated paper current collectors. Scale bar in (a) is 2 mm. Scale bar in (b) is 100 μm.

Then the assembled battery cell (shown in Figure 2.3) was folded using the desired origami patterns (Figure 2.1) in an ambient environment.

Figure 2.3. Optical image of an assembled LIB. Scale bar is 2 cm.

The thickness of the assembled LIB cell was 380 μm. Figures 2.4(a) and 2.4(b) provide optical and SEM images of as-coated anode in the regions of a crease.

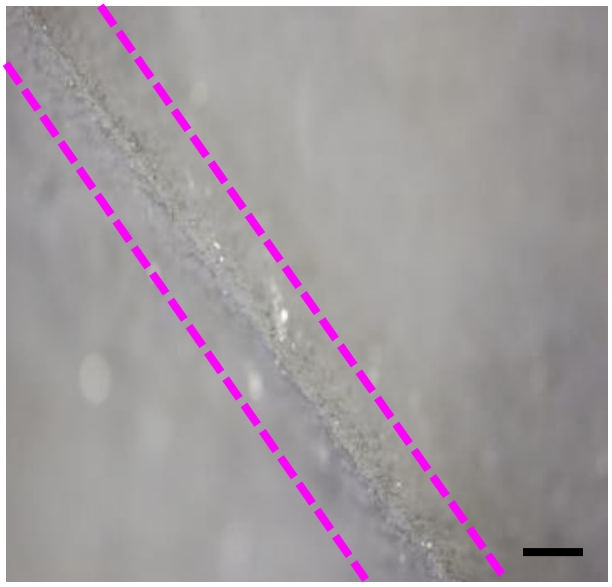

(a)

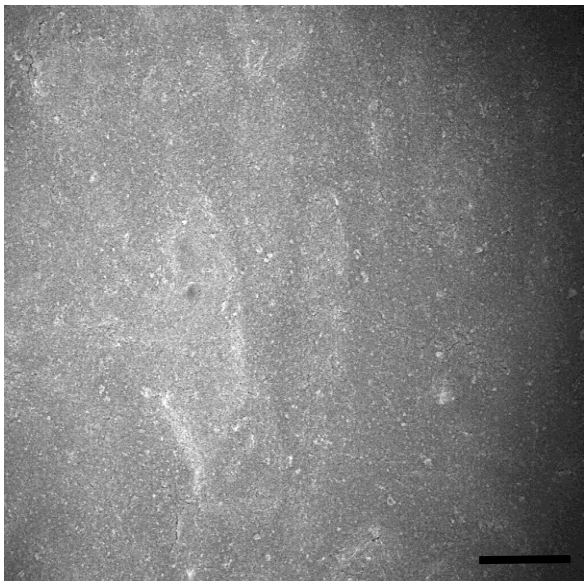

Figure 2.4. As-coated LTO anode electrode in (a) optical and (b) SEM images in a region of crease, as indicated by magenta dashed lines. Scale bar in (a) is 2 mm. Scale bar in (b) is 100 μm.

Figures 2.5(a) and 2.5(b) provide optical and SEM images of as-coated cathode electrodes in the regions of a crease, showing that there were no apparent cracks or delamination of active materials from the electrodes, as compared to the planar regions. Moreover, it was verified that the electrical resistance of the electrodes prior to and after folding in the origami pattern (without packaging) remained unchanged. Galvanostatic charge and discharge tests were performed using a battery testing unit (Arbin Instruments).

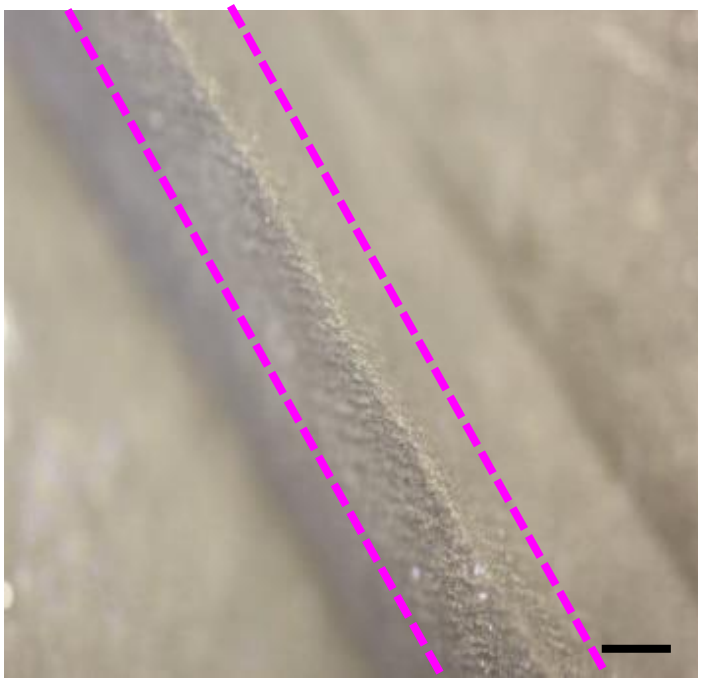

(a)

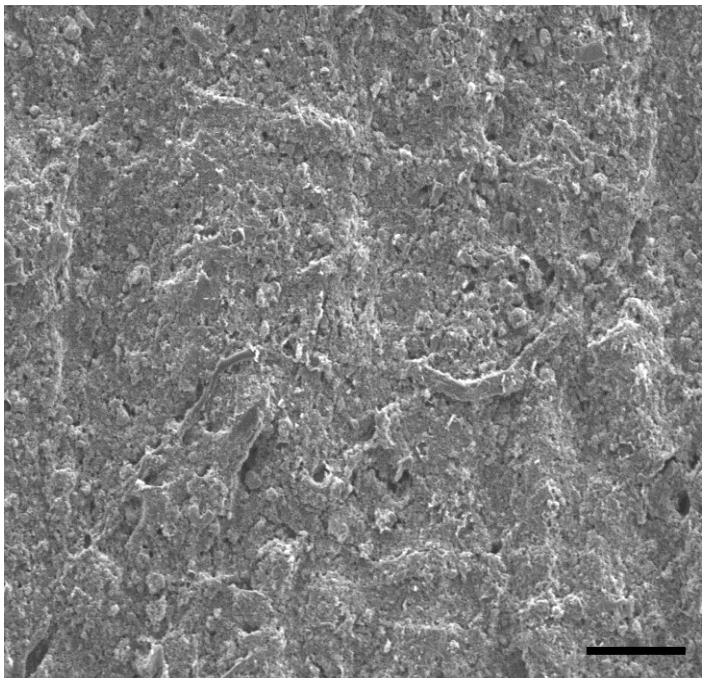

(b)

Figure 2.5. As-coated LCO cathode electrode in (a) optical and (b) SEM images in a region of crease, as indicated by magenta dashed lines. (e) and (g) show the entire region of the crease. Scale bar in (a) is 2 mm. Scale bar in (b) is 100 μm.

2.2.2 Electrochemical and Mechanical Characteristics of Origami LIBs

Figures 2.6(a) and 2.6(b) show the pictures of the planar and completely compressed configurations, respectively. The dotted black lines highlight the area of anode and cathode electrodes, which provides over 74% areal coverage.

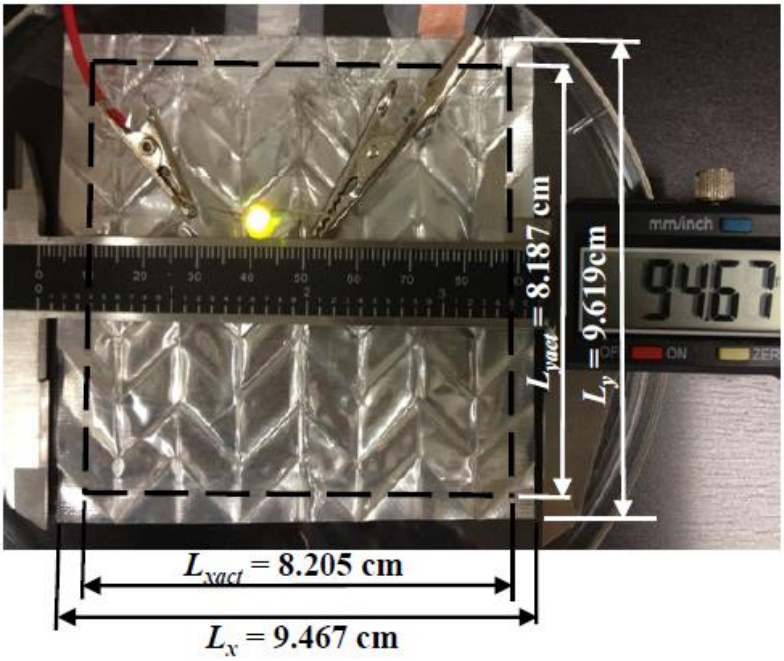

(a)

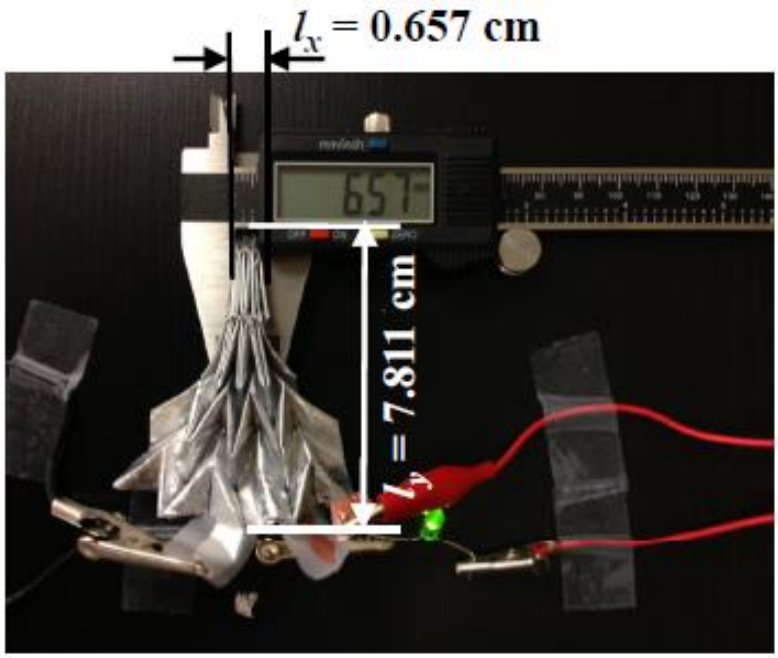

(b)

Figure 2.6. Characteristics of the origami LIBs using 45^o Miura folding (a) Photograph of the origami battery in the completely unfolded state, where the battery was used to power a light-emitting diode (LED). The size of the origami battery is $L_x \times L_y$ and the active electrodes cover the area of $L_{xact} \times L_{yact}$. The areal coverage is 74%. (b) Photograph of the origami battery operating a LED in its completely compressed state. The size of the battery is $l_x \times l_y$.

Electrochemical properties of the LIB in its planar state (for the 1st, 5th, and 10th cycles) and completely compressed state (for the 30th, 50th, 100th, and 150th cycles) under a current density of 20 mA g-1 are shown in Figure 2.7

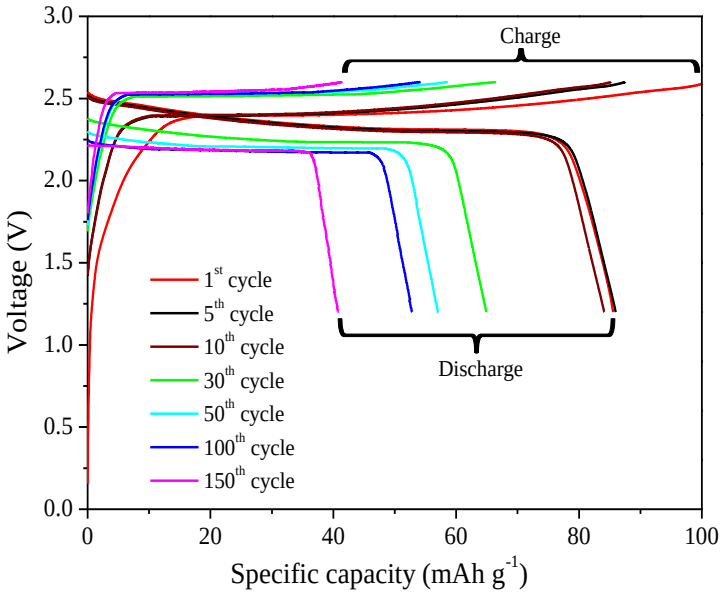

Figure 2.7. Electrochemical characterizations. Galvanostatic charge and discharge of the origami LIBs using 45^{o} Miura folding at the planar state (1st, 5th, and 10th cycles) and the completely compressed state (30th, 50th, 100th, and 150th cycles). Well-defined plateaus at around 2.35V were observed. The mass loading of LCO (specific capacity 145 mAh g-1) and LTO (specific capacity 160 mAh g-1) were 102 mg and 169 mg, respectively, which gave the specific capacity at its compressed configuration of 85.5 mAh g-1 for the present current density (or equivalently C/7).

The areal capacity for the planar and completely compressed states as a function of charge rate was examined by performing galvanostatic cycling under two current densities (Figure 2.8).

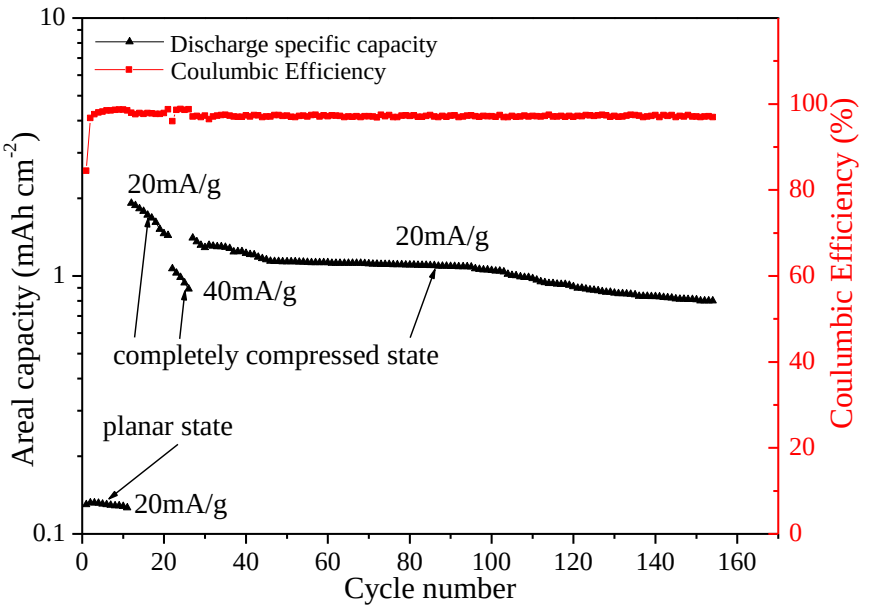

Figure 2.8. Capacity retention (left axis, black) and Coulumbic efficiency (right axis, red) as a function of cycle number for two current densities, 20 mA g^{-1} and 40mA g^{-1}.

At a current rate of 20 mA g^{-1}, the areal capacity was about 0.2 mAh cm^{-2} for the first 11 cycles when the origami battery was in its planar unfolded state, and increased to 1.4-2.0 mAh cm^{-2} for the next 10 cycles when the origami battery was completely compressed. When the current rate was increased to 40 mA g^{-1} for the next 5 cycles, the areal capacity remained at 0.8-1.0 mAh cm^{-2}. When the current density was reduced back to the initial level of 20 mA g^{-1}, the areal capacity nearly recovered to 1.3-1.4 mAh cm^{-2}, and remained at above 1.0 mAh cm^{-2} for up to 110 cycles, which indicates reasonably good areal capacity. Observed decrease of the capacity after many cycles (i.e., two months of continuous charging/discharging) may be attributed to factors related to leakage in the present aluminized PE packaging, which can be improved with better seals. The present areal capacity for the completely compressed state of 1.0-2.0 mAh cm^{-2}

could be further increased by adding more active materials (e.g., LTO and LCO) to obtain thicker electrodes. However, such a modification might reduce the rate capacity and could also lead to difficulty in folding and higher localized strain at the creases.

The mechanical characteristics of the fully charged LIBs using 45^{o} Miura folding were examined. As shown in Figure 2.9, under folding and unfolding, the output voltage remained steady at 2.65 V (same as the highest voltage shown in Figure 2.7 for the fully charged LIB), even up to 1,340% linear deformability with respect to its completely compressed state.

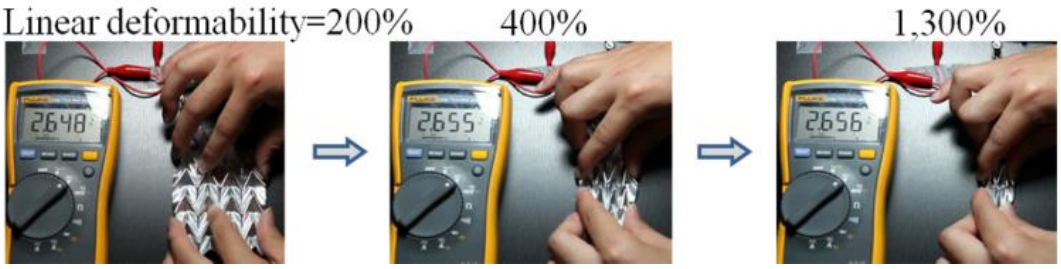

Figure 2.9. Photograph of linear deformation (i.e., folding and unfolding) of an origami LIB while it was connected to a voltmeter.

Electrochemical impedance spectroscopy (EIS) studies were performed during the first discharge cycle before and after the mechanical deformation and no significant changes in the impedance were found before and after mechanical deformation (Figures 2.10(a) and 2.10(b)). The EIS studies were performed by applying a small perturbation voltage of 5 mV in the frequency range of 0.1 Hz to 100 kHz during the first discharge cycle before and after mechanical deformation, using a Gamry Echem Analyst. The analysis of the impedance spectra was conducted using equivalent circuit software provided by the manufacturer.

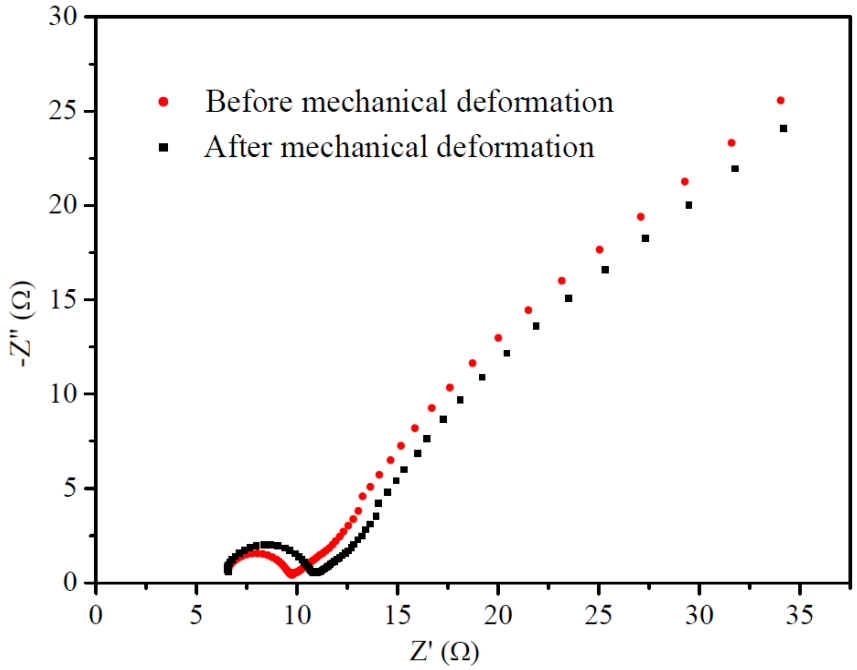

(a)

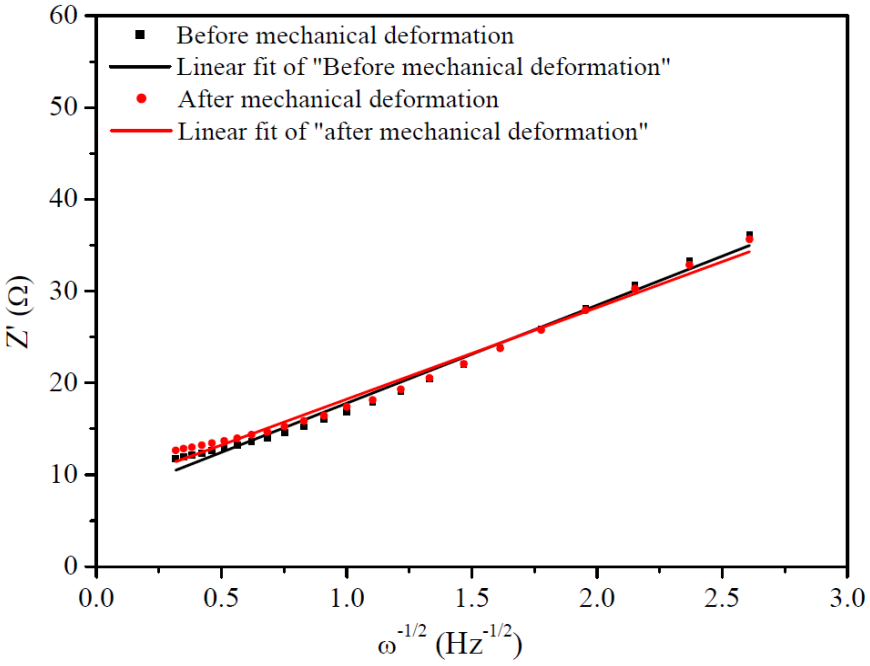

(b)

Figure 2.10. EIS analysis during the first discharge cycle before and after the mechanical deformation (completely compressed followed by bending and twisting). EIS studies were performed by applying a small perturbation voltage of 5 mV in the frequency range

of 0.1 Hz to 100 kHz. Typical impedance spectrum with high-to-middle frequency range semicircle and a relative straight line representing the low frequency range for both curves were observed. There are not significant changes in the impedance before and after mechanical deformation. (a) Nyquist plot shows that the surface resistance after mechanical deformation slightly increases, which may be due to the presence of tiny cracks and thickness change of solid electrolyte interface (SEI) layer. (b) The slope of the straight line in low frequency domain (Warburg resistance) in the EIS spectra corresponds to solid state Li-ion diffusion in the active electrodes (e.g., LTO and LCO). It is found that Li-ion diffusion does not show significant change before and after mechanical deformation.

The linear deformability $\varepsilon_{deformability}$ is defined by using the dimensions marked in Figures 2.6(a) and 2.6(b) as, $\varepsilon^{x}_{deformability} = \frac{L_x - l_x}{l_x}$ for the *x*-direction, and $\varepsilon^{y}_{deformability} = \frac{L_y - l_y}{l_y}$ for the *y*-direction. l_x and l_y are the dimensions for the completely compressed state (Figure 2.8), and L_x and L_y are the dimensions for the unfolded states, with the extreme case being the planar state shown in Figure 2.6(a). In other words, the deformability is defined for the unfolded states using the completely compressed state as the reference. This definition allows for the quantification of the extreme capacity for deformation in Miura folding, namely from the completely compressed state to the planar state through unfolding, and vice versa, from the planar state to completely compressed state through folding. Using the measured dimensions shown in Figures 2.6(a) and 2.6(b), the origami LIB with 45^{o} Miura folding demonstrated up to 1,340% linear deformability in the *x*-direction going from the completely compressed state to the planar state. The areal deformability ε_{Areal} can be correspondingly defined as $\varepsilon_{Areal} = \frac{L_x L_y - l_x l_y}{l_x l_y}$, and was found to reach 1,670%. These levels of linear and areal deformability significantly surpass those previously reported in stretchable interconnects, devices, supercapacitors and batteries.

Figure 2.11 shows the maximum output power of the origami battery as a function of linear deformability, $\varepsilon^{x}_{deformability} = \frac{L_x - l_x}{l_x}$, under different cycles of linear deformation.

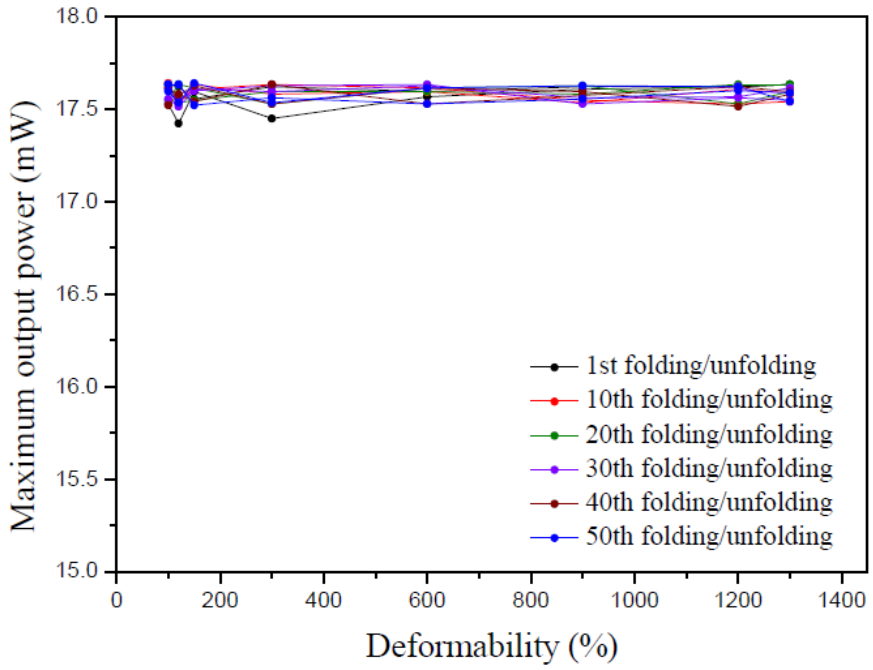

Figure 2.11. Maximum output power of the origami LIB as a function of linear deformability over 50 cycles of folding and unfolding.

Here the internal resistance of the battery was about 79Ω. Up to a linear deformability $\varepsilon^{x}_{deformability}$ of 1,340% and over 50 linear deformation cycles, the output power was quite stable and showed no noticeable decay. The maximum output power of the fully charged battery was calculated using $\frac{1}{2}\frac{V}{R_i}$, where V is the open circuit voltage and R_i is the internal resistance as a function of system-level mechanical strain and cycles of mechanical loading. When the origami battery was subjected to different mechanical loading, values of voltage were measured using a voltmeter. This stable performance is attributed to good bonding quality between the electrodes and CNT-coated paper current

collectors, the unchanged electrical resistance of the CNT-coated paper current collectors upon linear deformation, and vanishing deformation at the parallelogram faces for rigid origami. The output power of 17.5 mW is sufficient to operate commercial light-emitting diode (LED). As shown in the supporting information (Figures 2.12(a)-(c)), LEDs driven by this LIB do not show noticeable dimming upon cyclic linear deformation, even for a higher deformation rate (~ 0.2 ms^{-1}).

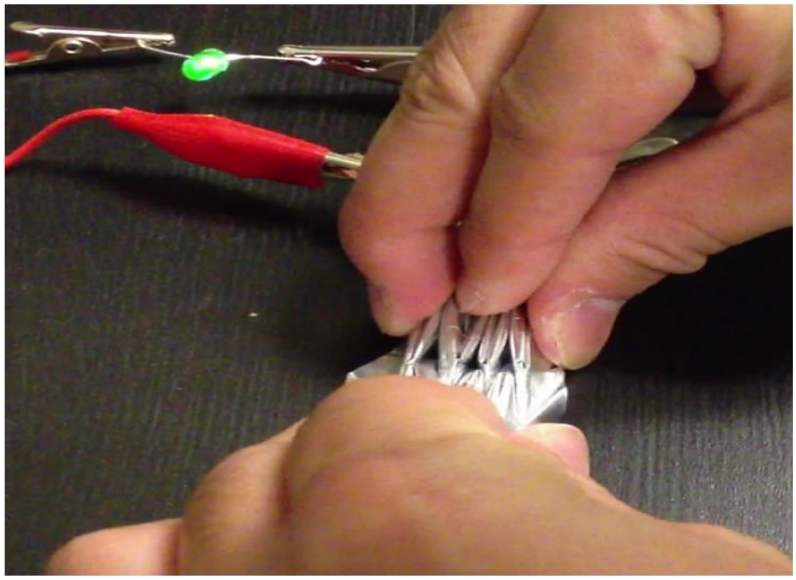

(a)

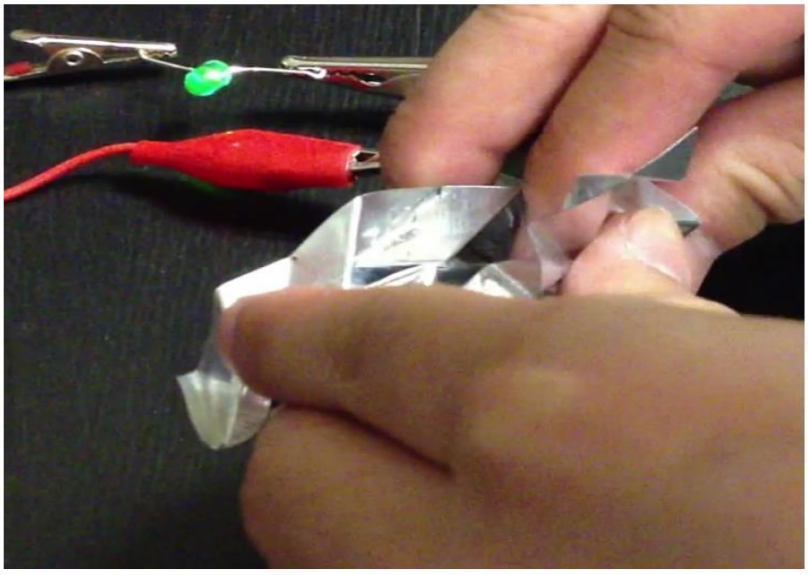

(b)

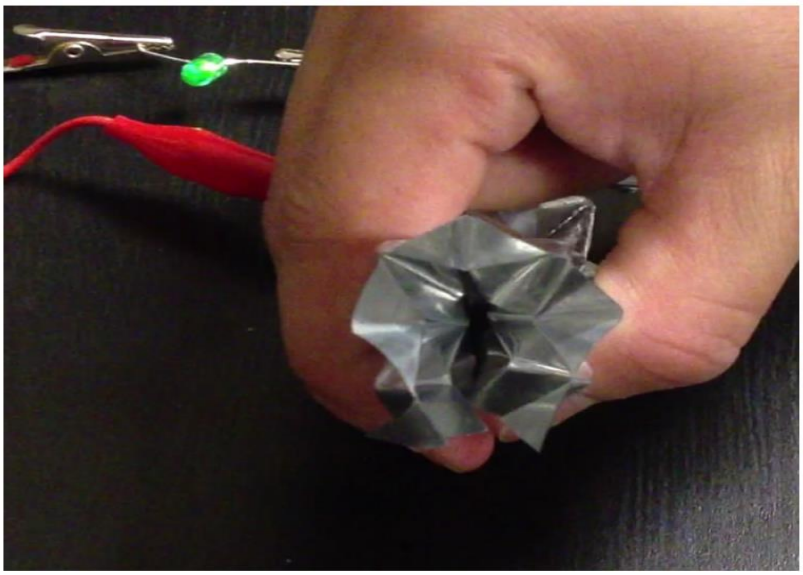

(c)

Figure 2.12. An origami LIB using 45^{o} Miura folding is lighting up a LED while (a) linear deformation with over 1,300% strain, (b) twisting, and (c) bending.

Figure 2.13 shows the optical photograph of the same origami battery subjected to torsion after tension. It is clear that the origami battery using 45^{o} Miura folding can bear large torsion of up to 10.8^{o}cm-1 twisting angle without degradation of the output voltage.

Figure 2.13. Twisting an origami LIB while it was connected with a voltmeter.

Fig. 2.14 shows the maximum output power of the battery as a function of twisting angle for various twisting cycles in which a similar stability to that for tension was repeatedly observed.

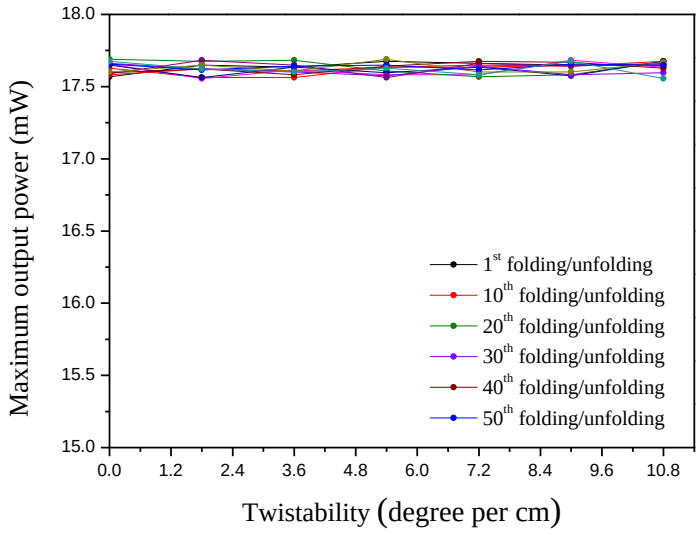

Figure 2.14. Maximum output power of the origami battery using 45^{o} Miura folding as a function of twisting angle for various twisting cycles.

It is relevant to note that for a rigid origami, there are (n−3) degrees of freedom with n as the number of edges at one vertex (*51, 52*), which gives only one degree of freedom for the Miura pattern (n =4). Therefore, an ideally rigid Miura folded device can only bear linear deformation, and torsion will cause strain on those parallelogram faces. Finite element analysis (FEA) was conducted by using a recently developed approach and the strain contour is shown in Figure 2.15 for 10^{o} per unit cell twisting angle, where the size of a unit cell is the shortest length of one parallelogram face. It is clear that the strain for most of the area was vanishingly small with strain levels on the order of 0.001%.

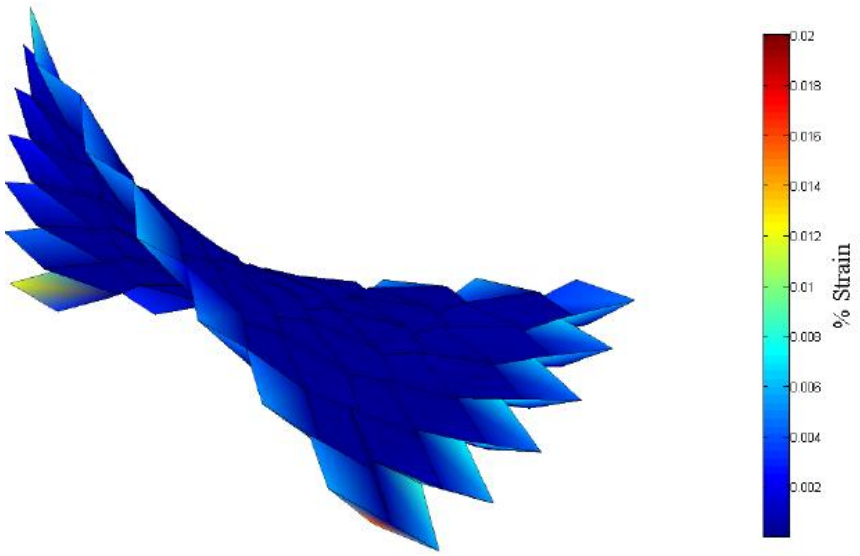

Figure 2.15. Finite element results of the strain contour of a 45^{o} Miura pattern subjected to twisting with twisting angle of 90^{o} per unit cell.

After tension and torsion, the same device was subjected to bending, as shown in Figure 2.16. Similar mechanical robustness was observed as for tension and torsion: the origami battery could be wrapped around an index finger (with bending radius of about 0.83 cm) without a large change in the output voltage.

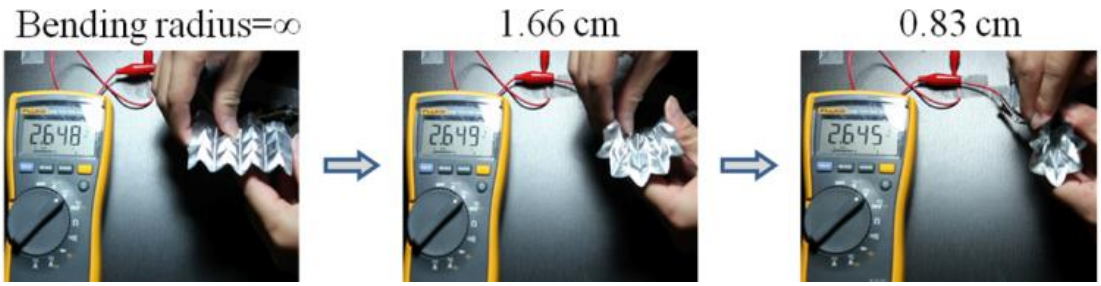

Figure 2.16. Bending an origami LIB while it was connected with a voltmeter.

Figure 2.17 shows the maximum output power versus bending radius under different bending cycles and the power stability was repeatedly observed. Bending is similar to twisting as it causes strain on the parallelogram faces.

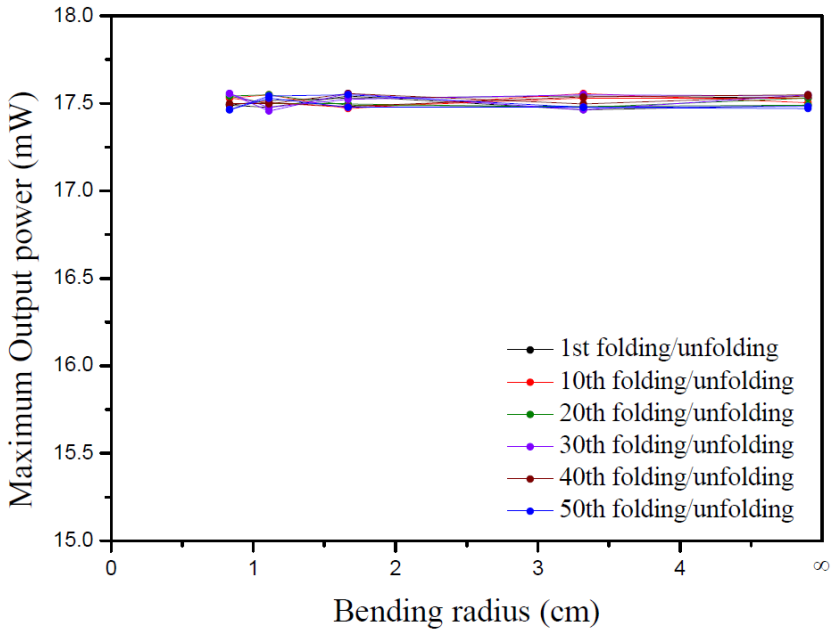

Figure 2.17. Maximum output power of the origami battery using 45^{o} Miura folding as a function of bending radius for various bending cycles.

Figure 2.18 shows the strain contour of a bent Miura folding pattern with bending radius of 2 unit cells, showing that the strain was again quite small - on the order of 0.1%.

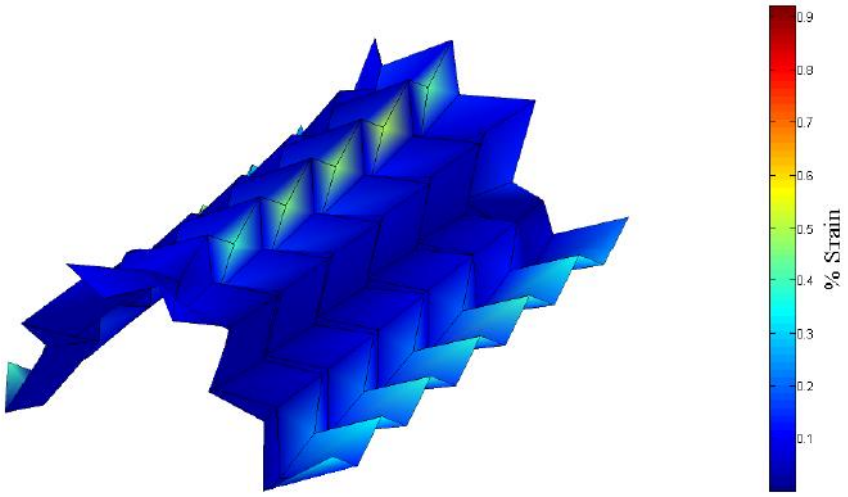

Figure 2.18. Finite element results of the strain contour of a 45^{o} Miura pattern subjected to bending with bending radius of 2 unit cell.

In additional to the 45^{o} Miura folding pattern that can achieve significant linear deformability and bear tension, torsion and bending, a Miura folding pattern with 90^{o} angle (lower right panel of Fig. 1) was also utilized. This folding can be completely collapsed in biaxial directions and thus can reach very high areal deformability. As shown in the supporting information (Figure 2.19), for a 90^{o} Miura pattern with 5×5 parallelogram faces, the areal deformability ε_{Areal} can be as high as 1,600%, which can be further increased using a denser Miura pattern, such as 10×10 pattern. It is thus believed that this approach can achieve unprecedented areal deformability compared to all other fabrication methods, to the best of our knowledge.

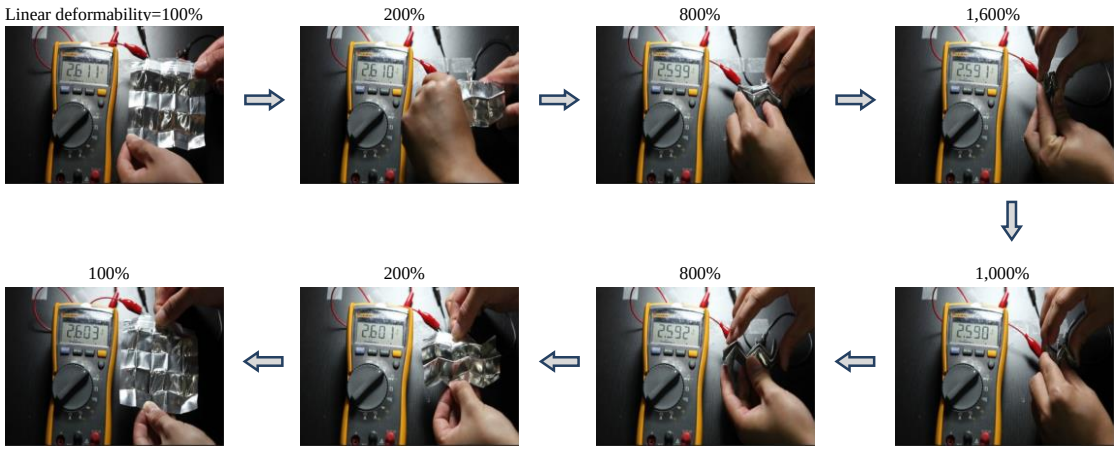

Figure 2.19. An origami battery using 90^{o} Miura folding subjected to folding and unfolding and connected to a voltmeter.

2.2.3 Comparison of Origami LIBs with LIBs Using Conventional Active Materials and Current Collectors

The superior deformability of origami LIBs is mainly due to two mechanisms, namely the use of rigid origami that can achieve deformability through folding and unfolding at creases and does not strain the rigid faces, and the use of CNT-coated paper current collectors that survive at the creases and form good adhesive between electrodes. Figures 2.20(a)–(d) show the optical and SEM images of the lithiated LTO and LCO active layers, respectively, in the regions of a crease, after the cyclic electrochemical characterization and mechanical loads (linear deformation, twisting, and bending up to more than 100 times) were performed. Although there were some voids and cracks observed, particularly in the lithiated LTO films at the paper current collector, there was no noticeable delamination from the CNT-coated current collectors as compared with those before lithiation as shown in Figures 2.4 and 2.5. This behavior could be explained by the interconnected fabric-like and porous structure of the CNT-coated paper current

collectors (as shown in Figures 2.2(a) and (b)) providing a continuous network for electron transport and significantly enhancing the bonding to the anode and cathode active material layers. To verify this hypothesis, we utilized conventional electrodes and current collectors (i.e., graphite on Cu foil for the anode and LCO on Al foil for the cathode) to assemble a LIB cell followed by 45^{o} Miura folding. Here the same multilayer stacking structures as shown in Figure 2.1 were used to fabricate the origami LIBs using the conventional materials, where the aluminized PE (Sigma-Aldrich) was the packaging material; Cu and Al as the anode and cathode current collectors, respectively; graphite and LCO as anode and cathode electrodes, respectively, polypropylene (Celgard 2500) as separator, and 1 M $LiPF_6$ in EC:DMC:DEC (4:2:4) as electrolyte. Anode slurries were prepared by mixing the graphite (Fisher Scientific), carbon black (Super C45) ,Carboxymethyl cellulose (Fisher Scientific), Styrene Butadiene Rubber (Fisher Scientific) and DI water with a ratio of 76:2:1:2:160 by weight. Then the slurry was uniformly coated on Cu with 20 μm in thickness (CF-T8G-UN, Pred Materials International, Inc.), and then dried on a hot plate at 120 ^{o}C for 5 hours. Cathode slurries were prepared by mixing the LCO, PVDF (MTI Corp.), Carbon black (Super C45) and N-Methyl-2-pyrrolidone solvent (CreoSalus) with a ratio of 18:1:1:20 by weight. Then the slurry was uniformly coated on Al with 10 μm in thickness (Reynolds Wrap), and then dried on a hot plate at 120 ^{o}C for 5 hours. A mass ratio for graphite:LCO was around 2:0. Then the anode and cathode electrodes were subject to press to make condensed electrodes. Then the same packaging process as discussed in the main text was used.

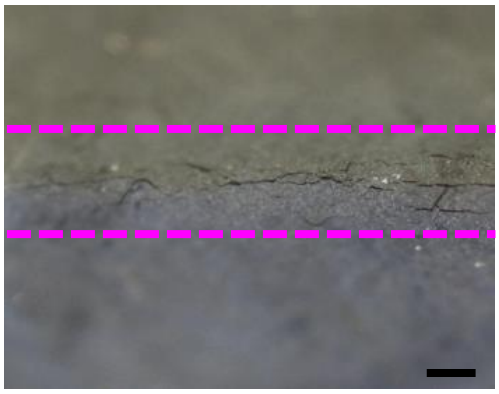

(a)

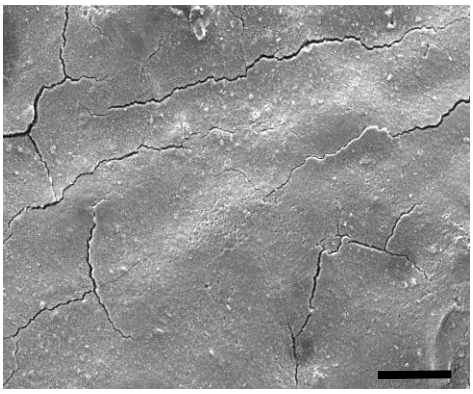

(b)

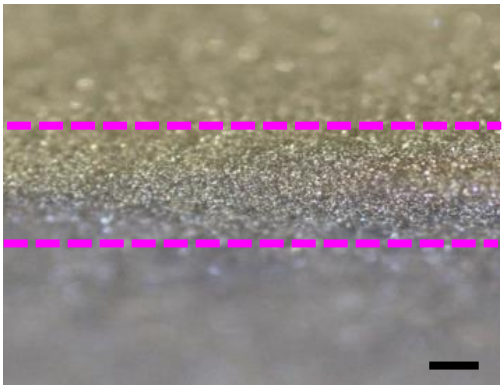

(c)

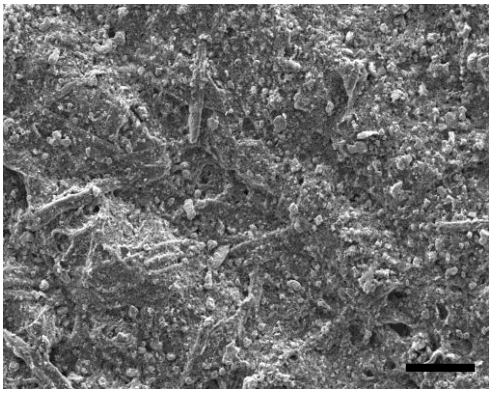

(d)

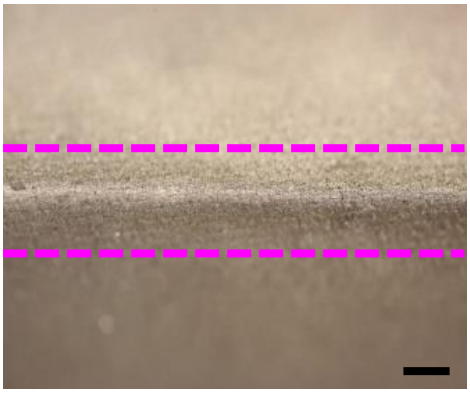

(e)

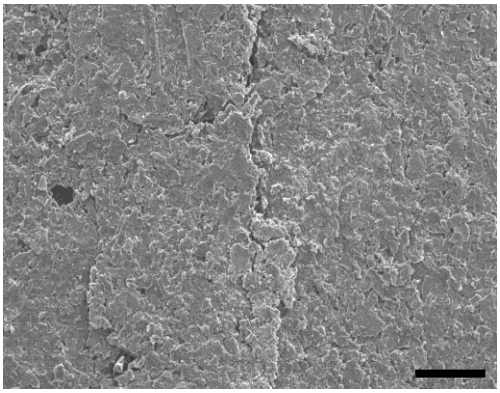

(f)

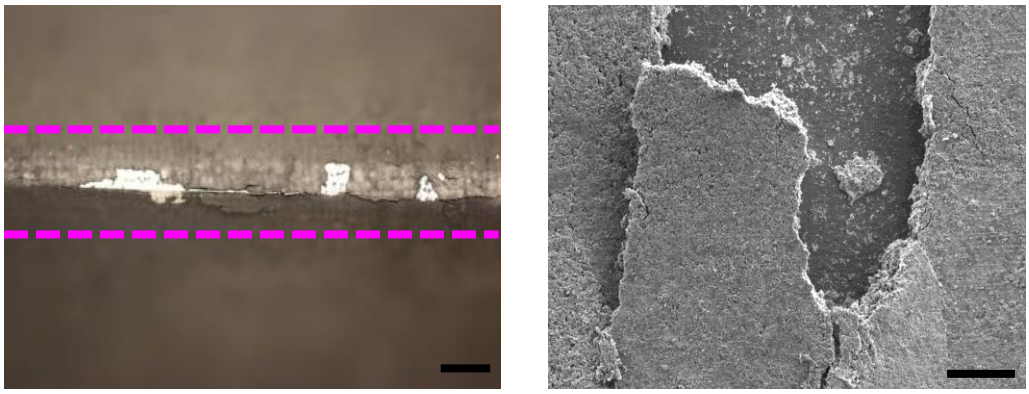

(g) (h)

Figure 2.20. Comparison of paper based origami LIBs with conventional materials based LIBs. For an origami LIB using CNT-coated paper current collectors, after cyclic electrochemical charge and discharge, as well as many cycles of mechanical loads, (a) optical and (b) SEM of LTO electrodes in the region of a crease as indicated by the magenta dashed lines; (c) optical and (d) SEM images of LCO electrodes in the region of a crease as indicated by the magenta dashed lines. (b) and (d) show the entire region of the crease. For an origami LIB using conventional collectors (Cu and Al), after one electrochemical charge and without mechanical loads, (e) optical and (f) SEM images of graphite electrodes on Cu current collector in a region of crease as indicated by the magenta dashed lines; (g) optical and (h) SEM images of LCO electrodes on Al current collector in a region of crease as indicated by the magenta dashed lines. (f) and (h) show the entire region of the crease. Scale bars in a, c, e and g are 2 mm. Scale bars in b, d, f and h are 100 μm.

The assembled LIB cell using conventional materials had a similar thickness (360 μm) as the origami LIBs and the detailed processes are provided in the supporting information. Figures 2.21(a)–(d) show optical images of the graphite and LCO electrodes before and after folding.

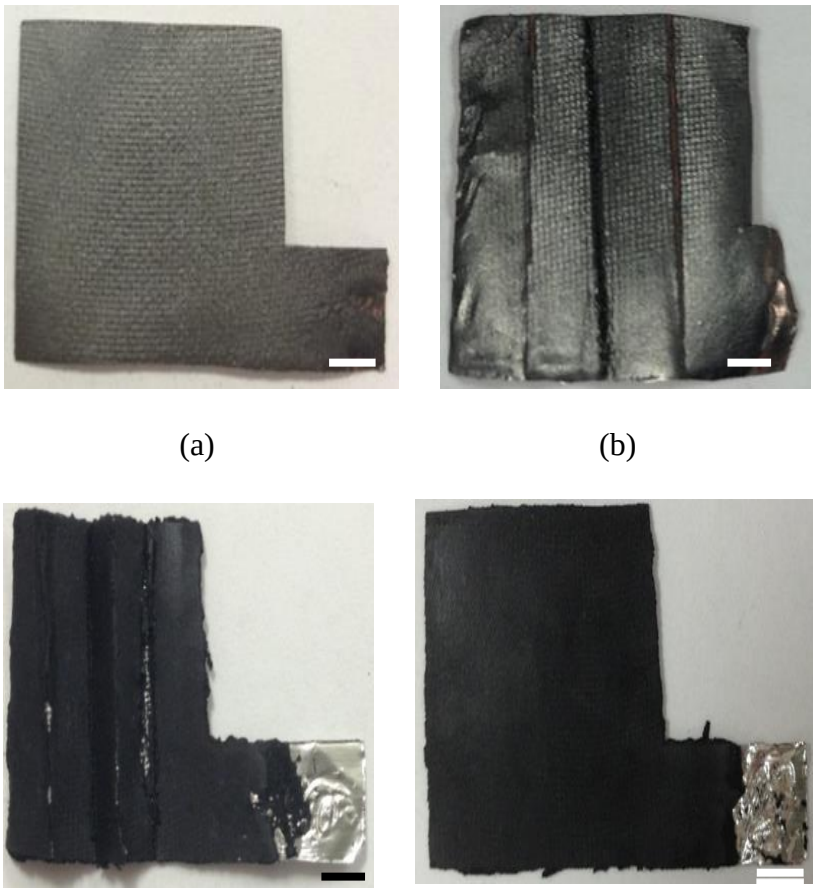

Figure 2.21. Optical images of graphite electrodes (a) prior to and (b) after folding, before change. Optical images of LCO electrodes (c) prior to and (d) after folding, before charge. Scale bars in a, b, c and d are 2 mm.

It is apparent that some active materials were lost from the conventional current collectors, even before charging. Figures 2.20(e)–(h) show the optical and SEM images of the lithiated graphite and LCO, respectively, in the regions of a crease after the first charge and without mechanical loading. It is now apparent that more electrode materials have been lost, which indicates insufficient thin film bonding at the creases. Figure 2.22 shows that the energy capacity of the origami battery using conventional materials decayed about 10% after 100 cycles of linear deformation, in contrast to the steady

capacity observations for the origami LIBs using CNT-coated paper current collectors. Therefore, good conductivity and strong bonding after cyclic folding and unfolding are two key attributes for origami LIBs.

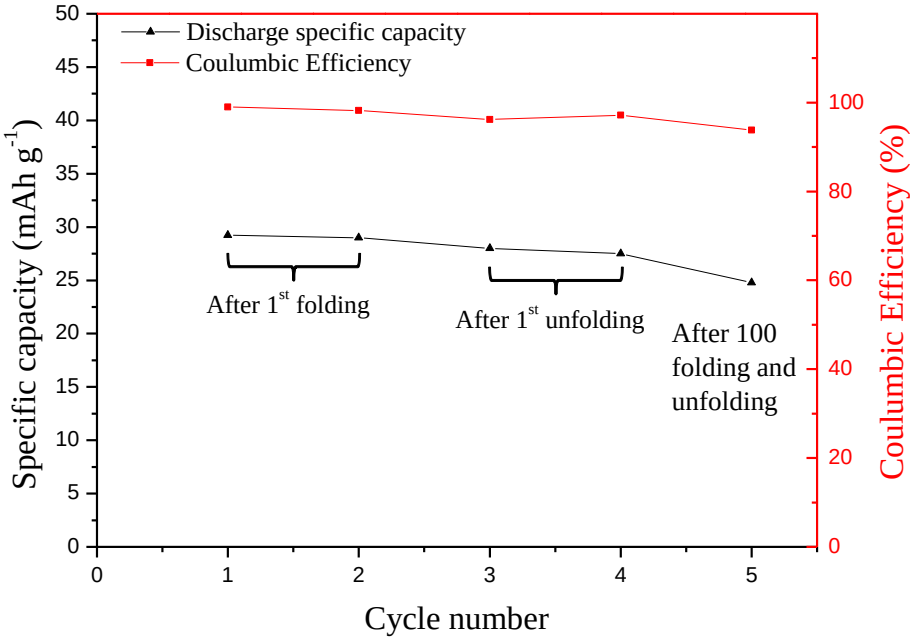

Figure 2.22. Capacity of an origami battery using 45^{o} Miura folding and conventional active materials and current collectors.

2.3 Discussion

The origami design concept enables LIBs with unprecedented mechanical deformability including folding, unfolding, twisting and bending. The use of CNT-coated paper as current collectors provides stable electrochemical characteristics under cyclic mechanical deformations. The fabrication process for origami LIB cells, including slurry mixing, coating and packaging, is completely compatible with mainstream industrial processing. At a high level, the strategy of fusing the art of origami with materials science, and energy storage devices provides a dramatically alternative approach for

powering deformable (including, flexible, foldable, stretchable and curvilinear) electronics ranging from displays, sensors, solar cells and antenna.

CHAPTER 3

KIRIGAMI BASED STRETCHABLE LITHIUM ION BATTERIES

3.1 Background

Energy storage devices, such as supercapacitors and LIBs that are able to sustain large strains (much greater than 1%) under complex deformations (for instance, bending, tension/compression, and torsion) are indispensable components for flexible, stretchable electronics, and recently emerging wearable electronics, such as flexible displays (*29-31*, *53*), stretchable circuits (*32*), hemispherical electronic eyes (*33*), and epidermal electronics (*34*). Various approaches have been employed to achieve flexible and stretchable energy storage devices, such as thin film based bendable supercapacitors (*35-38*) and batteries (*37, 39-43*), buckling-based stretchable supercapacitors (*45, 46*), and island-serpentine-based stretchable LIBs (*48*). Recently, an origami-based approach was adopted to develop highly foldable LIBs, where standard LIBs were produced followed by designated origami folding (*54*). The folding endows the origami LIB with a high level of foldability by changing the LIB from a planar state to a folded state. However, the previously developed origami-based foldable devices (*54*, *55*)have two disadvantages. First, their foldability is limited from the folded state to the planar state. Although it can be tuned by different folding patterns, the same constraint is still prescribed by the planar state. Second, the folded state involves uneven surfaces, which introduces inconvenience when integrating with planar systems, though this issue can be somewhat circumvented. The approach introduced here combines folding and cutting, by the name of kirigami, to define patterns that form an even surface after stretching and the stretchability is not limited by the planar state. The folding and cutting lead to high level of stretchability

through a new mechanism, ‘plastic rolling’, which has not yet been discovered and utilized in the stretchable electronics/systems. The LIBs were produced by the standard slurry coating (using graphite as an anode and $LiCoO_2$ as a cathode) and packaging procedure, followed by a designated folding and cutting procedure to achieve a particular kirigami pattern. Over 150% stretchability has been achieved and the produced kirigami LIBs have demonstrated the ability to power a Samsung Gear 2 smart watch, which shows the potential applications of this approach. The kirigami-based methodology can be readily expanded to other applications to develop highly stretchable devices and thus deeply and broadly impact the field of stretchable and wearable electronics.

3.2 Experiment and Results

3.2.1 Battery Design Using Kirigami Patterns

Three kirigami patterns are utilized, as illustrated in Figure 3.1, with (a) a zigzag-cut pattern, (b) a cut-N-twist pattern, and (c) a cut-N-shear pattern. The zigzag-cut pattern (Figure 3.1(a)) represents one of the most commonly seen kirigami patterns and is produced by cutting a folded stack of foil asymmetrically between the neighboring creases, which creates zigzag-liked cuttings in the longitudinal direction. The zigzag pattern can be stretched beyond its length in the planar state, which is the advantage of kirigami. To accommodate stretching, the out-of-plane deformation (or equivalently, buckling) occurs at the vicinity of cuts. The level of stretchability depends on the length of the cut and is a function of buckling amplitude. To eliminate the out-of-plane deformation, one of the advantages of kirigami compared with the origami pattern, the cut-N-twist pattern (Figure 3.1(b)) is utilized, in which a folded stack of foil is symmetrically cut at all creases, and then unfolded to a planar state, followed by twisting

at the two ends. The twisted structure is shown in the bottom panel of Figure 3.1(b) and analogous to a twisted telephone cord. This pattern represents a locked structure in the sense that the out-of-plane deformation, induced by stretching, is constrained and rotation occurs at the cuts to accommodate stretching. The packing density of cut-N-twist pattern is defined by the width of each face. To increase the packing density, the cut-N-shear pattern (Figure 3.1(c)) is introduced, where folding is employed after symmetric cutting and then the folded structure is subjected to shear, thus the packing density doubles compared with that for the cut-N-twist pattern. The stretching is also achieved by the rotations of the cuts and no out-of-plane deformation is involved.

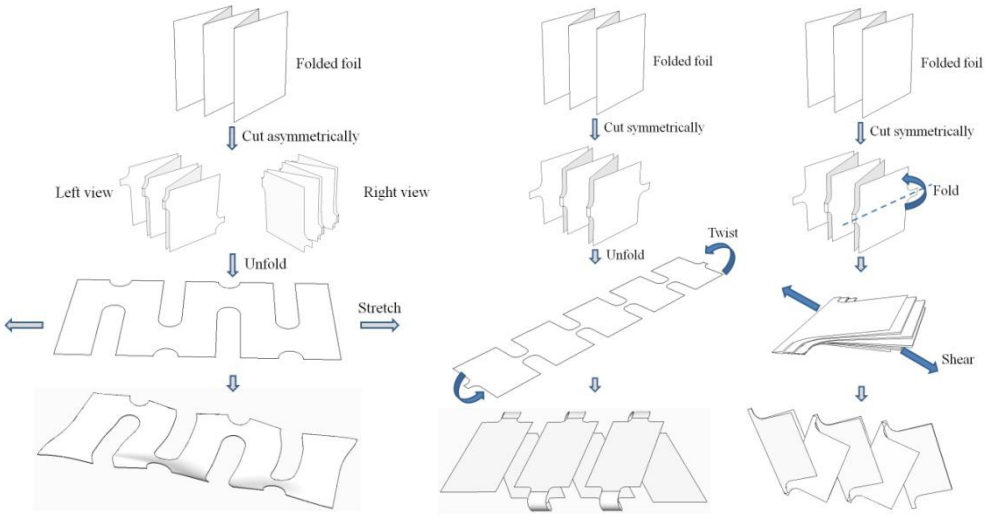

(a) (b) (c)

Figure 3.1. Illustrations of three kirigami patterns. (a) A zigzag-cut pattern, where the out-of-plane deformation occurs to accommodate stretching. (b) A cut-N-twist pattern, where the rotation is involved to accommodate stretching and no out-of-plane deformation. (c) A cut-N-shear pattern, where the packing density doubles compared with that of the cut-N-twist pattern. Rotation is involved to accommodate stretching and no out-of-plane deformation.

Now we demonstrate kirigami LIBs, specifically the LIBs using cut-N-twist here and cut-N-shear and zigzag-cut patterns in the Supporting Information. Conventional

materials and approaches of LIBs preparation were used, with graphite (Fisher Scientific Inc.) and LCO (MTI Corp.) as the anode and cathode active materials, respectively. Conventional slurries of these active materials were prepared and used to coat the current collectors, where Cu and Al served as the anode and cathode current collectors, respectively. The Cu and Al current collectors were first cut to the three patterns (Figure 3.1) based on the specific geometries as provided in the Figure 3.2, followed by slurry coating.

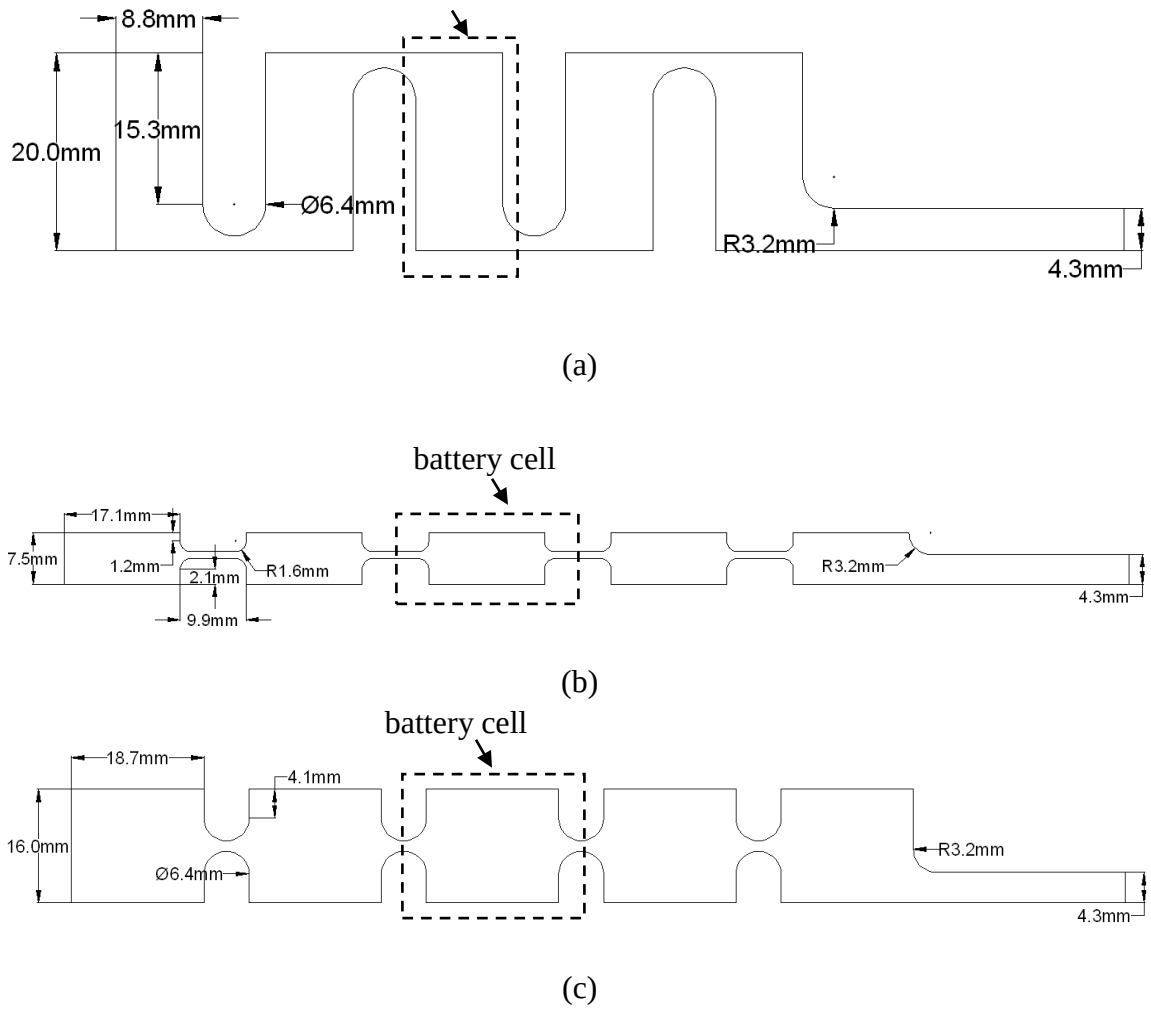

Figure 3.2. Geometries of the three kirigami batteries. (a) Zigzag-cut pattern, (b) cut-N-twist pattern, and (c) cut-N-shear pattern. The dashed line shows a battery cell.

To prepare packaging, polypropylene (Celgard 2500) as separator and aluminized PE (Sigma-Aldrich) as packaging materials were also cut using the same kirigami pattern; thus all the layers of a LIB have the same pattern. Then these layers were perfectly laminated in the order of packaging material, cathode electrode, separator, anode electrode, and packaging material, and delivered to an Argon-filled glovebox for packaging. The impulse sealer was used to seal the sides of the each cell (Fig. 12) except one side for the electrolyte (1 M $LiPF_6$ in EC:DMC:DEC (1:1:1), MTI Corp.) injection, followed by sealing the last side of the battery cell. The key to achieve excellent packaging is that the cutting of all layers of a battery cell must be uniform and the alignment must be perfect. We have designed a customized puncher for cutting. The cutting quality can be significantly improved by using laser cutting in the future.

3.2.2 Electrochemical and Mechanical Characteristics

Figures 3.3-3.11 show electrochemical and mechanical characterization results for LIBs using cut-N-twist pattern.

Using the most compact state (Figure 3.3(a)) as the reference, Figure 3.3(b), displaying the LIB at its most stretched state, shows that the stretchability of a kirigami LIB is over 100%. It should be noted that there is no significant change on the thickness of this LIB between the most compact state (h = 1.31 mm) and at the most stretched state (h = 1.07 mm).

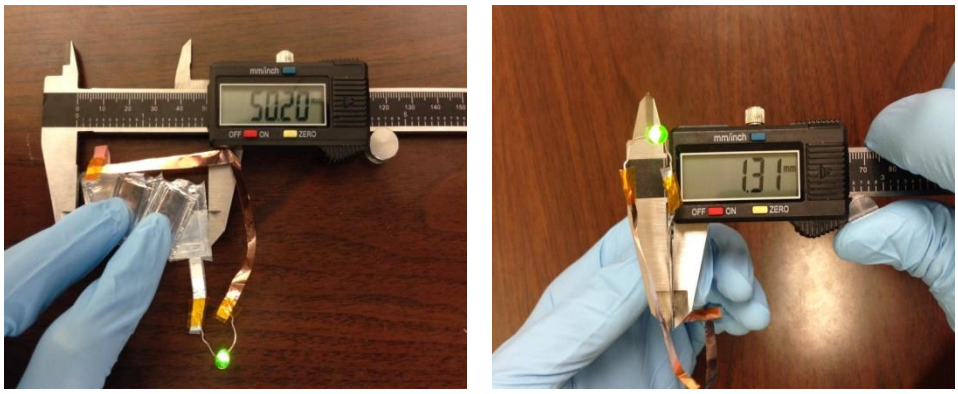

(a)

(b)

Figure 3.3. (a) Photograph of a LIB at its most compact state. (b) Photograph of a LIB at its most stretched state.

Figure 3.4 shows the electrochemical cycling results of a kirigami LIB at its most compact state (for the 1st to 5th cycles), followed by that at its most stretched state (for the 6th to 10th cycles), then that at its most compact state again (for the 11th to 15th cycles), and then that at its most stretched state again (for the 16th to 20th cycles), and finally that at its most stretched state (for the 21st to 100th cycles) under C/3 charge/discharge rate. Well-defined plateaus at around 3.7V are observed along with fairly stable charge/discharge behaviors under compact and stretched states.

The present mass loading (see caption of Figure 3.4) gives this kirigami LIB 30 mAh energy capacity.

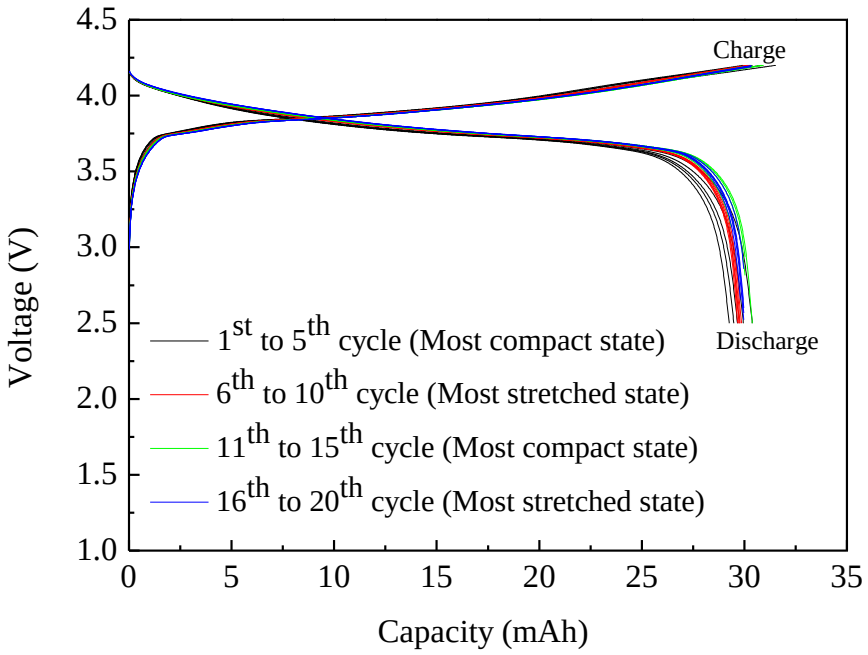

Figure 3.4. Galvanostatic charge and discharge at the most compact state (1st to 5th cycles), the most stretched state (6th to 10th cycles), the most compact state again (11th to 15th cycles), and the most stretched state again (16th to 20th cycles) under C/3 charge/discharge rate. The mass loading of LCO (specific capacity 145 mAh g-1) and graphite (specific capacity 372 mAh g-1) were 95 mg and 255 mg, respectively, which gave LIB the capacity of 30 mAh.

Figure 3.5 shows reasonable cyclic stability of the LIBs up to 100 cycles with over 85% capacity retention and 99.8% Coulombic efficiency. It should be emphasized that this result represents the stability of this kirigami LIB at mixed states, i.e., both compact and stretched states.

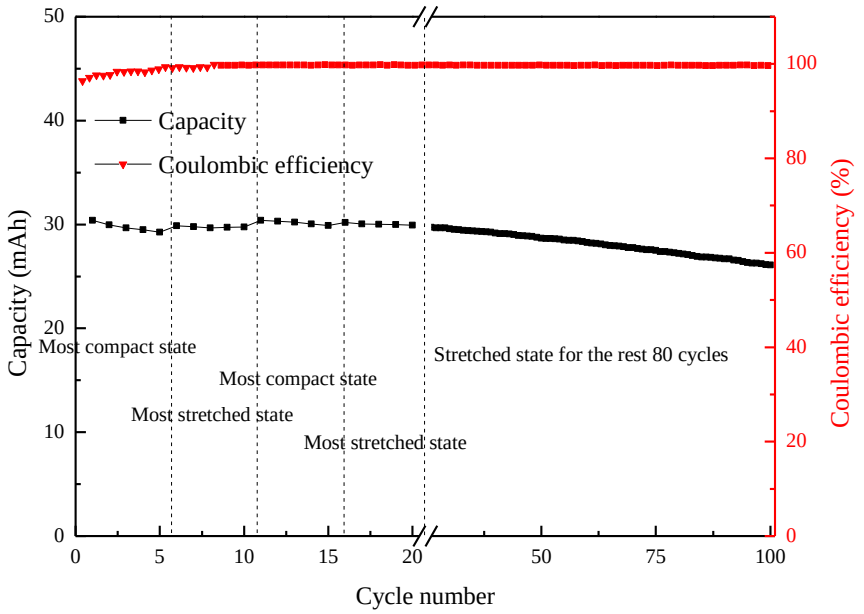

Figure 3.5. Energy capacity (left axis, black) and Coulombic efficiency (right axis, red) as a function of cycle number for C/3 charge/discharge rate. The mass accounts for all the materials involved in a cell, which is 1.49 g.

Figure 3.6 shows the rate performance of this kirigami battery when the charge/discharge rate varied in the sequence of C/3, C/2, C and C/3 again at both compact and stretched state. When discharge rates increase, as expected, the capacity decreases from 29.3 mAh for C/3 rate to 26.5 mAh for C/2 rate, and 21.4 mAh for discharge rate C. However, the capacity recovered to the 27.6 mAh when the discharge rate resumed to C/3 after 30 cycles charge/discharge at the both compact the stretched state under varies C-rates, which indicates great rate performance of this kirigami battery.

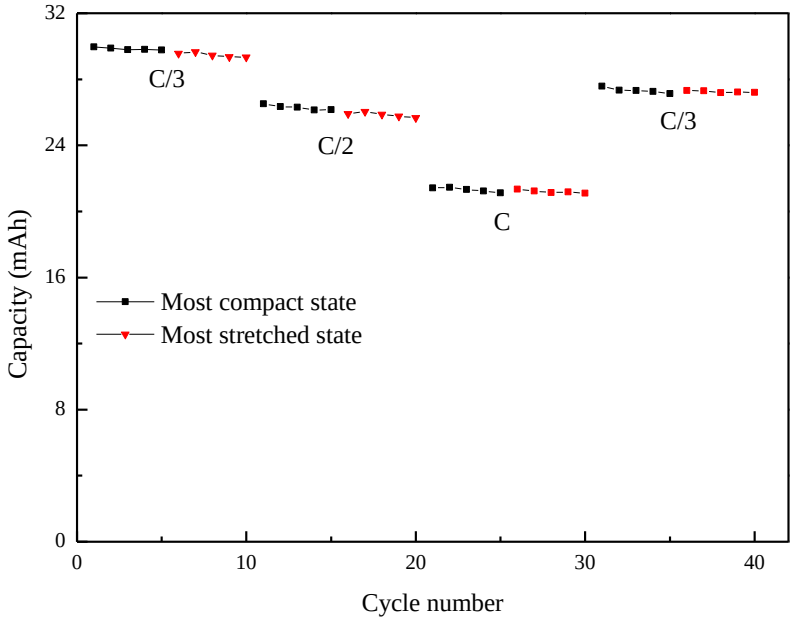

Figure 3.6. Rate performance when the charge/discharge rates varied from C/3, C/2, to C, and C/3 again for both compact and stretched states.

Figure 3.7 provides the results for EIS studies during the first discharge cycle at the most compact state before stretching and stretched state after 100 cycles of mechanical stretching. No significant changes in the impedance were found.

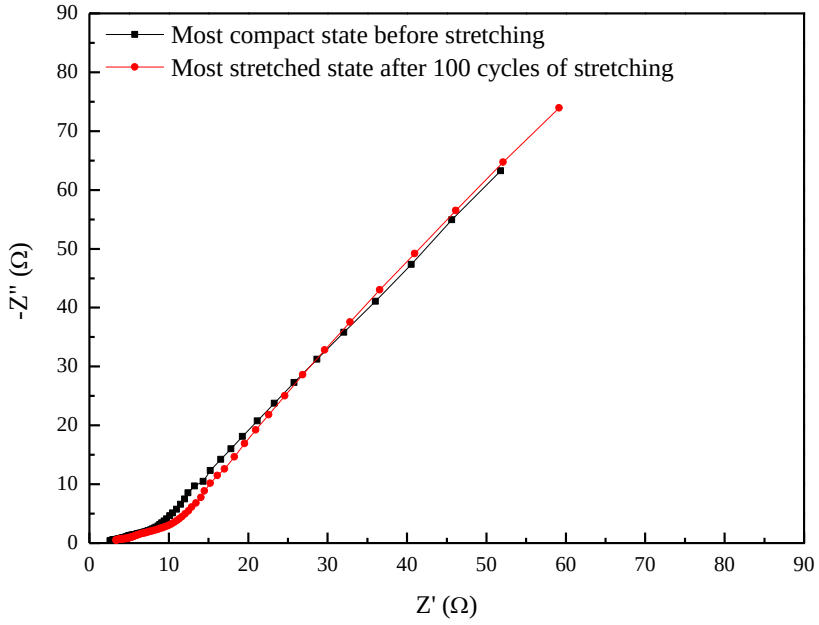

Figure 3.7. EIS analysis during the first discharge cycle at the most compact state before stretching and stretched state after 100 stretching cycles. EIS studies were performed by applying a small perturbation voltage of 5 mV in the frequency range of 0.1 Hz to 100 kHz. Typical impedance spectrum, with high-to-middle frequency range flat curve and a relative straight line representing the low frequency range, was observed. No obvious semicircle was observed because of the low internal resistant. There are not significant changes in the impedance before and after mechanical deformation.

The mechanical characteristics of the fully charged kirigami LIB using cut-N-twist are then examined. As shown in Figure 3.8, at different stretchability, the output voltage remained steady at 3.83 V.

Figure 3.8. Photograph of stretching a kirigami LIB while it was connected to a voltmeter.

Figure 3.9 shows the maximum output power of the kirigami LIB as a function of stretchability, $\varepsilon_{stretch}$, under different cycles of stretching. Here the internal resistance of the battery was measured to be about 1.8Ω. Over 1,000 stretching cycles and a stretchability $\varepsilon_{stretch}$ of up to 90%, it is found that the output power is stable and shows no noticeable decay. The maximum output power is 4.1 W and is sufficient to operate commercial LEDs. As shown in the Supporting Information, LEDs driven by this kirigami LIB do not show noticeable dimming upon cyclic stretching for a few hours.

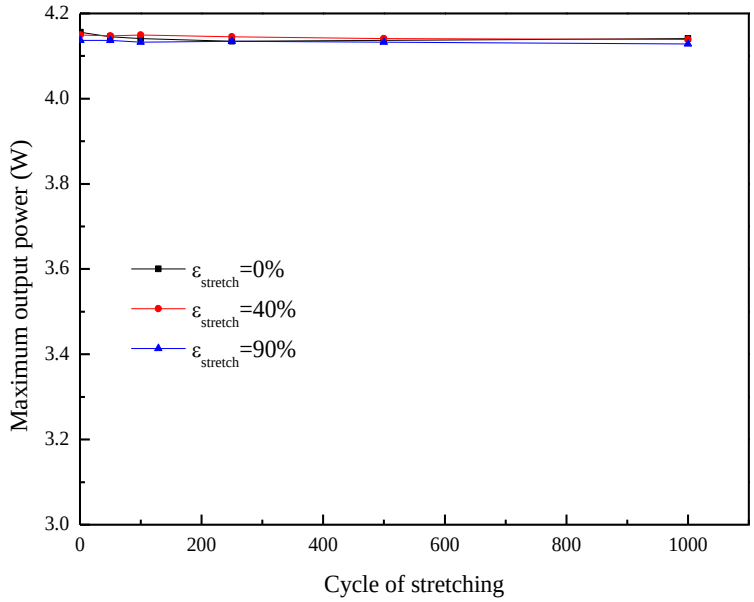

Figure 3.9. Maximum output power of the kirigami LIB as a function of stretchability over 1,000 cycles of stretches.

Figures 3.10(a) and 3.10(b) show the SEM images for the anode current collectors (e.g., Cu foil) at the cuts before charging, and after discharge and 100 cycles of mechanical deformation.

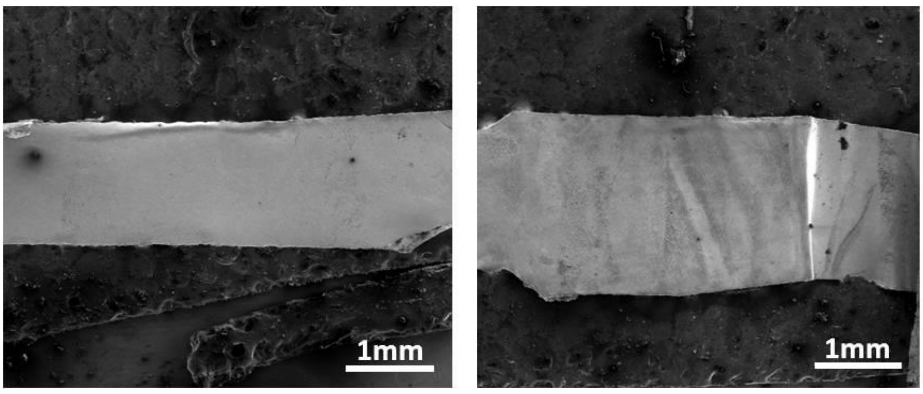

(a) (b)

Figure 3.10. (a) SEM of anode current collector Cu at the cut before charge. (b) SEM of anode current collector Cu at the cut after discharge and 100 cycles of stretching.

The similar SEM images are given for the cathode current collectors (e.g., Al foils) in Figures 3.11(a) and 3.11(b). There are no cracks after cyclic mechanical stretching, which contribute to the robust electrochemical and mechanical characterizations.

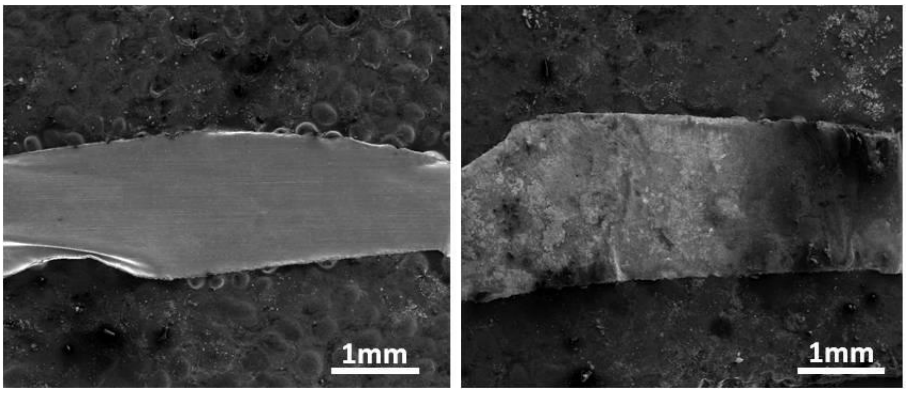

(a) (b)

Figure 3.11. (a) SEM of cathode current collector Al at the cut before charge. (b) SEM of cathode current collector Al at the cut after discharge and 100 cycles of stretching.

3.2.3 Connecting Kirigami Battery with Samsung Gear 2 Smart Watch

We demonstrated that the stretchable kirigami LIB is able to power a Samsung Gear 2 smart watch. The original LIB with energy capacity 300 mAh was removed from the Samsung Gear 2 and a kirigami LIB using cut-N-twist pattern was connected to the device. The same geometry as that in Fig. 13 was used. The mass loading for active

materials are 0.26 g for graphite, 0.65 g for LCO, which gives the energy capacity 80 mAh. At the compact state, the kirigami LIB is 51.3 mm in length, 27 mm in width, and 2.6 mm in thickness. The produced kirigami LIB was sewn between two elastic bands at its two ends and wrapped around the wrist, allowing the elastic bands to function as an elastic watch strap. By sewing the kirigami LIB to the elastic band at the two ends, the LIB can be stretched and contracted, driven by the elasticity of the band. Some snapshots are provided in Figure 3.12.

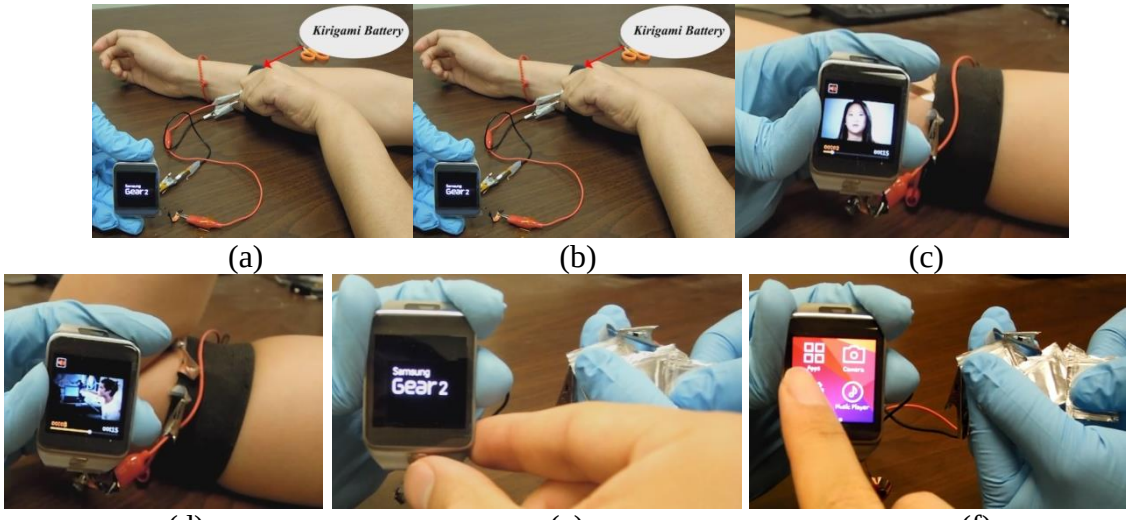

Figure 3.12. Powering a Samsung Gear 2 smart watch by a kirigami LIB using cut-N-twist pattern. The kirigami LIB sewn between two elastic bands was (a) at the wrist, (b) at the upper arm, (c) at the upper arm with elbow straightened, (d) at the upper arm with elbow bent. The kirigami LIB was removed from the elastic bands and stretched directly. (e) At the compact state and (f) at the stretched state.

Figure 3.12(a) shows that when the elastic band and the kirigami LIB were at their most compact states, the Samsung Gear 2 was just turned on. Then, while the elastic band was stretched from the wrist to the upper arm, the Samsung Gear 2 was working normally (Figure 3.12(b)). It is estimated from the circumferences of the wrist and upper arm, the kirigami LIB was subjected to a strain of 30%, lower than its full stretchability.

While the elbow bent (Figure 3.12(c)) and straightened (Figure 3.12(d)), the smart watch was able to maintain normal functionality, and even display a video. During bending and straightening of the elbow, the biceps introduced an additional 15% strain to the kirigami LIB. Finally, the kirigami LIB was removed from the elastic bands and stretched directly while powering the smart watch (Figures 3.12(e) and 3.12(f)).

To further evaluate the performance of the kirigami battery, standby and calling tests of the smart watch powered by the kirigami battery were carried out. For a fully charged kirigami battery with 80 mAh capacity that was connected with a Samsung Gear 2 smart watch, the standby time was measured to be 24.5 hours. When the smart watch was paired with a Samsung Galaxy S5 cell phone with a Bluetooth connection when they were separated by 30 cm, the smart watch was able to make calls through the Bluetooth connection. The calling time was measured to be 90 minutes. To simulate the standby and calling tests, quantitative discharge characterizations were also conducted by applying the corresponding constant discharge currents for standby (2.9 mA) and calling (48 mA) using an Arbin electrochemical workstation. The stopping voltage of the smart watch was measured to be 3.6 V. Details of the measurement of the discharge currents and stopping voltage are shown in Figure 3.13(a) for the simulated standby test, the calling time (when the voltage drops to the stopping voltage 3.6 V) is 25.8 hours, which is consistent with the direct test.

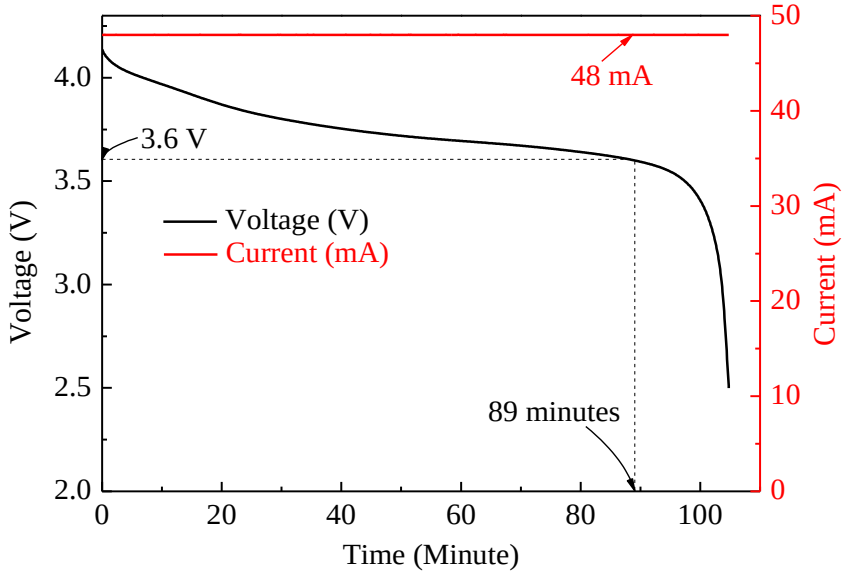

(a)

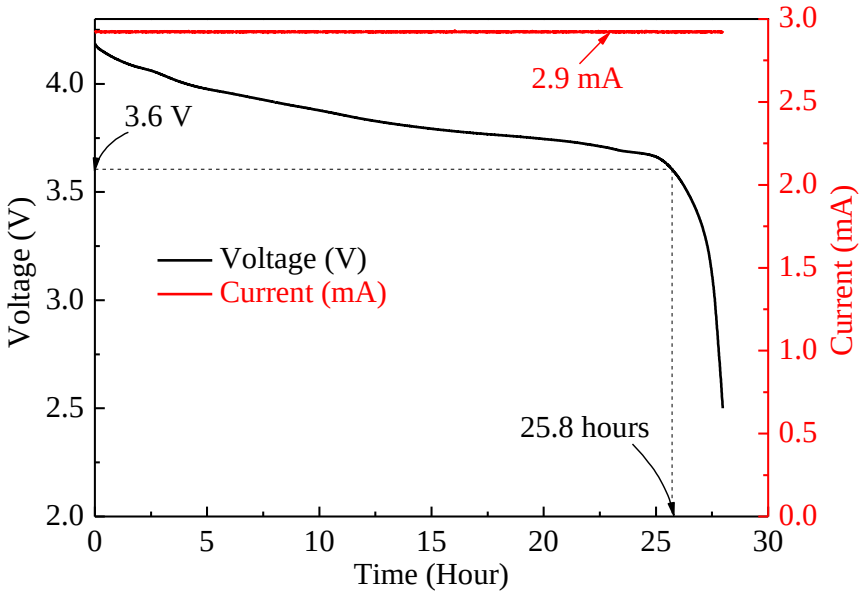

(b)

Figure 3.13. (a) Galvanostatic discharge to simulate the standby test with discharge current 2.9 mA. (b) Galvanostatic discharge to simulate the calling test with discharge current 48 mA. The stopping voltage is 3.6 V.

For the simulated calling test (Figure 3.13(b)), the calling time is 90 minutes, which perfectly matches the direct test. It should be noticed that the discharge currents for standby and calling are relatively low C-rate for the present kirigami battery with 80 mAh capacity, specifically discharge current for standby 2.9 mA ≈ C/30 and that for calling 48 mA ≈ C/2. Given the stable rate performance as shown in Figure 3.5 (though for a kirigami battery with different capacity), a stable cyclic charge/discharge performance can be expected. These experiments demonstrate the promises of using a kirigami LIB to replace present rigid and bulky batteries and to power a commercial smart watch, which has been a bottle-neck in developing compact wearable devices. It is worth mentioning that if the kirigami LIB is scaled up to cover the entire area of the elastic band (25 cm in length, 3 cm in width) with a battery thickness of 0.3 cm, the energy capacity is about 700 mAh, which significantly exceeds the current LIB used in most smart watches, and the energy density is about 160 Wh/Kg, which is comparable to the current LIB used in smart watches or smart phones. By using the space of watch strap instead of using the limited space of watch body, the kirigami battery may disruptively impact the field of wearable electronics by offering extra physical and functional design space. Furthermore, to test the compatibility of the Kirigami battery integrated with real watchband, a Cut-N-Twist battery was embedded in a watchband made of Sorta-Clear 40 (Smooth-On, Inc.).

3.2.4 Thermal test of Kirigami battery and Samsung Gear 2 battery

The Kirigami battery is thin film based. It is has much higher surface-to-volume ratio than bulky battery, which is beneficial for heat radiation. The thermal test of Kirigami battery and Samsung Gear 2 bulky battery were conducted. In the test both

batteries discharged at 48mA for one hour. Obvious temperature rise was observed for the Gear 2 bulky battery, while the Kirigami battery was consistent with the ambient temperature during the discharge period.

3.3 Discussion

The demonstration of stretchable kirigami LIBs in a Samsung smart watch only represents one application of this type of stretchable energy sources that fully utilize the mainstream manufacturing capability. Other applications may include smart bracelets and smart headbands among many others. It is expected that the kirigami LIBs are able to resolve one of the bottlenecks in the development of wearable devices by providing a scalable solution for a stretchable energy source to profoundly change the form factor. The methodology involved in kirigami-based approach, i.e., competing mechanisms between ‘crack growth’ and ‘plastic rolling’ also provide a much broader spectrum of employing the concept of kirigami to other fields, such as in microelectromechanical systems (MEMS) where robust interconnects can be placed at the cut/fold locations and the functional devices are fabricated on the rigid faces, which leads to stretchable devices using standardized procedures. These areas appear promising for further research.

CHAPTER 4

MICROSCALE SILICON ORIGAMI

4.1 Background

Chapter 2 and chapter 3 introduce two macro level applications of origami and kirigami, namely stretchable lithium ion batteries. In micro regimes, one particularly interesting application of origami is to form complicated 3D architectures from 2D sheets, which paves a way to fabricate complex 3D patterns in micro level that are otherwise impossible. The applications of 3D architectures span from many disciplines. There are 3D MEMS, artificial biological systems (*56, 57*), metrology (*58*), and energy storages (*59*). Some strategies have been developed to fabricate microscale 3D structures, such as self-assembly (*60*) and residual stress-induced bending (*61*) that are limited to choices of materials. A recent compressive buckling (*62*) approach is capable to fabricate 3D ribbon-liked structures. The intrinsic geometrical feature of origami, i.e., high aspect ratio between the out-of-plane dimension of the origami (vertical distance from the 'mountain' vertex to the 'valley' vertex) and thickness of 2D sheets, which is typical much greater than 100, makes the widely-used fabrication approaches, such as photolithography and 3D printing., incapable for microscale origami.

Here we demonstrate a new strategy to fabricate microscale origami using Si NMs as the materials that are supported by elevated PDMS walls on top of a PDMS substrate. Thus the Si NMs are suspended. Upon relaxation of the pre-stretch applied on the PDMS substrates, the suspended Si NMs buckle with the pre-patterned wall as the support and constraints to form designated microscale Si origami. The final microscale origami patterns are controlled by the patterning of the elevated wall.

4.2 Introduction of micro Transfer Printing

Micro-Transfer-Printing (μTP) is one of the essential processes to meet the goal of making silicon origamis. The (μTP) process, which was invented by Professor John Rogers at the University of Illinois, Urbana-Champaign (*63, 64*), utilizes engineered elastomer stamps to selectively pick-up and print large arrays of microscale devices onto non-native substrates. In its simplest process, (μTP) is analogous to using a rubber stamp to transfer liquid-based inks from an ink-pad onto paper. However, in (μTP) the 'inks' are actually a diversity of material classes with a wide range of geometries and confi gurations having functional integration into the precise architectures required by devices and the 'paper' can be many things, including plastics and other semiconductors.

In transfer printing-based fabrication schemes, almost any class of material can be developed in the form of an ink from complex molecular scale materials nanotubes and grapheme (*65-68*), photoresists (*69*), (self-assembled monolayers (SAMs) (*70-72*), DNA (*73-75*) and functional polymers, (*76-78*) etc.), to high performance hard materials (metals (*79-82*), oxide thin films (*83, 84*), single-crystalline inorganic semiconductors (*63, 85-88*), complementary metal oxide semiconductor (CMOS) circuits (*89-91*), etc.), to fully integrated device structures (solar cells (*92, 93*), thin film transistors (TFTs) (*63, 64, 91, 94, 95*), sensing arrays(*33, 96*), LEDs, (*97, 98*) etc.).

Transfer printing process can be classified into three distinct categories as shown in Figure 4.1: additive transfer, subtractive transfer, and deterministic assembly. Additive transfer, shown in Figure 4.1(a) is an effective method for processing many types of organic and inorganic materials (*99-108*). Transfer occurs between a receiving substrate

and an entire ink layer, or selected parts of it, which have been deposited on the surface of a stamp.

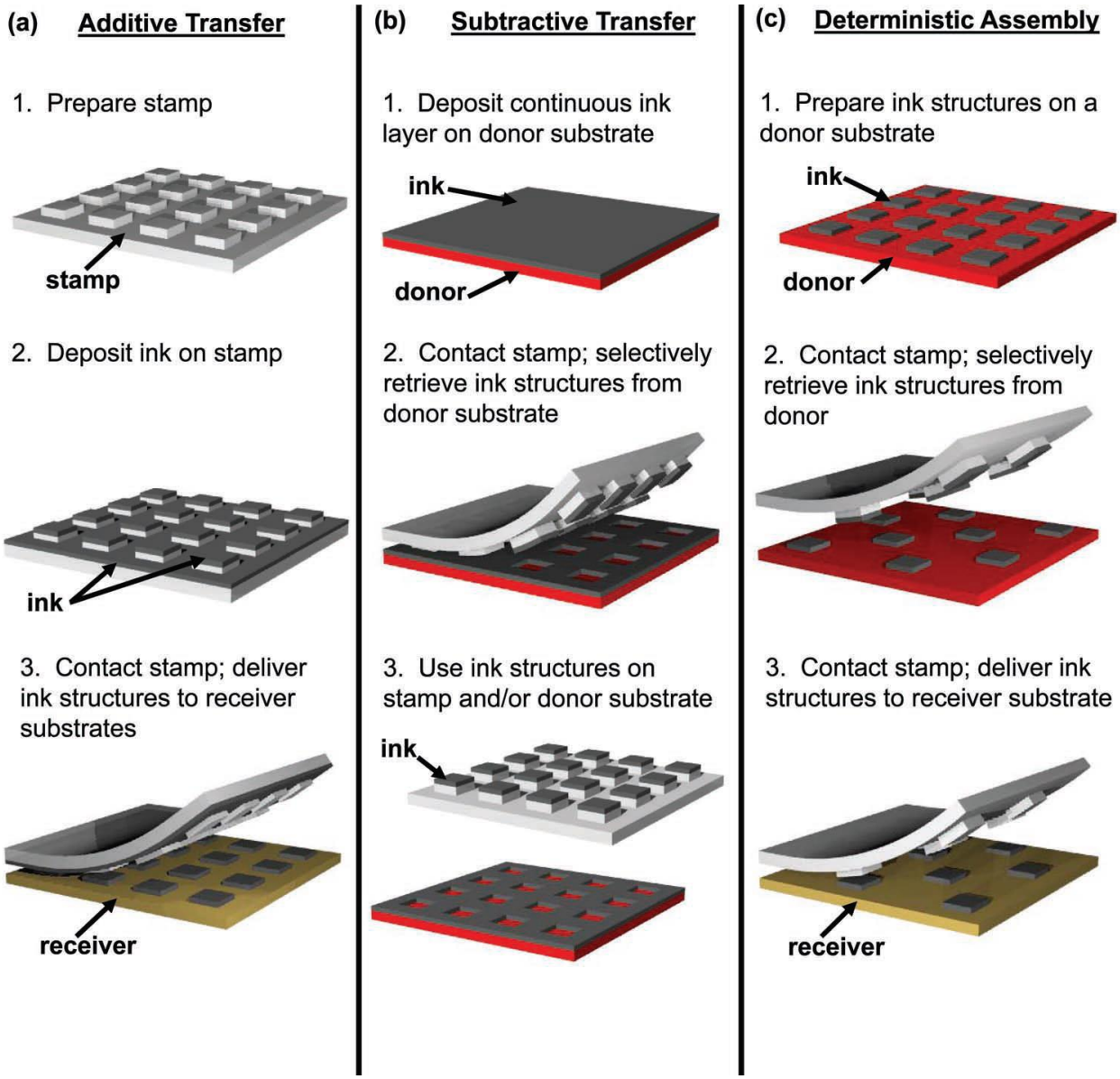

Figure 4.1. Schematic illustrations of three basic modes for transfer printing. (a) Additive transfer. (b) Subtractive transfer. (c) Deterministic assembly.

Figure 4.1(b) shows the second method, named subtractive transfer. It utilizes a stamp to selectively pick up regions of a blanket film and use ink structures on stamp and/or donor substrate. Figure 4.1(c) shows deterministic assembly which is a combination of additive transfer and subtractive tranfer. Ink structure is first prepared on a donor substrate, followed by selectively being picked up by a stamp. Then the stamp with ink structure is contacted with receivers and delivers ink onto it.

At the heart of these three method is how to selectively tune the adhesion between the elastomer stamp and the donor or receiver by varying the speed of the print-head (*64*).

$$G_{stamp/ink} = G_0[1+\varphi(v)] \quad (1)$$

Where $G_{stamp/ink}$ is the adhesion energy hysteresis taken as the separation energy, or the energy release rate between stamp and ink structures. v is the separation speed between stamp and ink structures. φ is an increasing function of v and φ(v)=0 when v=0. G_0 is the initial energy release rate when v=0.

Separation energy $G_{stamp/ink}$ depends strongly on the speed of separation speed v owing to the viscous behavior of stamps. Conversely, the separation energy between ink structure and donor or receiver $G_{ink/substrate}$ is typically independent of rate. As the speed of separation speed v increase, $G_{stamp/ink}$ increases relative to $G_{ink/substrate}$ until the stamp-ink interface becomes strong enough to break the ink-substrate interface.

When the stamp is moved quickly away from a bonded interface, the adhesion is large enough to ‘pick’ the ink structures away from their native substrates, and conversely, when the stamp is moved slowly away from a bonded interface the adhesion is low enough to ‘let go’ or ‘print’ the element onto a foreign surface.

In this dissertation, we utilized the second transfer method, subtractive transfer to make silicone origamis. To futher increase bonding between stamp (PDMS) and ink structure (Si NMs), PDMS is pretreated under UV/ozone (UVO) light to form a thin SiO_x layer, such that strong –O-Si-O- bonding occurs with the native oxide of the Si NMs (*109*)

The chemistry upon PDMS exposure to UV radiation at 185 and 254 nm in air atmosphere has been proposed as below (*110*).

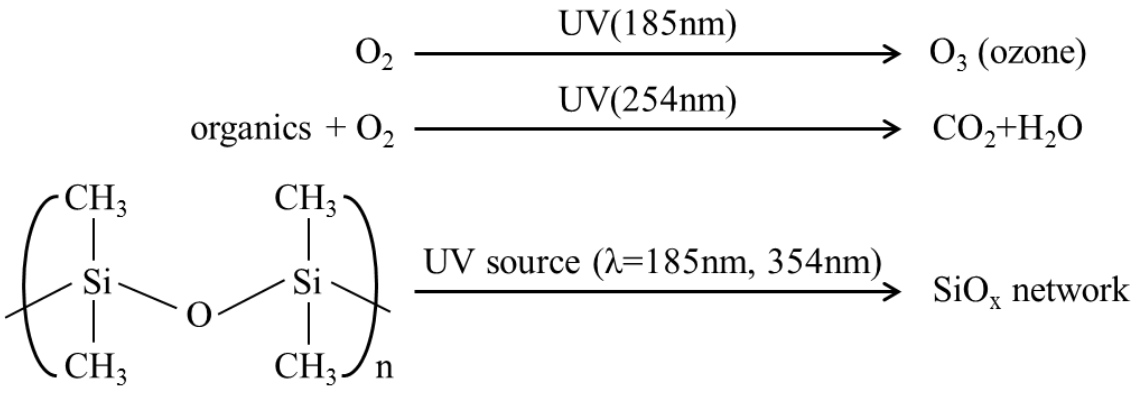

4.3 Experiment and Results

4.3.1 Fabrication of Silicon Origami

The methodology is illustrated in Figure 4.2. Silicon mold was made by a single side bare silicon wafer (500um in thickness), which was patterned with origami patterns by deep Silicon Etching (STS ICP Advanced Silicon Etch, 75minutes, 200um in depth) following photolithography (EVG 620, 400mJ/cm2,) using photoresist (AZ 4330), The photoresist was then removed with acetone and a thin layer of release agent 1H,1H,2H,2H-perfluorooctyltrichlorosilane was vapor coated on top of the silicon. PDMS (Sylgard 184, Dow Corning) solution (mixed base and curing agent with 10:1 ratio by weight) was then poured into the mold and cure at 80^{o}C for 3 hours. PDMS was

peeled and cut into desire shape ca. 20mm wide, 15mm long, followed by biaxial or uniaxial pre-stretch (from L to $L + \Delta L_1$ and $L + \Delta L_2$ along the perpendicular directions), which can be achieved by mechanical means or heating. The characteristic sizes of the elevated walls are on the order of $10-120\mu m$. The pre-stretched PDMS is subjected to ultraviolet/ozone treatment in order to form activated hydroxyl groups for bonding as mentioned before. Because the PDMS walls are elevated, they thus provide selective bonding sites. Then a Si NM is prepared by patterning The top thin silicon layer (300nm in thickness) of a Si-on-insulator (SOI) wafer to form membranes ca. 7mm wide, 8 mm long with hole-arrays inside (8um in diameter for each hole) by reactive ion etching (Oxford Plasmalab80 RIE Fluorine; SF6, 100 W, 1 minute) following photolithography (EVG 620, 300mJ/cm2,) using photoresist (AZ 4330). Removing the photoresist with acetone and then etching the sacrifice SiO2 layer with hydrofluoric acid (49%, 50 minutes) releases the membranes from the underlying Si substrate. Then Si NMs is derived from the SOI wafer and brought to contact with the patterned PDMS. Specifically, the elevated PDMS walls provide supports to Si NM and thus Si NM is suspended. Because of the surface treatment, condensation reactions occur at room temperature between the elevated PDMS walls and the native oxide surfaces of Si NMs (*111-113*). Si NMs then can be exfoliated from the SOI wafer and adhere to the elevated PDMS walls. Once the pre-stretch exceeds a certain critical level, relaxation of the pre-stretch buckles suspended Si NMs and forms origami patterns. The buckling is the result of releasing the membrane energy through the out-of-plane deformation via mainly bending and sometime twisting. The resulted origami patterns are defined by two factors: (1) the shape of the pre-patterned, elevated walls, and (2) the nature of pre-stretch (i.e., biaxial with

different pre-stretches in two directions vs. equi-biaxial pre-stretch). The first factor determines the type of the origami and later fine tunes the patterns.

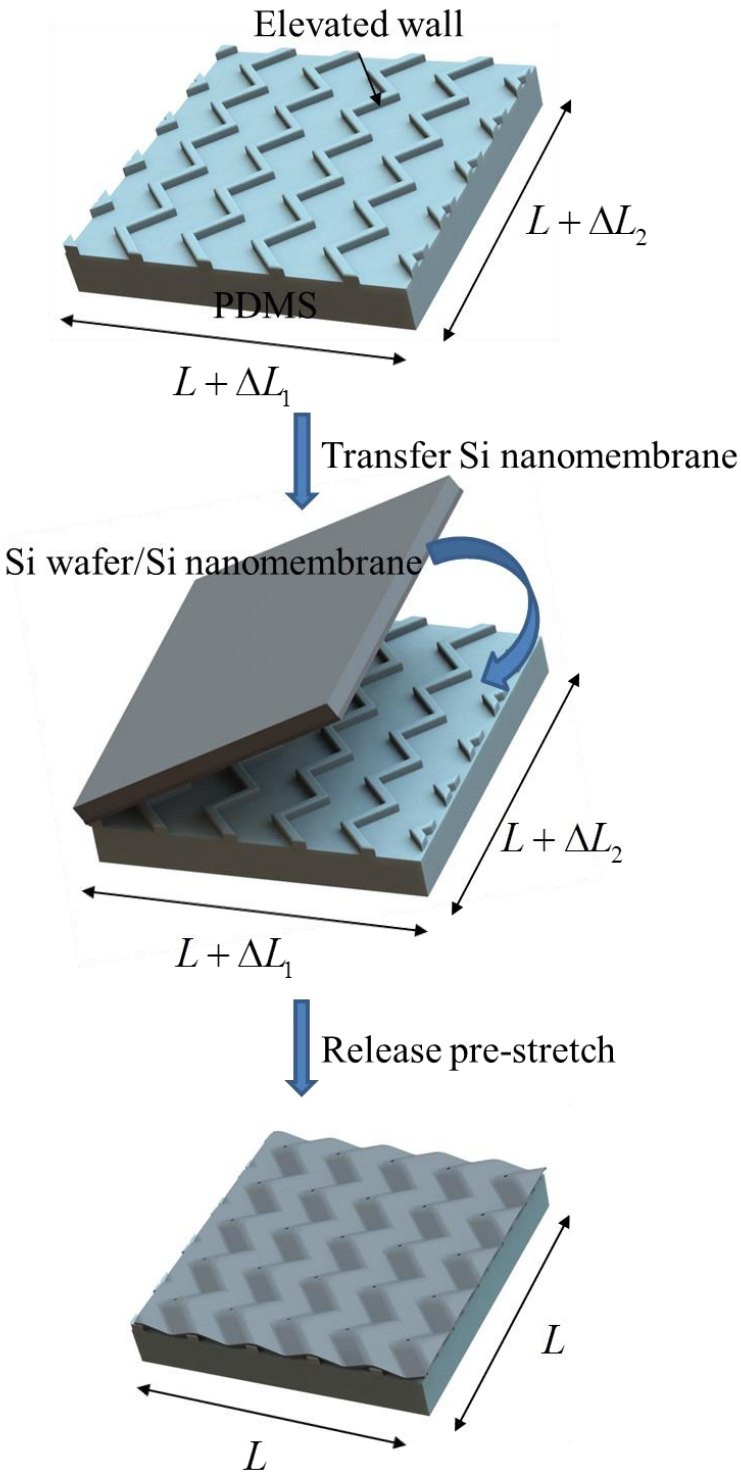

Figure 4.2. Schematic illustration of using elevated PDMS walls to suspend Si NM and releasing the pre-stretch to generate designated microscale origami patterns. Here the elevated PDMS walls have been pre-patterned for the Miura-ori pattern.

4.3.2 Studies of Silicon with Different Patterns

As a specific example using the pre-patterned walls with shapes illustrated in Figure 4.2, a Miura-ori pattern (*49*) can be obtained. Figure 4.3 shows a photography of a Si NM Miura-ori pattern generated using this approach, where the thickness of the Si NM is 300 nm and the equi-biaxial pre-strain is 3.6% introduced by heating the PDMS from room temperature to 120^{o}C.

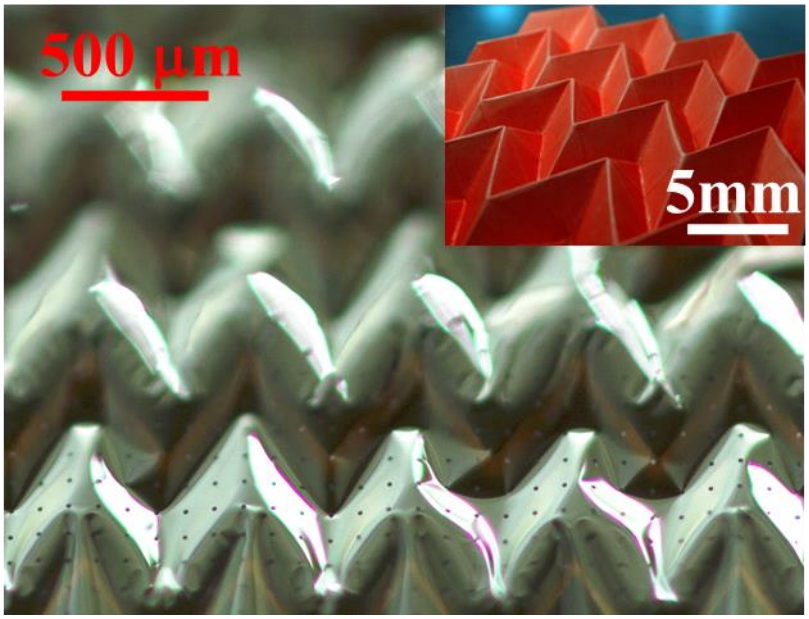

Figure 4.3. A photography of a Si NM Miura-ori pattern. The inset shows a paper-based Miura-ori pattern for comparison.

The detailed geometry of the pre-patterned PDMS wall is given in Figures A1(a) and A1(b).

It is apparent that in a 12.5mm × 10.9 mm area this Si NM Miura-ori pattern replicates the paper-based Miura-ori, given by the inset of Figure 4.3. The observable

difference is that the sharp ‘mountain’ creases in paper-based Miura-ori are replaced by the flat PDMS walls in the Si NM Miura-ori, because the downwards out-of-plane buckling occurs and the elevated PDMS walls actually form as ‘mountain’ supports for the Si NMs. The ‘valley’ creases are not as sharp as paper-based pattern because of the buckling. It is emphasized here that using this origami inspired methodology, a planar structure is transferred to a 3D architecture across an entirely continuum film, rather than discretized ribbons (*62*). Figures 4.4(a) and 4.4(b) show the SEMs of the Si NM Miura-ori patterns, where the well-defined periodicity is clearly observed.

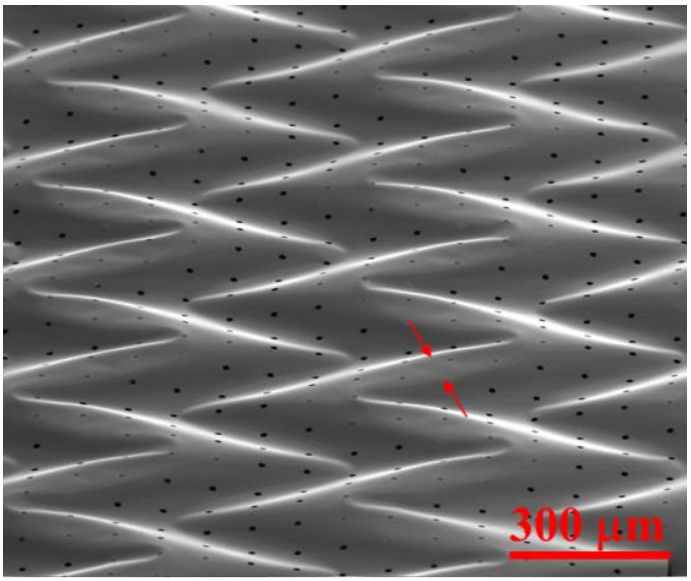

(a)

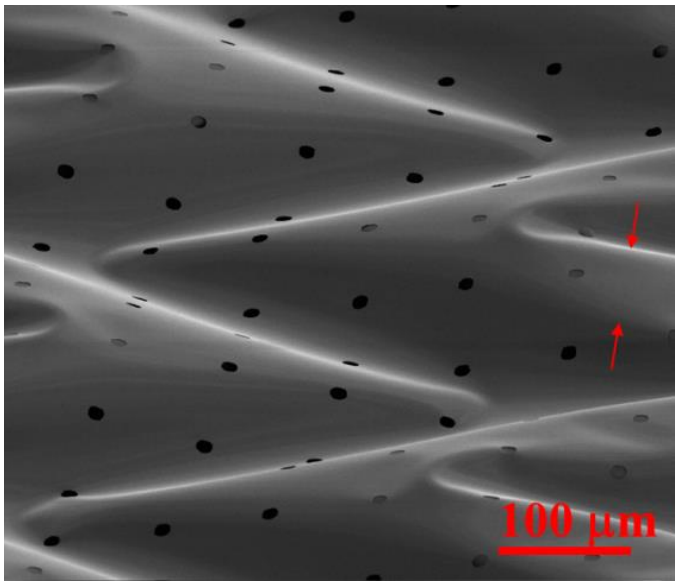

(b)

Figure 4.4. (a) SEM image shows periodic Si NM Miura-ori pattern in an overall 1 mm × 1 mm area. (b) A SEM image shows the details of the Si NM Miura-ori pattern.

The measured width of the PDMS wall is about 117.02 μm (shown within red arrows in Figures 4.4(a) and 4.4(b), which is larger than the pre-designed 111.8 μm (Figure A1(b)) due to partial delamination at the wall. Figure 4.5 provides a cross-sectional view near the elevated PDMS walls using an integrated focused ion beam (FIB) and an SEM system, where the partial delamination is observed at the vertices of the elevated PDMS walls. The partial delamination may release the stress concentration at the wall.

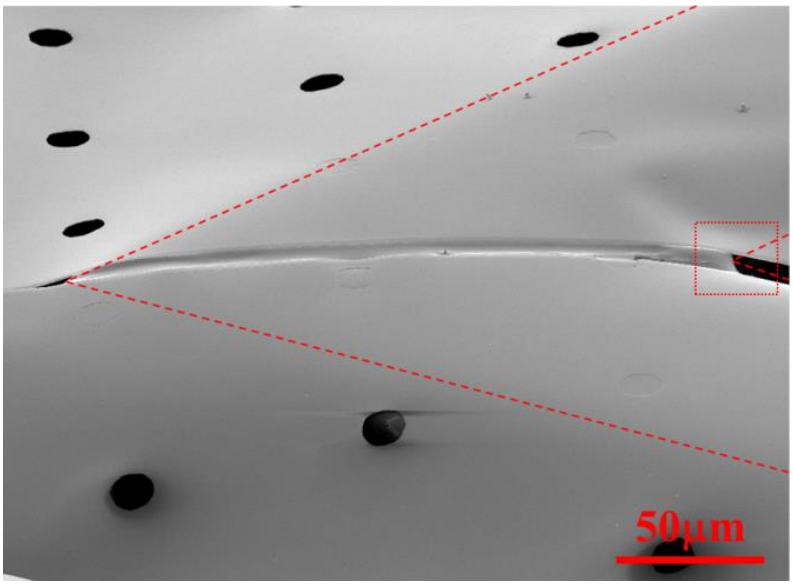

(a)

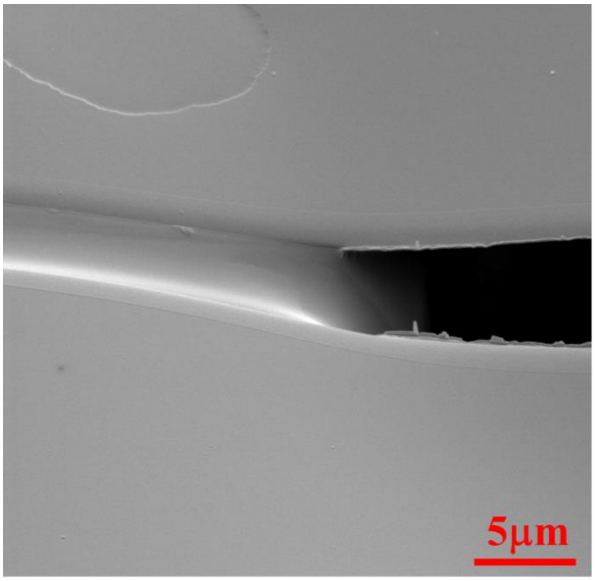

(b)

Figure 4.5. SEM images near the elevated PDMS walls. Triangular dash lines in (a) indicate creases and in ractangular dash lines is the delamination region and has been zoomed in in (b).

Figures 4.6(a) and 4.6(b) provide the optical profilometer images of the Si NM Miura-ori pattern. It is observed that the Si NM has apparent deformation at the vertices

of the elevated wall (marked by the red triangle) in Figure 4.6(a), which suggests a localized and possibly large strain presents.

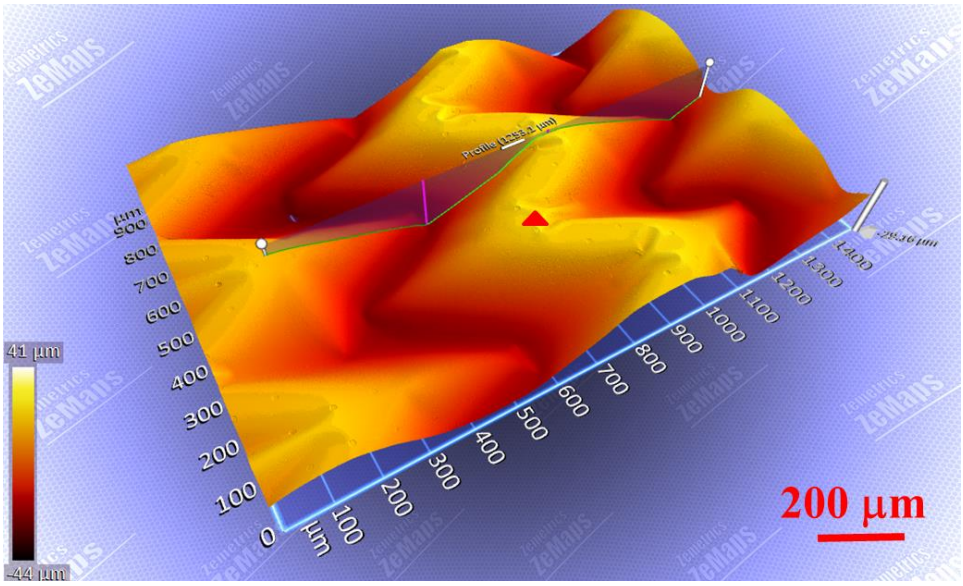

(a)

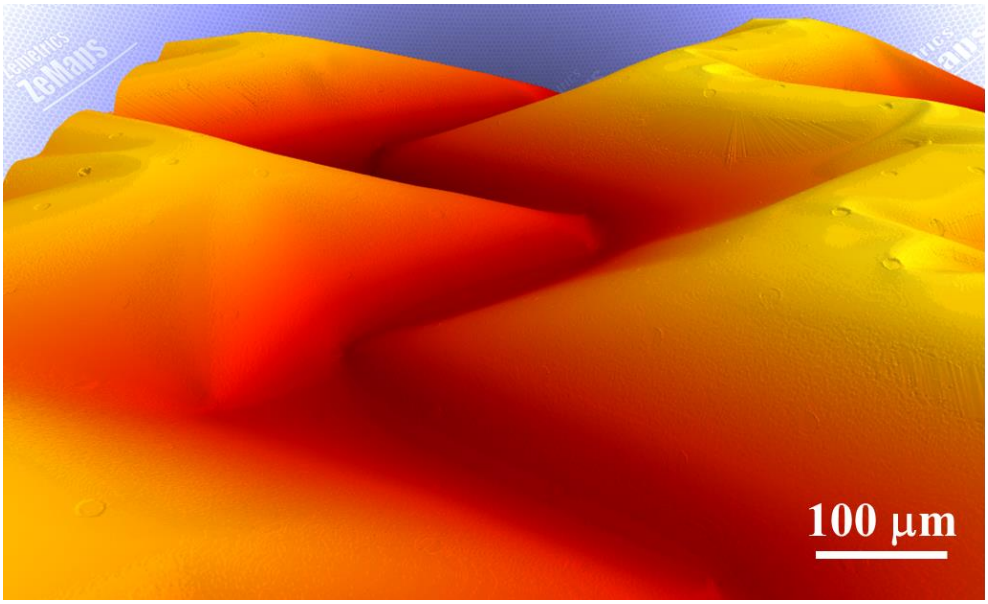

(b)

Figure 4.6. (a) A optical profilometer image shows the Si NM Miura-ori pattern. The line cut measurement was performed. (b) A optical profilometer image shows the details of the Si NM Miura-ori pattern.

Figures 4.7(a), 4.7(b) and 4.7(c) show the line-cut with comparison between the experiments, FEA results, and analytical expression of rigorous Miura-pattern. Use *n* to denote the number of creases at one vertex and *n*=4 for Miura-ori. For ideally rigid origami (e.g., Miura-ori) where all facets are rigid and only the creases deform during folding, it is known that there are *n*-3 degrees of freedoms (*51, 52*); thus Miura-ori has only one degree of freedom. The closed loop solution can be obtained and detailed. It is observed that the generated Si NM origami agrees reasonably well with both the analytical and FEA results. The major discrepancies occur at the 'mountain' vertices since the analytical solution and FEA results are based on zero size of creases while the experiments have finite size of the elevated PDMS walls.

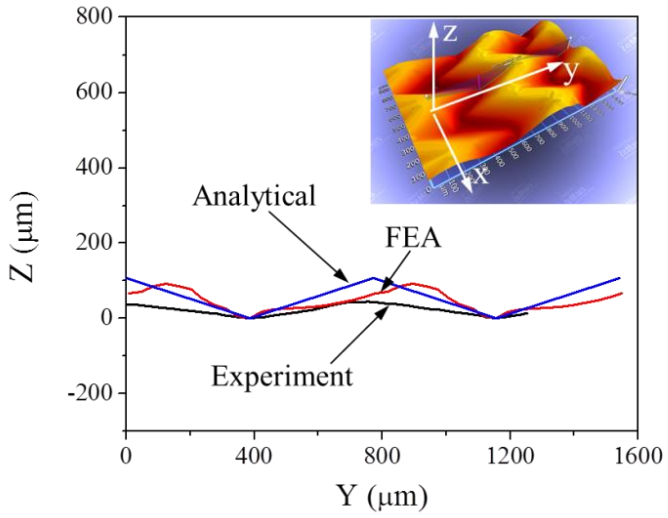

(a)

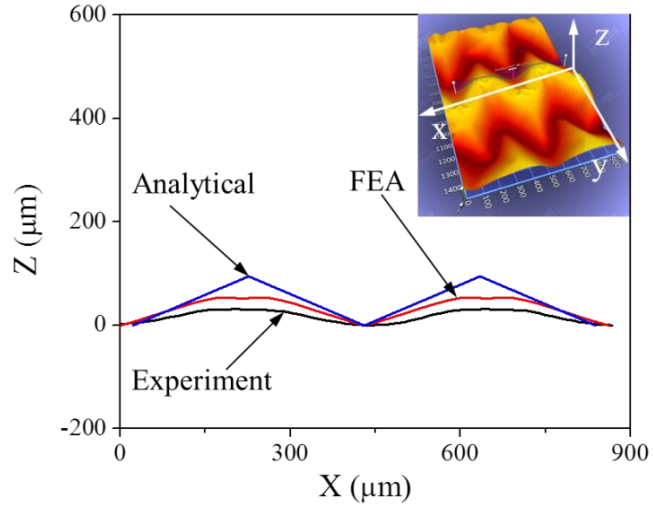

(b)

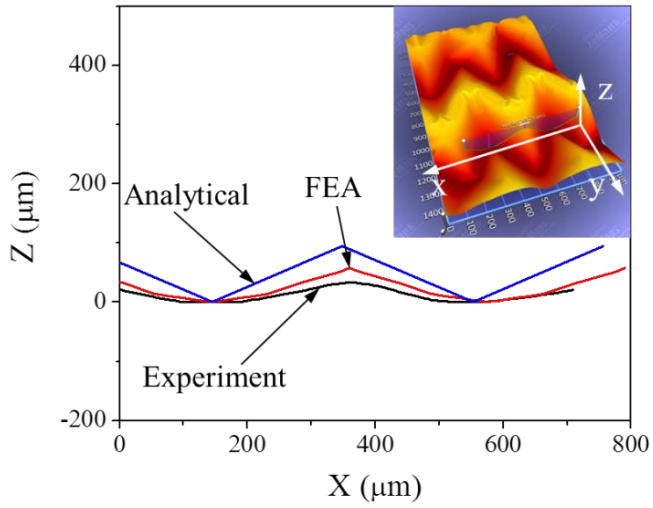

(c)

Figure 4.7. Line cut comparisons between the experiment, FEA, and analytical solution. The inset shows an image of optical profilometer, in which the line cut profile was measured in experiment. The measured directions are: **(a)** 'mountain'-'valley'-'mountain' cut along y-direction, **(b)** along the mid-point of 'mountain' creases, and **(c)** 'mountain'-'valley'-'mountain' cut along x-direction.

Wide range and more complicated Si NM origami patterns can be realized, with the inspiration from the paper-based origami. The logic is to vary the shape of the elevated PDMS walls. As there are significant variations of paper-based origami, the first extension from Figure 4.3 is an origami pattern with three (3) degrees of freedoms. Figure 4.8 shows a photography of a Si NM origami with waterbomb pattern, or the nickname ‘magic ball’ pattern, through the relaxation of 3.6% pre-strain via thermal expansion of the PDMS.

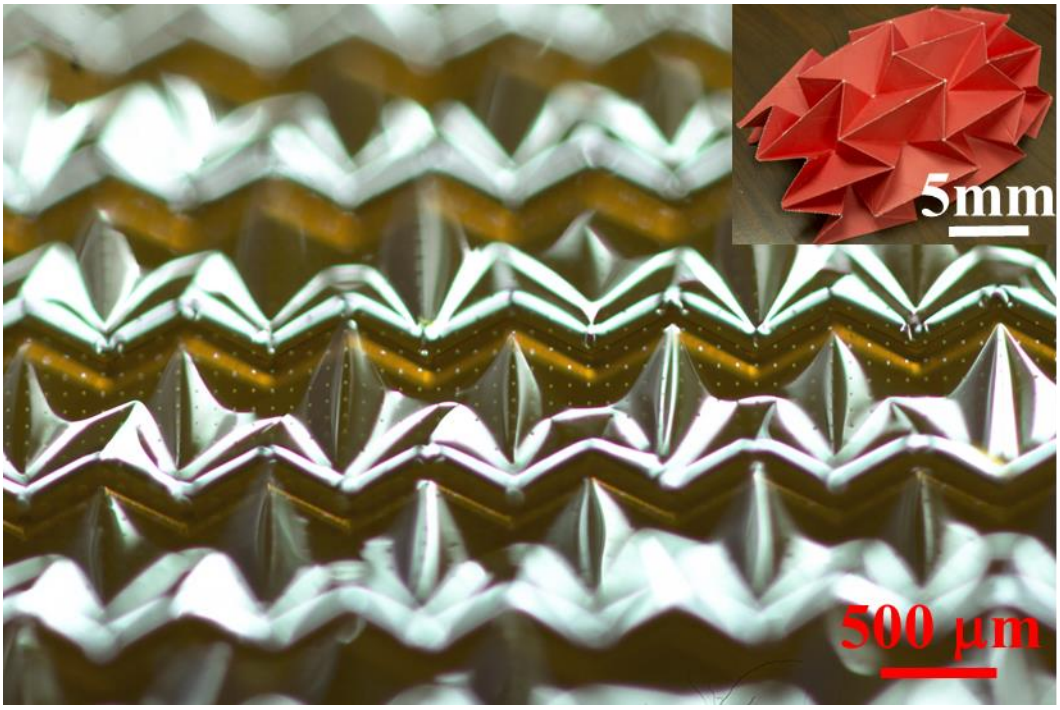

Figure 4.8. A photography of a Si NM ‘magic ball’ pattern. The inset shows a paper-based Miura-ori pattern for comparison.

The detailed shape and geometry of the elevated PDMS walls to form this pattern are given in the Figures A2(a) and A2(b).

Great similarity is observed when compared with the paper-based ‘magic ball’ pattern (inset of Figure 4.8). However, a discrepancy is also noticed and in fact related to

the methodology of generating microscale origami using elevated PDMS walls. For ideal ‘magic ball’ pattern (as detailed in the supporting information), the ‘mountain’ creases always form a curved geometry and cannot stay flat unless at the completed collapsed state, which is different from the Si NM origami (Figure 4.8) where the ‘mountain’ creases (i.e., elevated PDMS walls) are on the flat state. The reason is that Si NM is not ideal rigid and facets are allowed to deform.

Figures 4.9(a) and 4.9(b) further show the SEM and optical profilometer of Si NM ‘magic ball’ patterns. This example suggests that the methodology is able to mimic paper-based origami with complicated shapes and further modify them by utilizing the deformability of Si NMs.

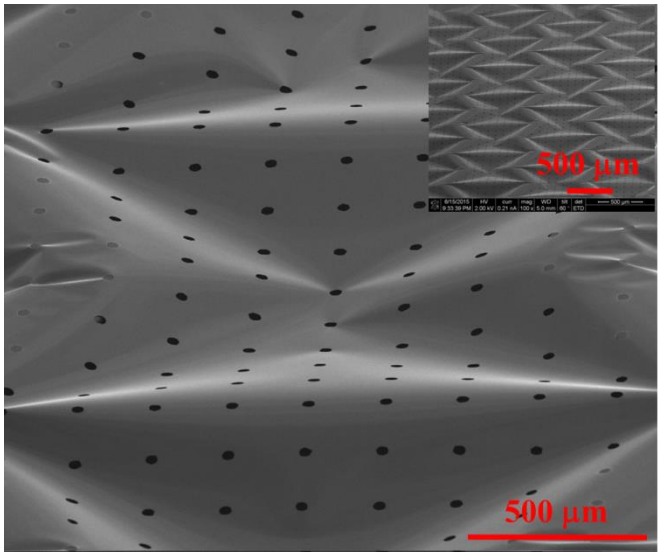

(a)

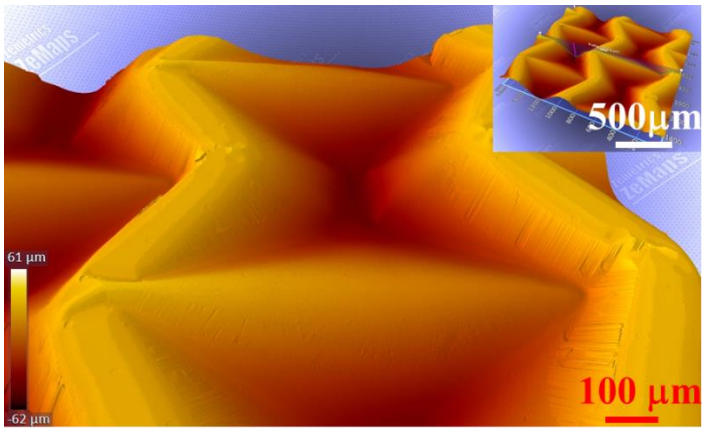

(b)

Figure 4.9. A SEM image shows Si NM 'magic ball' pattern in an overall 13.9 mm × 15.2 mm area. (d) A optical profilometer image shows the Si NM 'magic ball' pattern.

Figures 4.10(a) and 4.10(b) provide more Si NM origami patterns that cannot be rigidly folded using paper but can be achieved using the present methodology.

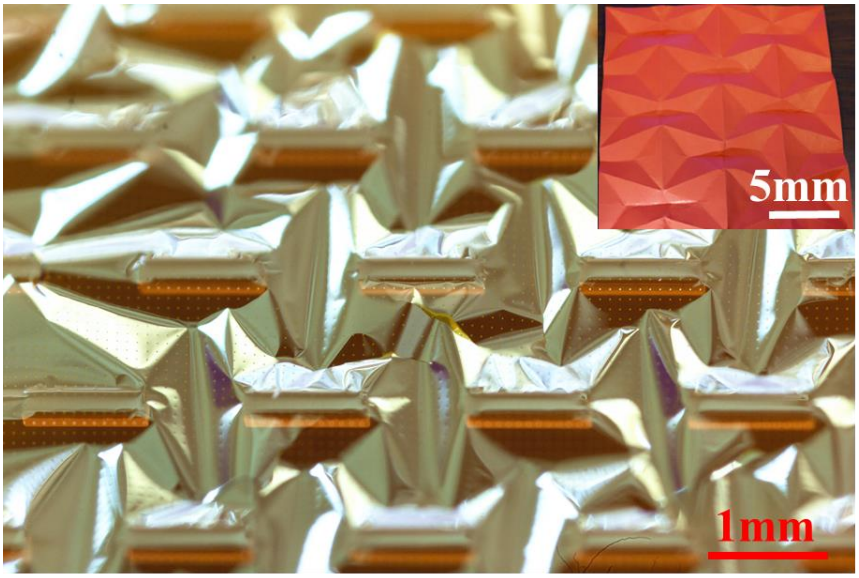

(a)

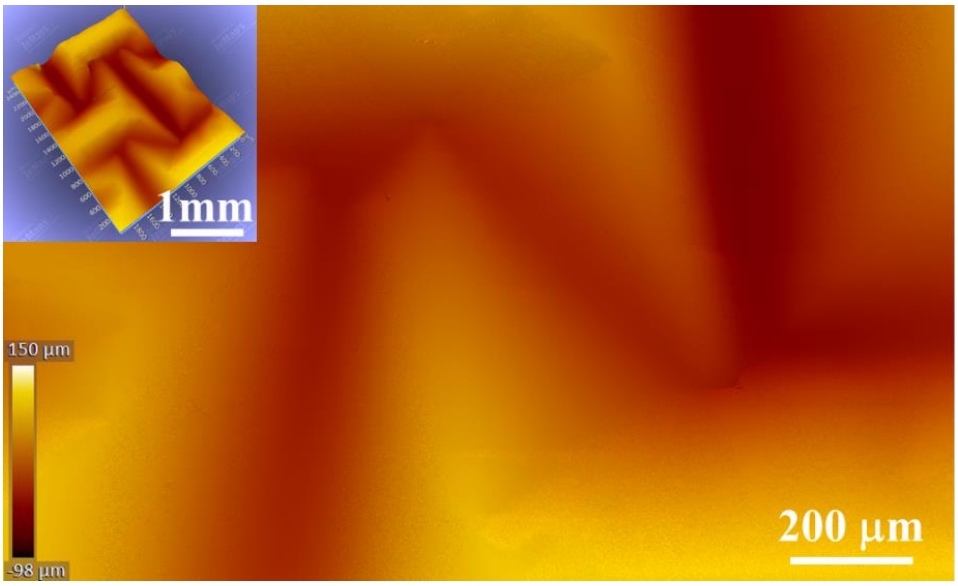

(b)

Figure 4.10. (a) A photography of a Si NM non-rigidly foldable pattern. (b) A optical profilometer image shows the Si NM non-rigidly foldable pattern.

Figure 4.10(a) presents the photography of a non-rigidly foldable pattern using staggered PDMS walls given in Figures A3(a) and A3(b).

To be rigid foldable, at all vertices, the difference between numbers of 'mountain' and 'valley' creases must be 2 or 0. As seen from Figure 4.10(a), this condition is not satisfied at neither vertices; thus it is not rigid foldable. To generate this pattern, Si NMs have to be geometrically compatible at the facets through bending, which can be clearly observed in Figure 4.10(b) (optical profilometer). Very sharp creases are observed. Related to this pattern that it is not rigid foldable at all vertices, some patterns are rigid foldable at the unit cell level but are not at the assembled level, such as the star pattern shown in Figures 4.11(a) – 4.11(c).

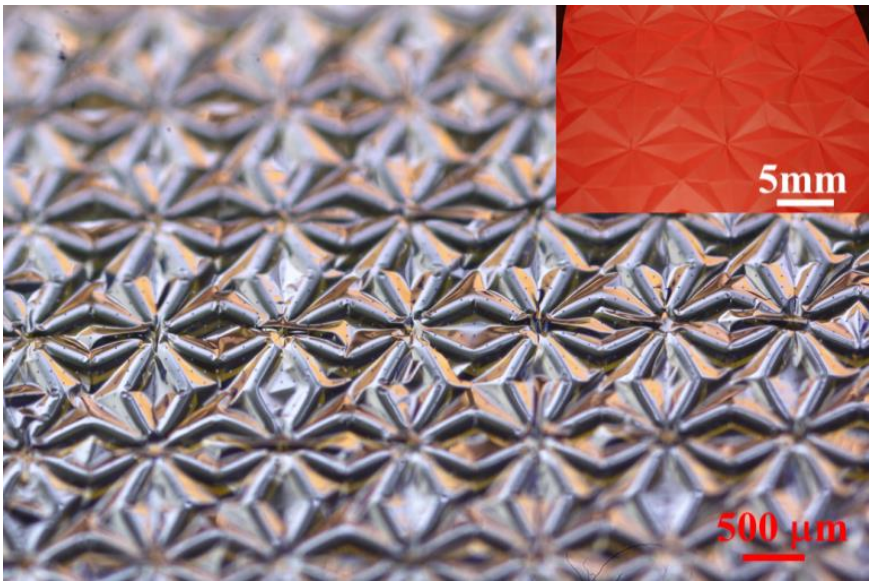

(a)

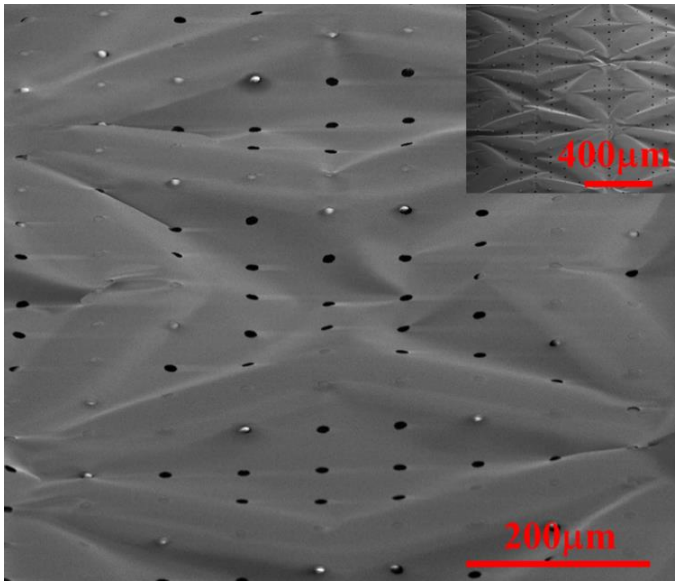

(b)

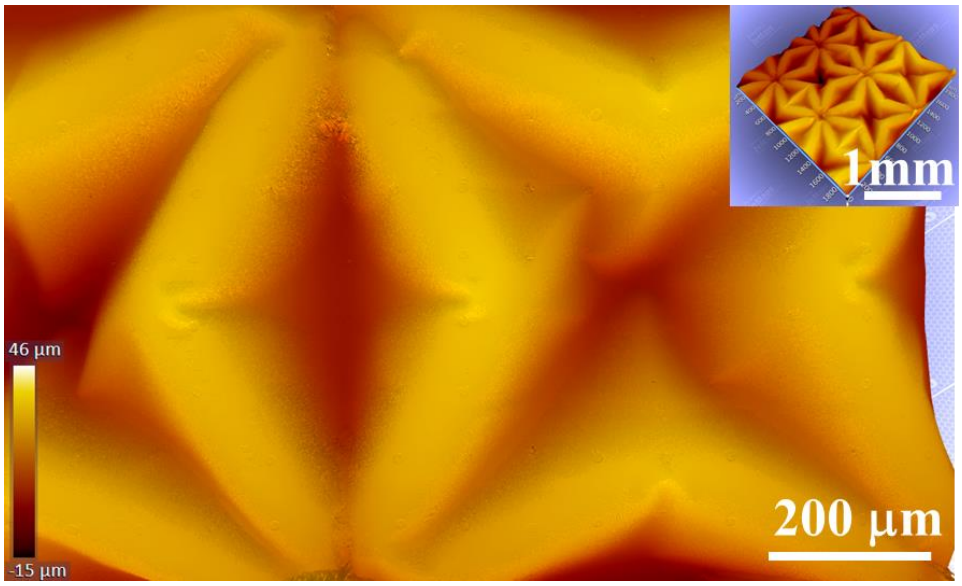

(c)

Figure 4.11. (a) A photography of a Si NM star pattern. (b) A SEM image shows Si NM star foldable pattern. (c) A optical profilometer image shows the Si NM star pattern.

The shape and geometry of the PDMS walls for star patern are given in Figures A4(a) and A4(b).

In this pattern, the unit cell is a star, which is rigid foldable. However, when two stars are assembled, their boundaries are not rigid foldable. Composite and non-periodic patterns can be generated by combing multiply patterns, such as the mimicked US Flag shown in Figures 4.12(a) - 4.12(c) consisting of stars and stripes.

(a)

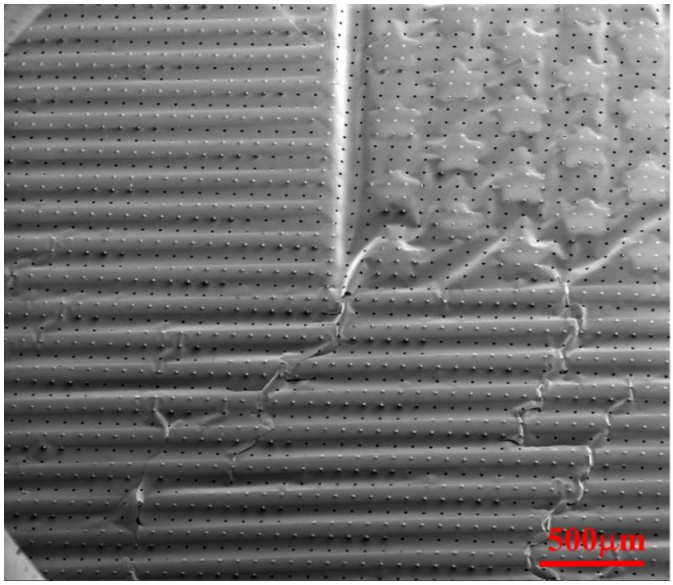

(b)

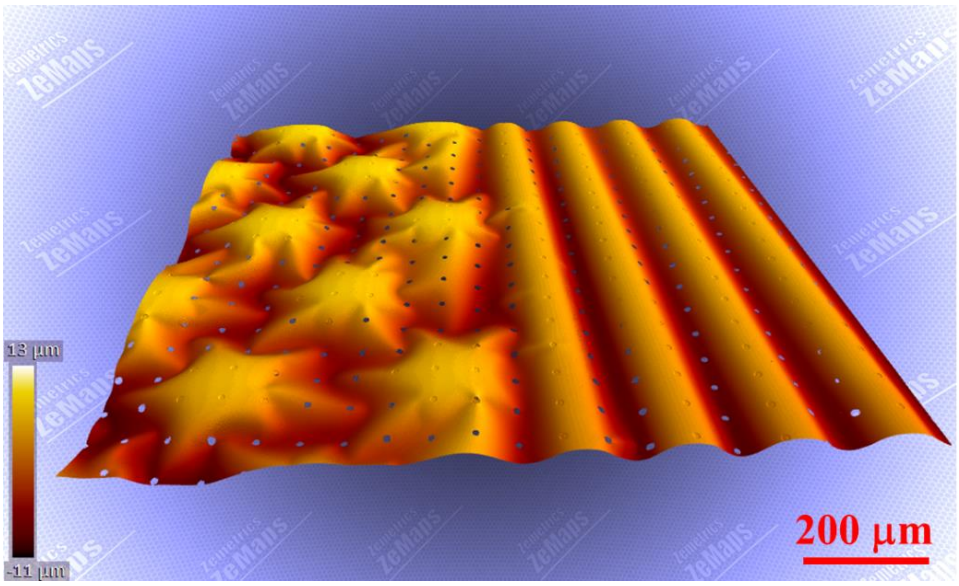

(c)

Figure 4.12. (a) A photography of a Si NM US Flag pattern. (b) A SEM image shows Si NM US Flag pattern. (c) A optical profilometer image shows the Si NM US Flag pattern.

The shape and geometry of the PDMS walls for US flag patern are given in Figures A5(a) and A5(b).

4.4 Discussion

Control over the geometrical configuration of semiconductor nanostructures is important for nearly all applications. In this chapter, a mechanical strategy for creating 3D origami silicons that would be difficult to generate in other ways is reported. This approach involves transfer printing Si NMs on pre-stretched, elevated PDMS walls, following by releaing the pre-strain to achieve 3D origamis. One big challenge of this approach is that pattern of PDMS wall needs to be carefully designed to minimize the strain at vertex where highest strain tends to occur.

CHAPTER 5

CONCLUSIONS AND OUTLOOK

5.1 Summary

In summary, history, classification and theory of origami and kirigami are studied in the first chapter of this dissertation. Applications of origami and kirigami are then demonstrated in followed chapters.

In chapter 2, an approach to enable origami LIBs with the attributes of extreme mechanical deformability was reported, including significant system-level linear and areal deformability large twistability and bendability, and up to 74% areal coverage. Furthermore, commercially standard packaging technologies were used in the origami LIBs, which when combined with other deformable electronic devices, may lead to direct practical applications.

In chapter 3, the LIBs were produced by the standard slurry coating (using graphite as an anode and $LiCoO_2$ as a cathode) and packaging procedure, followed by a designated folding and cutting procedure to achieve a particular kirigami pattern. Over 150% stretchability has been achieved and the produced kirigami LIBs have demonstrated the ability to power a Samsung Gear 2 smart watch, which shows the potential applications of this approach. The kirigami-based methodology can be readily expanded to other applications to develop highly stretchable devices and thus deeply and broadly impact the field of stretchable and wearable electronics.

In chapter 4, 3D silicon origami structures was created by tranfer printing Si NMs onto pre-stretched PDMS wall followed by releasing the prestrain to form origami structures. PDMS walls were created by exposing under UVO light to increase bonding

with Si NMs. Several origami structures such as Miura-ori, magic ball, star and US flag structures were achieved.

5.2 Future work

The strategy described here represents the fusion of the art of origami, kirigami, materials science, and functional energy storage devices, and could provide a paradigm shift for architecture and design of flexible and curvilinear electronics with exceptional mechanical characteristics and functionalities.

This critical feature of the present work could well benefit the general field of flexible and stretchable, electronics from a manufacturability perspective. To utilize this origami and kirigami battery concept in realistic applications with high level of deformability, at least two approaches can be considered. The first approach would be to build a functional system that includes energy harvesting devices (e.g., solar cells), energy storage devices (e.g., lithium-ion batteries) and a functional device (e.g., a display) in the same origami platform to enable equivalent deformability to each component in the system. The second approach would be to build a standalone lithium-ion battery by encapsulating the origami or kirigami battery with highly deformable elastomers to provide a flat device that could then be integrated with other functional devices leading to a fully deformable system. It is therefore expected that this technology can be applied to various deformable systems.

Because of the microscale characteristics of the origami architectures and the continuum feature of the NMs, the microscale origami may lead to multiple breakthroughs, such as in electromagnetics. Other potential applications include microscale grating, thermal invisible device, and low observable (stealth) structures.

REFERENCES

1. R. J. Lang, T. C. Hull, Origami design secrets: mathematical methods for an ancient art. *The Mathematical Intelligencer* **27**, 92-95 (2005).

2. K. Kuribayashi, K. Tsuchiya, Z. You, D. Tomus, M. Umemoto, T. Ito, M. Sasaki, Self-deployable origami stent grafts as a biomedical application of Ni-rich TiNi shape memory alloy foil. *Mater. Sci. Eng. A-Struct. Mater. Prop. Microstruct. Process.* **419**, 131-137 (2006).

3. J. L. Silverberg, J.-H. Na, A. A. Evans, B. Liu, T. C. Hull, C. D. Santangelo, R. J. Lang, R. C. Hayward, I. Cohen, Origami structures with a critical transition to bistability arising from hidden degrees of freedom. *Nature materials* **14**, 389-393 (2015).

4. T. Tachi, Rigid-foldable thick origami. *Origami* **5**, 253-264 (2011).

5. J. P. Gardner, J. C. Mather, M. Clampin, R. Doyon, M. A. Greenhouse, H. B. Hammel, J. B. Hutchings, P. Jakobsen, S. J. Lilly, K. S. Long, J. I. Lunine, M. J. McCaughrean, M. Mountain, J. Nella, G. H. Rieke, M. J. Rieke, H. W. Rix, E. P. Smith, G. Sonneborn, M. Stiavelli, H. S. Stockman, R. A. Windhorst, G. S. Wright, The James Webb Space Telescope. *Space Science Reviews* **123**, 485-606 (2006).

6. Y. Chen, R. Peng, Z. You, Origami of thick panels. *Science* **349**, 396-400 (2015).

7. K. Fuchi, P. R. Buskohl, G. Bazzan, M. F. Durstock, G. W. Reich, R. A. Vaia, J. J. Joo, Origami Actuator Design and Networking Through Crease Topology Optimization. *Journal of Mechanical Design* **137**, 091401 (2015).

8. X. Liu, S. V. Georgakopoulos, M. Tentzeris, in *Wireless and Microwave Technology Conference (WAMICON)*. (2015), pp. 1-3.

9. S. Yao, X. Liu, S. V. Georgakopoulos, M. M. Tentzeris, in *Antennas and Propagation Society International Symposium (APSURSI)*. (2014), pp. 370-371.

10. X. Liu, S. Yao, S. V. Georgakopoulos, in *Antennas and Propagation Society International Symposium (APSURSI)*. (2014), pp. 368-369.

11. X. Liu, S. Yao, S. V. Georgakopoulos, M. Tentzeris, in *Antennas and Propagation Society International Symposium (APSURSI), 2014 IEEE*. (IEEE, 2014), pp. 372-373.

12. O. Jonah, S. V. Georgakopoulos, in *Antennas and Propagation Society International Symposium (APSURSI), 2013 IEEE*. (IEEE, 2013), pp. 1040-1041.

13. Y. Liu, J. K. Boyles, J. Genzer, M. D. Dickey, Self-folding of polymer sheets using local light absorption. *Soft Matter* **8**, 1764-1769 (2012).

14. S. M. Felton, M. T. Tolley, B. Shin, C. D. Onal, E. D. Demaine, D. Rus, R. J. Wood, Self-folding with shape memory composites. *Soft Matter* **9**, 7688-7694 (2013).

15. S. Felton, M. Tolley, E. Demaine, D. Rus, R. Wood, A method for building self-folding machines. *Science* **345**, 644-646 (2014).

16. Q. Ge, H. J. Qi, M. L. Dunn, Active materials by four-dimension printing. *Applied Physics Letters* **103**, 131901 (2013).

17. Q. Ge, C. K. Dunn, H. J. Qi, M. L. Dunn, Active origami by 4D printing. *Smart Materials and Structures* **23**, 094007 (2014).

18. E. T. Filipov, T. Tachi, G. H. Paulino, Origami tubes assembled into stiff, yet reconfigurable structures and metamaterials. *Proceedings of the National Academy of Sciences* **112**, 12321-12326 (2015).

19. Z. Song, T. Ma, R. Tang, Q. Cheng, X. Wang, D. Krishnaraju, R. Panat, C. K. Chan, H. Yu, H. Jiang, Origami Lithium-ion Batteries. *Nature Communications* **5:3140 doi: 10.1038/ncomms4140**, (2014).

20. E. D. Demaine, M. L. Demaine, J. Ku, in *Proc. fifth international meeting of origami science, mathematics, and education*. (2011), pp. 449-455.

21. G. J. Hayes, J.-H. So, A. Qusba, M. D. Dickey, G. Lazzi, Flexible liquid metal alloy (EGaIn) microstrip patch antenna. *Antennas and Propagation, IEEE Transactions on* **60**, 2151-2156 (2012).

22. T. Tachi, Designing freeform origami tessellations by generalizing Resch's patterns. *Journal of mechanical design* **135**, 111006 (2013).

23. T. Tachi, in *The Fourth International Conference on Origami in Science, Mathematics, and Education, R. Lang, ed., Pasadena*. (2009), pp. 259-272.

24. S. A. Zirbel, R. J. Lang, M. W. Thomson, D. A. Sigel, P. E. Walkemeyer, B. P. Trease, S. P. Magleby, L. L. Howell, Accommodating thickness in origami-based deployable arrays. *Journal of Mechanical Design* **135**, 111005 (2013).

25. R. J. Lang, in *Proceedings of the twelfth annual symposium on Computational geometry*. (ACM, 1996), pp. 98-105.

26. L. A. Bowen, C. L. Grames, S. P. Magleby, L. L. Howell, R. J. Lang, A classification of action origami as systems of spherical mechanisms. *Journal of Mechanical Design* **135**, 111008 (2013).

27. E. A. Peraza-Hernandez, D. J. Hartl, R. J. Malak Jr, D. C. Lagoudas, Origami-inspired active structures: a synthesis and review. *Smart Materials and Structures* **23**, 094001 (2014).

28. Y. Chen, J. Au, P. Kazlas, A. Ritenour, H. Gates, M. McCreary, Electronic paper: Flexible active-matrix electronic ink display. *Nature* **423**, 136-136 (2003).

29. G. H. Gelinck, H. E. A. Huitema, E. Van Veenendaal, E. Cantatore, L. Schrijnemakers, J. Van der Putten, T. C. T. Geuns, M. Beenhakkers, J. B. Giesbers, B. H. Huisman, E. J. Meijer, E. M. Benito, F. J. Touwslager, A. W. Marsman, B. J. E. Van Rens, D. M. De Leeuw, Flexible active-matrix displays and shift registers based on solution-processed organic transistors. *Nature Materials* **3**, 106-110 (2004).

30. S. Kim, H. J. Kwon, S. Lee, H. Shim, Y. Chun, W. Choi, J. Kwack, D. Han, M. Song, S. Kim, S. Mohammadi, I. Kee, S. Y. Lee, Low-Power Flexible Organic Light-Emitting Diode Display Device. *Advanced Materials* **23**, 3511-+ (2011).

31. B. Yoon, D. Y. Ham, O. Yarimaga, H. An, C. W. Lee, J. M. Kim, Inkjet Printing of Conjugated Polymer Precursors on Paper Substrates for Colorimetric Sensing and Flexible Electrothermochromic Display. *Advanced Materials* **23**, 5492-+ (2011).

32. D. H. Kim, J. H. Ahn, W. M. Choi, H. S. Kim, T. H. Kim, J. Z. Song, Y. G. Y. Huang, Z. J. Liu, C. Lu, J. A. Rogers, Stretchable and foldable silicon integrated circuits. *Science* **320**, 507-511 (2008).

33. H. C. Ko, M. P. Stoykovich, J. Z. Song, V. Malyarchuk, W. M. Choi, C. J. Yu, J. B. Geddes, J. L. Xiao, S. D. Wang, Y. G. Huang, J. A. Rogers, A hemispherical electronic eye camera based on compressible silicon optoelectronics. *Nature* **454**, 748-753 (2008).

34. D. H. Kim, N. S. Lu, R. Ma, Y. S. Kim, R. H. Kim, S. D. Wang, J. Wu, S. M. Won, H. Tao, A. Islam, K. J. Yu, T. I. Kim, R. Chowdhury, M. Ying, L. Z. Xu, M. Li, H. J. Chung, H. Keum, M. McCormick, P. Liu, Y. W. Zhang, F. G. Omenetto, Y. G. Huang, T. Coleman, J. A. Rogers, Epidermal Electronics. *Science* **333**, 838-843 (2011).

35. V. L. Pushparaj, M. M. Shaijumon, A. Kumar, S. Murugesan, L. Ci, R. Vajtai, R. J. Linhardt, O. Nalamasu, P. M. Ajayan, Flexible energy storage devices based on nanocomposite paper. *Proceedings of the National Academy of Sciences of the United States of America* **104**, 13574-13577 (2007).

36. B. Scrosati, Nanomaterials - Paper powers battery breakthrough. *Nature Nanotechnology* **2**, 598-599 (2007).

37. L. B. Hu, J. W. Choi, Y. Yang, S. Jeong, F. La Mantia, L. F. Cui, Y. Cui, Highly conductive paper for energy-storage devices. *Proceedings of the National Academy of Sciences of the United States of America* **106**, 21490-21494 (2009).

38. K. Z. Gao, Z. Q. Shao, X. Wu, X. Wang, Y. H. Zhang, W. J. Wang, F. J. Wang, Paper-based transparent flexible thin film supercapacitors. *Nanoscale* **5**, 5307-5311 (2013).

39. J. Z. Wang, S. L. Chou, H. Liu, G. X. Wang, C. Zhong, S. Y. Chew, H. K. Liu, Highly flexible and bendable free-standing thin film polymer for battery application. *Materials Letters* **63**, 2352-2354 (2009).

40. L. B. Hu, H. Wu, F. La Mantia, Y. A. Yang, Y. Cui, Thin, Flexible Secondary Li-Ion Paper Batteries. *Acs Nano* **4**, 5843-5848 (2010).

41. J. F. Ihlefeld, P. G. Clem, B. L. Doyle, P. G. Kotula, K. R. Fenton, C. A. Apblett, Fast Lithium-Ion Conducting Thin-Film Electrolytes Integrated Directly on Flexible Substrates for High-Power Solid-State Batteries. *Advanced Materials* **23**, 5663-+ (2011).

42. M. Koo, K. I. Park, S. H. Lee, M. Suh, D. Y. Jeon, J. W. Choi, K. Kang, K. J. Lee, Bendable Inorganic Thin-Film Battery for Fully Flexible Electronic Systems. *Nano Letters* **12**, 4810-4816 (2012).

43. A. M. Gaikwad, D. A. Steingart, T. N. Ng, D. E. Schwartz, G. L. Whiting, A flexible high potential printed battery for powering printed electronics. *Applied Physics Letters* **102**, (2013).

44. Y. H. Kwon, S. W. Woo, H. R. Jung, H. K. Yu, K. Kim, B. H. Oh, S. Ahn, S. Y. Lee, S. W. Song, J. Cho, H. C. Shin, J. Y. Kim, Cable-Type Flexible Lithium Ion Battery Based on Hollow Multi-Helix Electrodes. *Advanced Materials* **24**, 5192-5197 (2012).

45. C. J. Yu, C. Masarapu, J. P. Rong, B. Q. Wei, H. Q. Jiang, Stretchable Supercapacitors Based on Buckled Single-Walled Carbon Nanotube Macrofilms. *Advanced Materials* **21**, 4793-+ (2009).

46. X. Li, T. L. Gu, B. Q. Wei, Dynamic and Galvanic Stability of Stretchable Supercapacitors. *Nano Letters* **12**, 6366-6371 (2012).

47. L. B. Hu, M. Pasta, F. La Mantia, L. F. Cui, S. Jeong, H. D. Deshazer, J. W. Choi, S. M. Han, Y. Cui, Stretchable, Porous, and Conductive Energy Textiles. *Nano Letters* **10**, 708-714 (2010).

48. S. Xu, Y. H. Zhang, J. Cho, J. Lee, X. Huang, L. Jia, J. A. Fan, Y. W. Su, J. Su, H. G. Zhang, H. Y. Cheng, B. W. Lu, C. J. Yu, C. Chuang, T. I. Kim, T. Song, K. Shigeta, S. Kang, C. Dagdeviren, I. Petrov, P. V. Braun, Y. G. Huang, U. Paik, J. A. Rogers, Stretchable batteries with self-similar serpentine interconnects and integrated wireless recharging systems. *Nature Communications* **4**, 8 (2013).

49. K. Miura, Method of packaging and deployment of large membranes in space, (Institute of Space and Astronomical Sciences, 1985).

50. Q. Cheng, Z. Song, T. Ma, B. B. Smith, R. Tang, H. Yu, H. Jiang, C. K. Chan, Folding Paper-based Lithium-ion Batteries for Higher Areal Energy Densities. *Nano Lett.* **13**, 4969-4974 (2013).

51. S.-M. Belcastro, T. C. Hull, Modeling the folding of paper into three dimensions using affine transformations. *Linear Algebra and its Applications* **348**, 273-282 (2002).

52. S.-M. Belcastro, T. C. Hull, in *Origami 3*, T. C. Hull, Ed. (A K Peters/CRC Press, 2002), pp. 39-51.

53. Y. Chen, J. Au, P. Kazlas, A. Ritenour, H. Gates, M. McCreary, Flexible active-matrix electronic ink display. *Nature* **423**, 136-136 (2003).

54. Z. Song, T. Ma, R. Tang, Q. Cheng, X. Wang, D. Krishnaraju, R. Panat, C. K. Chan, H. Yu, H. Jiang, Origami lithium-ion batteries. *Nature communications* **5**, (2014).

55. R. Tang, H. Huang, H. Tu, H. Liang, M. Liang, Z. Song, Y. Xu, H. Jiang, H. Yu, Origami-enabled Deformable Silicon Solar Cells. *Applied Physics Letters* **104**, 083501 (2014).

56. A. Khademhosseini, R. Langer, J. Borenstein, J. P. Vacanti, Microscale technologies for tissue engineering and biology. *Proceedings of the National Academy of Sciences of the United States of America* **103**, 2480-2487 (2006).

57. L. G. Griffith, M. A. Swartz, Capturing complex 3D tissue physiology in vitro. *Nature reviews Molecular cell biology* **7**, 211-224 (2006).

58. N. Bowden, S. Brittain, A. G. Evans, J. W. Hutchinson, G. M. Whitesides, Spontaneous formation of ordered structures in thin films of metals supported on an elastomeric polymer. *Nature* **393**, 146-149 (1998).

59. H. Zhang, X. Yu, P. V. Braun, Three-dimensional bicontinuous ultrafast-charge and-discharge bulk battery electrodes. *Nature nanotechnology* **6**, 277-281 (2011).

60. J. G. Fernandez, A. Khademhosseini, Micro‐masonry: construction of 3D structures by microscale self‐assembly. *Advanced Materials* **22**, 2538-2541 (2010).

61. O. G. Schmidt, K. Eberl, Nanotechnology: Thin solid films roll up into nanotubes. *Nature* **410**, 168-168 (2001).

62. S. Xu, Z. Yan, K.-I. Jang, W. Huang, H. Fu, J. Kim, Z. Wei, M. Flavin, J. McCracken, R. Wang, A. Badea, Y. Liu, D. Xiao, G. Zhou, J. Lee, H. U. Chung, H. Cheng, W. Ren, A. Banks, X. Li, U. Paik, R. G. Nuzzo, Y. Huang, Y. Zhang, J. A. Rogers, Assembly of micro/nanomaterials into complex, three-dimensional architectures by compressive buckling. *Science* **347**, 154-159 (2015).

63. E. Menard, K. Lee, D.-Y. Khang, R. Nuzzo, J. Rogers, A printable form of silicon for high performance thin film transistors on plastic substrates. *Applied Physics Letters* **84**, 5398-5400 (2004).

64. M. A. Meitl, Z.-T. Zhu, V. Kumar, K. J. Lee, X. Feng, Y. Y. Huang, I. Adesida, R. G. Nuzzo, J. A. Rogers, Transfer printing by kinetic control of adhesion to an elastomeric stamp. *Nature materials* **5**, 33-38 (2006).

65. R. H. Baughman, A. A. Zakhidov, W. A. de Heer, Carbon nanotubes--the route toward applications. *science* **297**, 787-792 (2002).

66. Q. Cao, J. A. Rogers, Ultrathin films of single‐walled carbon nanotubes for electronics and sensors: a review of fundamental and applied aspects. *Advanced Materials* **21**, 29-53 (2009).

67. T. Dürkop, S. Getty, E. Cobas, M. Fuhrer, Extraordinary mobility in semiconducting carbon nanotubes. *Nano letters* **4**, 35-39 (2004).

68. J. Kong, N. R. Franklin, C. Zhou, M. G. Chapline, S. Peng, K. Cho, H. Dai, Nanotube molecular wires as chemical sensors. *Science* **287**, 622-625 (2000).

69. J. Yeom, M. A. Shannon, Detachment Lithography of Photosensitive Polymers: A Route to Fabricating Three‐Dimensional Structures. *Advanced Functional Materials* **20**, 289-295 (2010).

70. Y. Xia, G. M. Whitesides, Soft lithography. *Annual review of materials science* **28**, 153-184 (1998).

71. J. A. Rogers, R. G. Nuzzo, Recent progress in soft lithography. *Materials today* **8**, 50-56 (2005).

72. E. Menard, M. A. Meitl, Y. Sun, J.-U. Park, D. J.-L. Shir, Y.-S. Nam, S. Jeon, J. A. Rogers, Micro-and nanopatterning techniques for organic electronic and optoelectronic systems. *Chemical reviews* **107**, 1117-1160 (2007).

73. P. Björk, S. Holmström, O. Inganäs, Soft Lithographic Printing of Patterns of Stretched DNA and DNA/Electronic Polymer Wires by Surface - Energy Modification and Transfer. *Small* **2**, 1068-1074 (2006).

74. H. Nakao, M. Gad, S. Sugiyama, K. Otobe, T. Ohtani, Transfer-printing of highly aligned DNA nanowires. *Journal of the American Chemical Society* **125**, 7162-7163 (2003).

75. A. Amy áYu, Stamping with high information density. *Journal of Materials Chemistry* **16**, 2868-2870 (2006).

76. G. Malliaras, R. Friend, An organic electronics primer. *Physics Today* **58**, 53-58 (2005).

77. T. W. Kelley, P. F. Baude, C. Gerlach, D. E. Ender, D. Muyres, M. A. Haase, D. E. Vogel, S. D. Theiss, Recent progress in organic electronics: Materials, devices, and processes. *Chemistry of Materials* **16**, 4413-4422 (2004).

78. J. M. Frechet, Functional polymers and dendrimers: reactivity, molecular architecture, and interfacial energy. *Science-AAAS-Weekly Paper Edition-including Guide to Scientific Information* **263**, 1710-1714 (1994).

79. Y.-L. Loo, R. L. Willett, K. W. Baldwin, J. A. Rogers, Interfacial chemistries for nanoscale transfer printing. *Journal of the American Chemical Society* **124**, 7654-7655 (2002).

80. E. J. Smythe, M. D. Dickey, G. M. Whitesides, F. Capasso, A technique to transfer metallic nanoscale patterns to small and non-planar surfaces. *ACS nano* **3**, 59-65 (2008).

81. K. Felmet, Y.-L. Loo, Y. Sun, Patterning conductive copper by nanotransfer printing. *Applied physics letters* **85**, 3316-3318 (2004).

82. H. Schmid, H. Wolf, R. Allenspach, H. Riel, S. Karg, B. Michel, E. Delamarche, Preparation of metallic films on elastomeric stamps and their application for contact processing and contact printing. *Advanced Functional Materials* **13**, 145-153 (2003).

83. T. H. Kim, W. M. Choi, D. H. Kim, M. A. Meitl, E. Menard, H. Jiang, J. A. Carlisle, J. A. Rogers, Printable, flexible, and stretchable forms of ultrananocrystalline diamond with applications in thermal management. *Advanced Materials* **20**, 2171-2176 (2008).

84. A. Kawahara, H. Katsuki, M. Egashira, Fabrication of semiconductor oxide thick films by slide-off transfer printing and their NO 2-sensing properties. *Sensors and Actuators B: Chemical* **49**, 273-278 (1998).

85. K. J. Lee, J. Lee, H. Hwang, Z. J. Reitmeier, R. F. Davis, J. A. Rogers, R. G. Nuzzo, A Printable Form of Single‐Crystalline Gallium Nitride for Flexible Optoelectronic Systems. *small* **1**, 1164-1168 (2005).

86. Y. Sun, J. A. Rogers, Inorganic semiconductors for flexible electronics. *Advanced Materials* **19**, 1897-1916 (2007).

87. Y. Sun, H. S. Kim, E. Menard, S. Kim, I. Adesida, J. A. Rogers, Printed arrays of aligned GaAs wires for flexible transistors, diodes, and circuits on plastic substrates. *small* **2**, 1330-1334 (2006).

88. A. J. Baca, J. H. Ahn, Y. Sun, M. A. Meitl, E. Menard, H. S. Kim, W. M. Choi, D. H. Kim, Y. Huang, J. A. Rogers, Semiconductor Wires and Ribbons for High‐Performance Flexible Electronics. *Angewandte Chemie International Edition* **47**, 5524-5542 (2008).

89. D. H. Kim, Y. S. Kim, J. Wu, Z. Liu, J. Song, H. S. Kim, Y. Y. Huang, K. C. Hwang, J. A. Rogers, Ultrathin silicon circuits with strain‐isolation layers and mesh layouts for high‐performance electronics on fabric, vinyl, leather, and paper. *Advanced Materials* **21**, 3703-3707 (2009).

90. D.-H. Kim, J.-H. Ahn, H.-S. Kim, K. J. Lee, T.-H. Kim, C.-J. Yu, R. G. Nuzzo, J. A. Rogers, Complementary logic gates and ring oscillators on plastic substrates by use of printed ribbons of single-crystalline silicon. *Electron Device Letters, IEEE* **29**, 73-76 (2008).

91. J.-H. Ahn, H.-S. Kim, K. J. Lee, S. Jeon, S. J. Kang, Y. Sun, R. G. Nuzzo, J. A. Rogers, Heterogeneous three-dimensional electronics by use of printed semiconductor nanomaterials. *science* **314**, 1754-1757 (2006).

92. J. Yoon, A. J. Baca, S.-I. Park, P. Elvikis, J. B. Geddes, L. Li, R. H. Kim, J. Xiao, S. Wang, T.-H. Kim, Ultrathin silicon solar microcells for semitransparent, mechanically flexible and microconcentrator module designs. *Nature materials* **7**, 907-915 (2008).

93. A. J. Baca, K. J. Yu, J. Xiao, S. Wang, J. Yoon, J. H. Ryu, D. Stevenson, R. G. Nuzzo, A. A. Rockett, Y. Huang, Compact monocrystalline silicon solar modules with high voltage outputs and mechanically flexible designs. *Energy & Environmental Science* **3**, 208-211 (2010).

94. S. Mack, M. A. Meitl, A. J. Baca, Z.-T. Zhu, J. A. Rogers, Mechanically flexible thin-film transistors that use ultrathin ribbons of silicon derived from bulk wafers. *Applied physics letters* **88**, 213101 (2006).

95. E. Menard, R. G. Nuzzo, J. A. Rogers, Bendable single crystal silicon thin film transistors formed by printing on plastic substrates. *Applied Physics Letters* **86**, 093507 (2005).

96. I. Jung, G. Shin, V. Malyarchuk, J. S. Ha, J. A. Rogers, Paraboloid electronic eye cameras using deformable arrays of photodetectors in hexagonal mesh layouts. *Applied Physics Letters* **96**, 021110 (2010).

97. S.-I. Park, Y. Xiong, R.-H. Kim, P. Elvikis, M. Meitl, D.-H. Kim, J. Wu, J. Yoon, C.-J. Yu, Z. Liu, Printed assemblies of inorganic light-emitting diodes for deformable and semitransparent displays. *science* **325**, 977-981 (2009).

98. J.-h. Choi, K.-H. Kim, S.-J. Choi, H. H. Lee, Whole device printing for full colour displays with organic light emitting diodes. *Nanotechnology* **17**, 2246 (2006).

99. Y.-L. Loo, R. L. Willett, K. W. Baldwin, J. A. Rogers, Additive, nanoscale patterning of metal films with a stamp and a surface chemistry mediated transfer process: Applications in plastic electronics. *Applied Physics Letters* **81**, 562-564 (2002).

100. D. Suh, S. J. Choi, H. H. Lee, Rigiflex lithography for nanostructure transfer. *Advanced materials* **17**, 1554-1560 (2005).

101. D. Hines, S. Mezhenny, M. Breban, E. Williams, V. Ballarotto, G. Esen, A. Southard, M. Fuhrer, Nanotransfer printing of organic and carbon nanotube thin-film transistors on plastic substrates. *Applied Physics Letters* **86**, 163101 (2005).

102. J. Zaumseil, M. A. Meitl, J. W. Hsu, B. R. Acharya, K. W. Baldwin, Y.-L. Loo, J. A. Rogers, Three-dimensional and multilayer nanostructures formed by nanotransfer printing. *Nano Letters* **3**, 1223-1227 (2003).

103. S.-H. Hur, D.-Y. Khang, C. Kocabas, J. A. Rogers, Nanotransfer printing by use of noncovalent surface forces: applications to thin-film transistors that use single-walled carbon nanotube networks and semiconducting polymers. *Applied Physics Letters* **85**, 5730-5732 (2004).

104. H. Ahn, K. J. Lee, W. R. Childs, J. A. Rogers, R. G. Nuzzo, A. Shim, Micron and submicron patterning of polydimethylsiloxane resists on electronic materials by decal transfer lithography and reactive ion-beam etching: application to the fabrication of high-mobility, thin-film transistors. *Journal of applied physics* **100**, 084907 (2006).

105. W. R. Childs, M. J. Motala, K. J. Lee, R. G. Nuzzo, Masterless soft lithography: patterning UV/Ozone-induced adhesion on poly (dimethylsiloxane) surfaces. *Langmuir* **21**, 10096-10105 (2005).

106. W. R. Childs, R. G. Nuzzo, Decal transfer microlithography: a new soft-lithographic patterning method. *Journal of the American Chemical Society* **124**, 13583-13596 (2002).

107. W. Childs, R. G. Nuzzo, Patterning of Thin‐Film Microstructures on Non‐Planar Substrate Surfaces Using Decal Transfer Lithography. *Advanced Materials* **16**, 1323-1327 (2004).

108. W. R. Childs, R. G. Nuzzo, Large-area patterning of coinage-metal thin films using decal transfer lithography. *Langmuir* **21**, 195-202 (2005).

109. Y. Berdichevsky, J. Khandurina, A. Guttman, Y.-H. Lo, UV/ozone modification of poly (dimethylsiloxane) microfluidic channels. *Sensors and Actuators B: Chemical* **97**, 402-408 (2004).

110. R. Muisener, C. Mirley, J. Koberstein, in *APS March Meeting Abstracts*. (1996), vol. 1, pp. 3229.

111. D. C. Duffy, J. C. McDonald, O. J. A. Schueller, G. M. Whitesides, Rapid prototyping of microfluidic systems in poly(dimethylsiloxane). *Analytical Chemistry* **70**, 4974-4984 (1998).

112. D. Y. Khang, H. Q. Jiang, Y. Huang, J. A. Rogers, A stretchable form of single-crystal silicon for high-performance electronics on rubber substrates. *Science* **311**, 208-212 (2006).

113. Y. G. Sun, W. M. Choi, H. Q. Jiang, Y. G. Y. Huang, J. A. Rogers, Controlled buckling of semiconductor nanoribbons for stretchable electronics. *Nature Nanotechnology* **1**, 201-207 (2006).

APPENDIX A

PATTERNS OF PDMS WALLS DESIGNED BY AUTOCAD

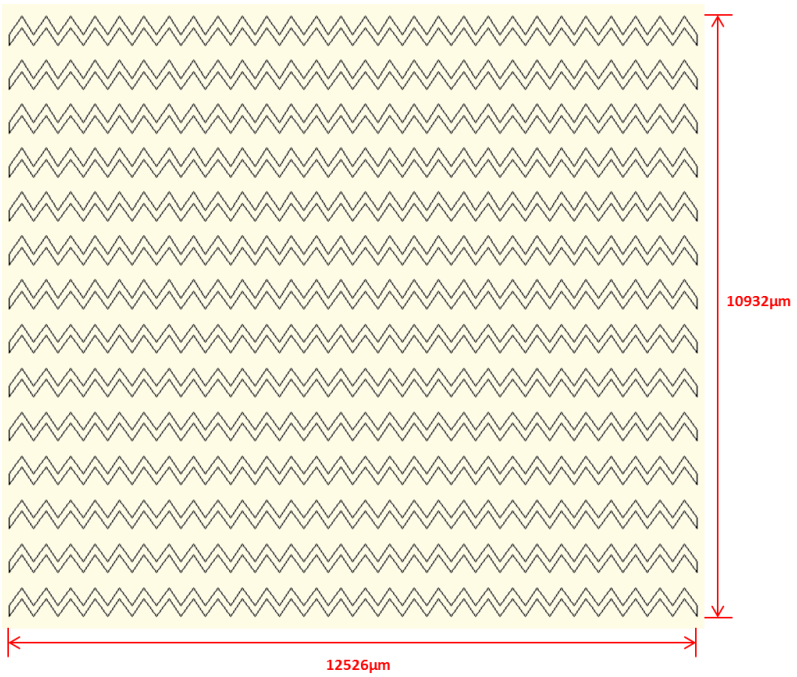

(a)

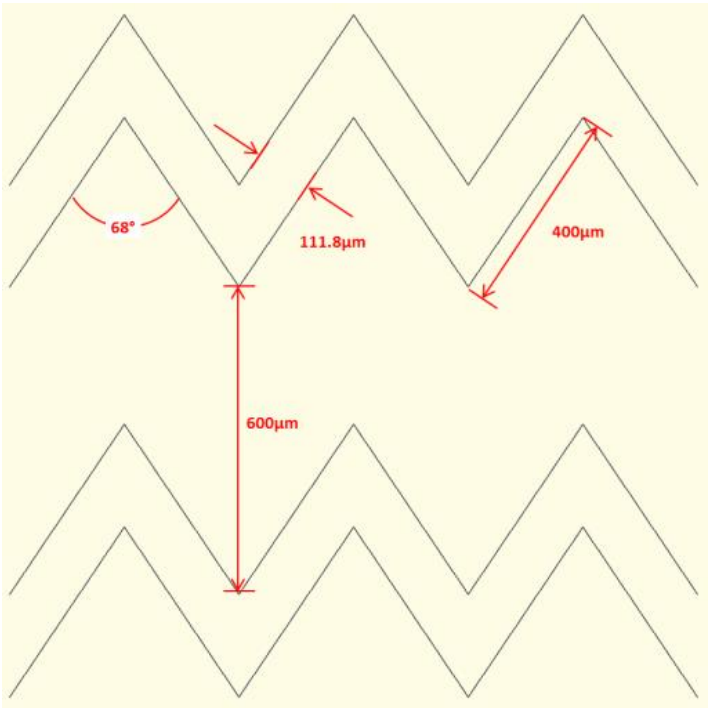

(b)

Figure A1. Geometry of the pre-patterned PDMS wall with Miura-ori pattern. (a) Overall dimension. (b) Detailed dimension.

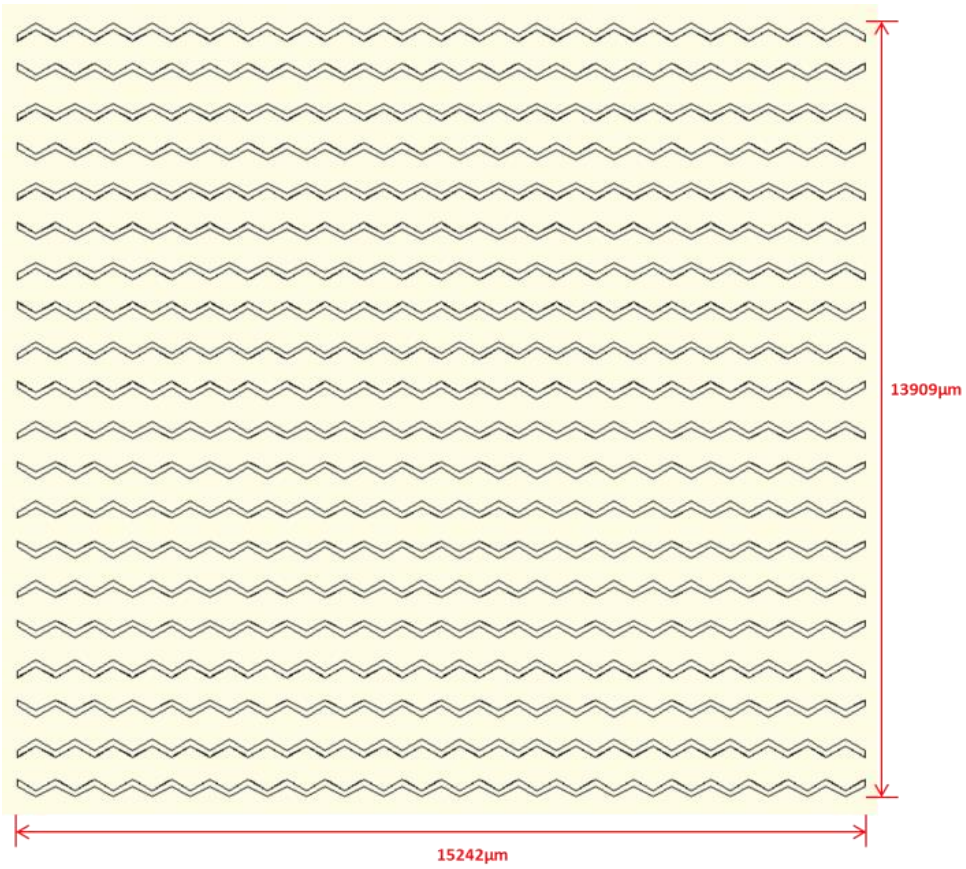

(a)

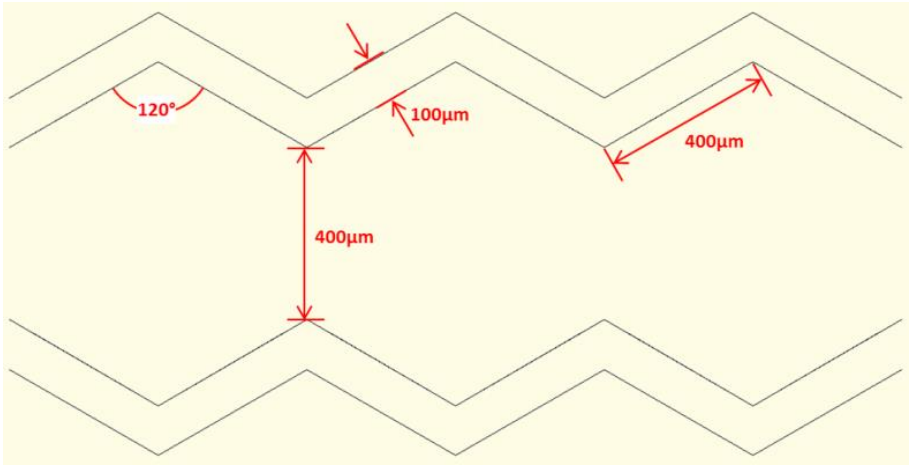

(b)

Figure A2. Geometry of the pre-patterned PDMS wall with magic ball pattern. (a) Overall dimension. (b) Detailed dimension.

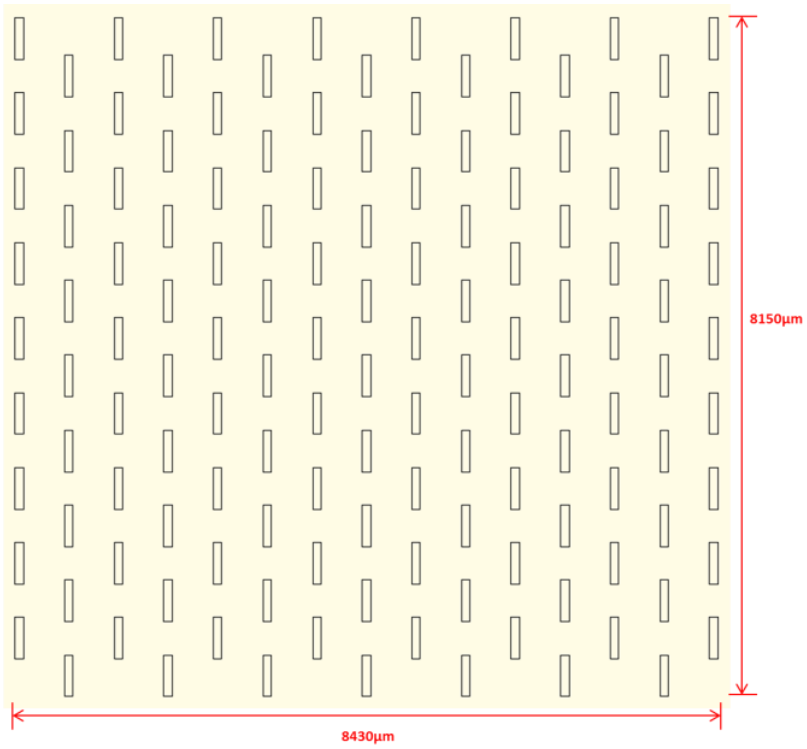

(a)

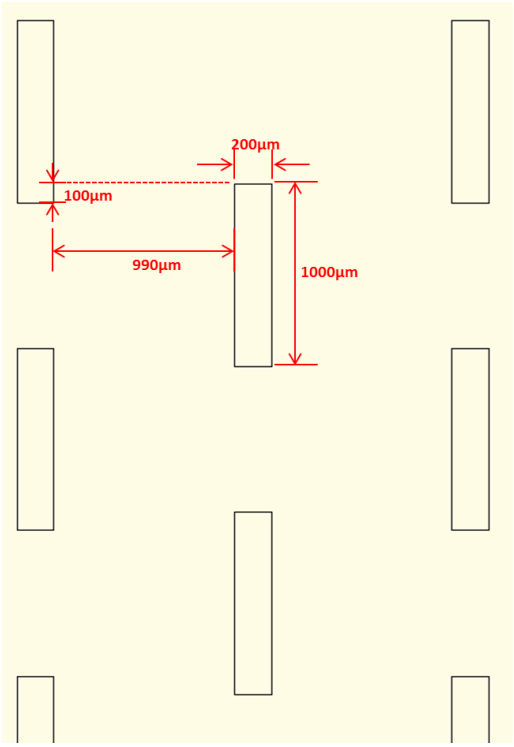

(b)

Figure A3. Geometry of the pre-patterned PDMS wall with non-rigidly foldable pattern. (a) Overall dimension. (b) Detailed dimension.

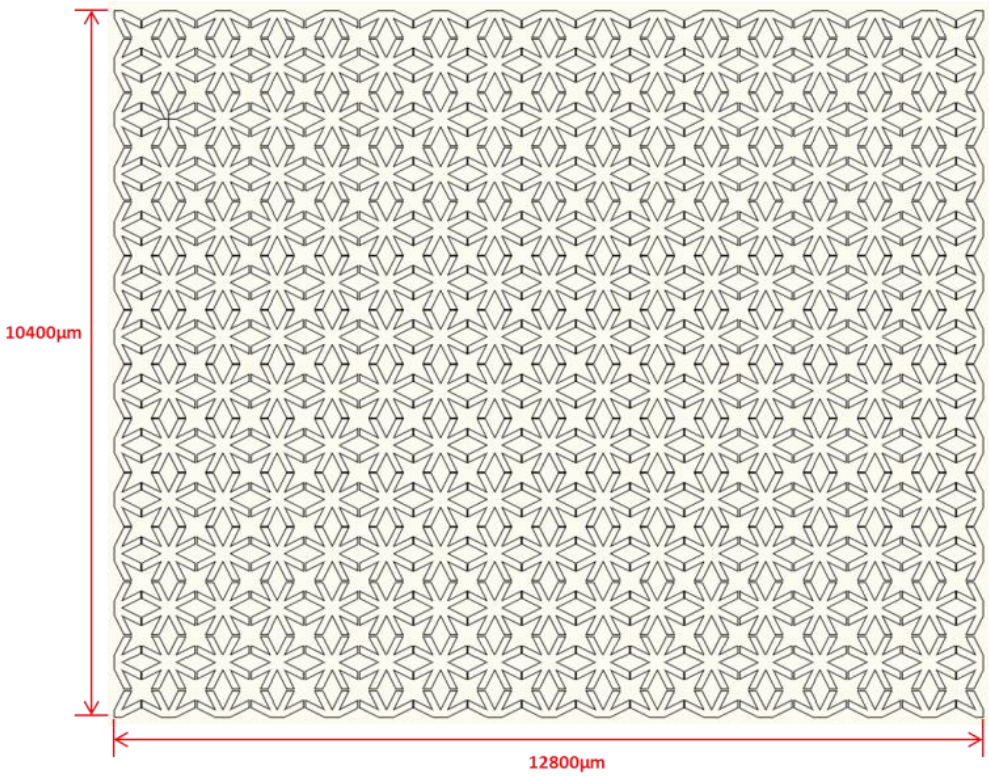

(a)

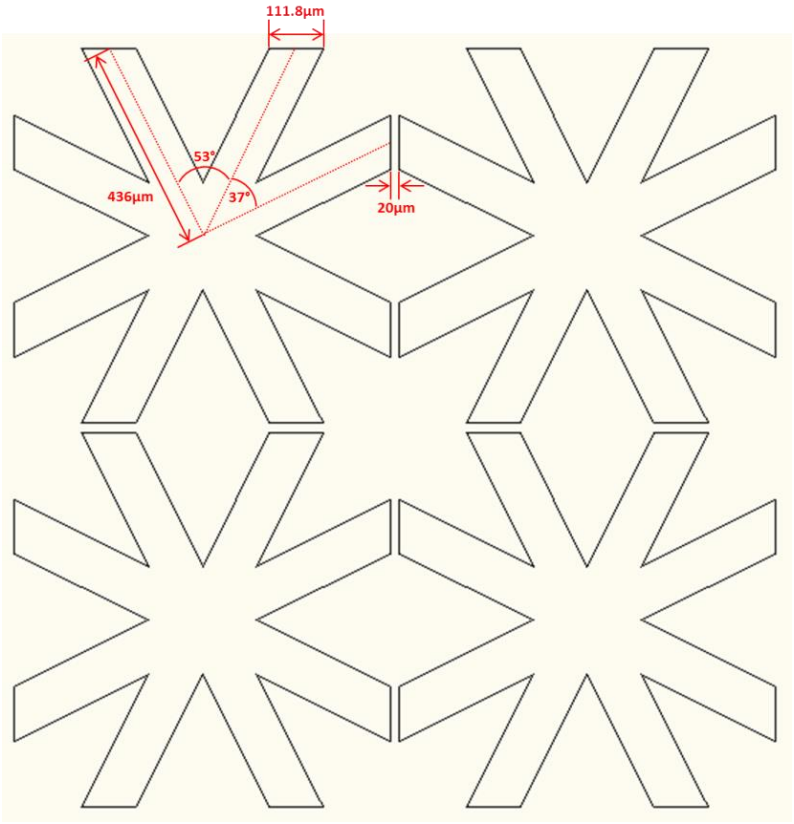

(b)

Figure A4. Geometry of the pre-patterned PDMS wall with star pattern. (a) Overall dimension. (b) Detailed dimension.

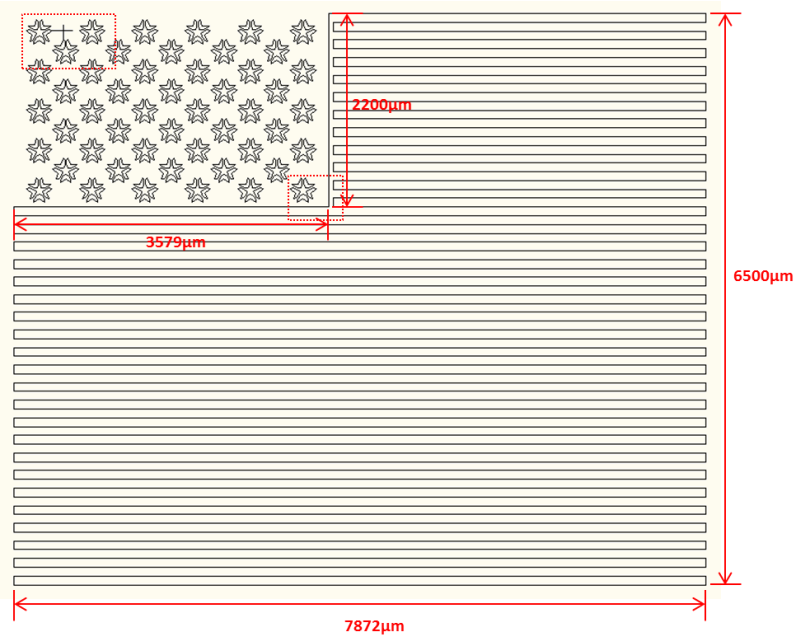

(a)

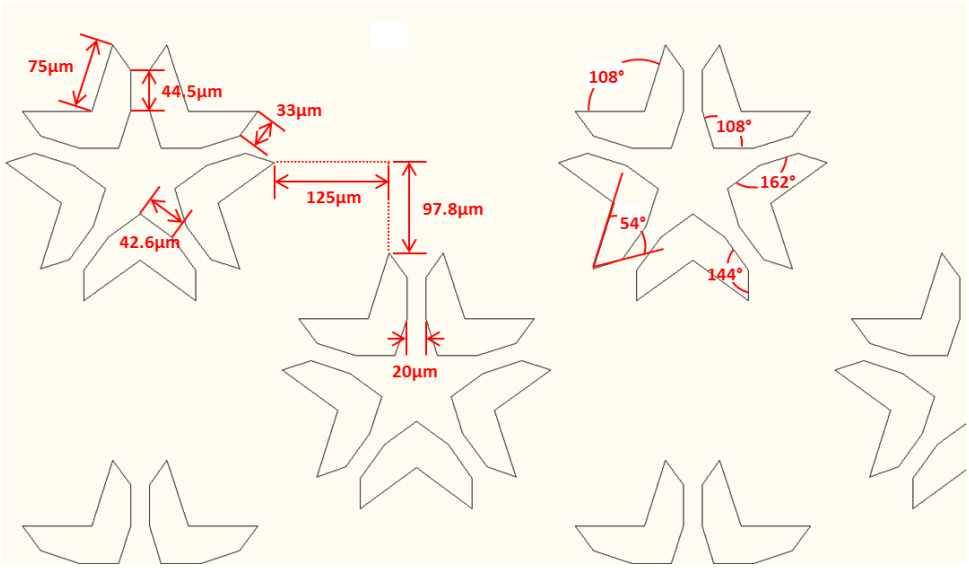

(b)

Figure A5. Geometry of the pre-patterned PDMS wall with US flag pattern. (a) Overall dimension. (b) Detailed dimension.